Feasibility Study for Detection and Quantification of Corrosion in Bridge Barrier Rails

Final Report
April 2013

IPRT **works**
for Iowa

IOWA STATE UNIVERSITY
Center for Nondestructive Evaluation

IOWA STATE UNIVERSITY
Institute for Transportation

About the Center for Nondestructive Evaluation

The Center for Nondestructive Evaluation (CNDE) is a National Science Foundation Industry/University Cooperative Research Center and is a member of the Institute for Physical Research and Technology at Iowa State University. The Center focuses on the research and development of new theories and techniques for use in quantitative nondestructive evaluation.

Disclaimer Notice

Non-Discrimination Statement

Iowa Department of Transportation Statements

Technical Report Documentation Page

1. Report No. InTrans Project 11-413	2. Government Accession No.	3. Recipient's Catalog No.	
4. Title and Subtitle Feasibility Study for Detection and Quantification of Corrosion in Bridge Barrier Rails		**5. Report Date** April 2013	
		6. Performing Organization Code	
7. Author(s) T. Jensen, S. Wendt, J. Gray, D. Eisenmann, F. Margetan, C. Lo, N. Nakagawa, and L. Brasche		**8. Performing Organization Report No.** InTrans Project 11-413	
9. Performing Organization Name and Address Center for Nondestructive Evaluation Iowa State University 1915 Scholl Road Ames, IA 50010		**10. Work Unit No. (TRAIS)**	
		11. Contract or Grant No.	
12. Sponsoring Organization Name and Address Iowa Department of Transportation 800 Lincoln Way Ames, IA 50010	Federal Highway Administration U.S. Department of Transportation 400 7th Street SW Washington, DC 20590	**13. Type of Report and Period Covered** Final Report	
		14. Sponsoring Agency Code SPR 90-00-RB22-012	

15. Supplementary Notes

Visit www.intrans.iastate.edu for color pdfs of this and other research reports.

16. Abstract

Technical challenges exist with infrastructure that can be addressed by nondestructive evaluation (NDE) methods, such as detecting corrosion damage to reinforcing steel that anchor concrete bridge railings to bridge road decks. Moisture and chloride ions reach the anchors along the cold joint between the rails and deck, causing corrosion that weakens the anchors and ultimately the barriers.

The Center for Nondestructive Evaluation at Iowa State University has experience in development of measurement techniques and new sensors using a variety of interrogating energies. This research evaluated feasibility of three technologies—x-ray radiation, ground-penetrating radar (GPR), and magnetic flux leakage (MFL)—for detection and quantification of corrosion of embedded reinforcing steel.

Controlled samples containing pristine reinforcing steel with and without epoxy and reinforcing steel with 25 percent and 50 percent section reduction were embedded in concrete at 2.5 in. deep for laboratory evaluation. Two of the techniques, GPR and MFL, were used in a limited field test on the Iowa Highway 210 Bridge over Interstate 35 in Story County.

The methods provide useful and complementary information. GPR provides a rapid approach to identify reinforcing steel that has anomalous responses. MFL provides similar detection responses but could be optimized to provide more quantitative correlation to actual condition. Full implementation could use either GPR or MFL methods to identify areas of concern, followed by radiography to give a visual image of the actual condition, providing the final guidance for maintenance actions.

17. Key Words concrete bridge barriers—corrosion quantification—giant magnetoresistance sensors—ground-penetrating radar—magnetic flux leakage—nondestructive testing—radiography—reinforcing steel evaluation—steel corrosion		18. Distribution Statement No restrictions.	
19. Security Classification (of this report) Unclassified.	**20. Security Classification (of this page)** Unclassified.	**21. No. of Pages** 101	**22. Price** NA

Form DOT F 1700.7 (8-72)   **Reproduction of completed page authorized**

FEASIBILITY STUDY FOR DETECTION AND QUANTIFICATION OF CORROSION IN BRIDGE BARRIER RAILS

Authors
Terry Jensen, Scott Wendt, Joe Gray, Chester Lo, Frank Margetan,
David Eisenmann, Norio Nakagawa, and Lisa Brasche

TABLE OF CONTENTS

LIST OF FIGURES

LIST OF TABLES

ACKNOWLEDGMENTS

EXECUTIVE SUMMARY

The US transportation system is at the heart of our economic prosperity, providing the network for the movement of people and products. We rely on our roadways and bridges for safe passage in a time-efficient manner. Availability for traffic places strict demands on inspection methods in regards to speed and reliability ensuring that the time to complete an inspection is minimized and that results provide sufficient, quantitative information to enable repair/replace decisions.

There are multiple technical challenges involved with the nation's aging infrastructure that can be addressed by nondestructive evaluation methods. One such challenge involves detecting corrosion damage to the reinforcing steel and U-bolts that anchor concrete bridge barrier rails to the road deck of some bridge structures. Moisture and chloride ions reach the reinforcing steel or U-bolt anchors along the cold joint between the rails and the deck and cause general corrosion that can weaken the performance of the anchors and ultimately the barriers.

The Center for Nondestructive Evaluation (CNDE) at Iowa State University (ISU) has extensive experience in the development of measurement techniques and new sensor applications using a variety of interrogating energies. CNDE joined forces with the Bridge Engineering Center at ISU to build on their experience with bridge design and use.

This research project evaluated the feasibility of three technologies, x-ray radiation, ground-penetrating radar (GPR), and a magnetic flux leakage (MFL) approach using a giant magnetoresistance (GMR) sensor, for the detection and quantification of corrosion of embedded reinforcing steel. A set of controlled samples containing pristine reinforcing steel with and without epoxy, and reinforcing steel with 25 percent and 50 percent section reduction, were embedded in concrete at 2.5 in. depths.

The controlled samples were used to develop each of the three methods. Two of the techniques, GPR and MFL, were also used in a limited field test on the Iowa Highway 210 Bridge over Interstate 35 (I-35) in Story County, Iowa. Primary conclusions for each of the three methods are as follows.

- Radiographic inspection provides a visual image of the position and condition of the reinforcing steel. Proper selection of the source is needed to ensure penetration of the x-ray energy through typical thicknesses of concrete. Several detector options are also available including film and digital detectors. Hesitancy has existed with use of radiography because of cost and health safety concerns (i.e., protection zones are needed to prevent inadvertent radiation exposure to humans). However, modern digital x-ray detectors reduce the exposure time and use less radiation, thus increasing the cost-to-benefit ratio for this method. Further improvements could result from the use of backscatter x-ray methods, which is a topic recommended for future study. The benefits of actual visual evidence of the reinforcing steel condition could lead to more-effective decisions regarding bridge maintenance actions and ensure that scarce infrastructure resources are used where they are needed most.

- An MFL sensor was designed and fabricated using GMR sensors. Laboratory tests showed a monotonic decrease in signal response with material loss, which indicates the ability to quantify corrosion damage in standalone reinforcing steel. Interference can occur when other reinforcing bars are in close proximity, so application of this technique requires independent knowledge of the location of the bars. Future sensor designs could combine an eddy current sensor with the MFL measurement to address this issue. The sensor was also used to inspect 18 reinforcing bar locations on the Highway 210 Bridge over I-35. Of the 18 locations, 13 showed a stronger off-deck response than measurements near the cold joint, indicating suspect conditions.

- GPR was also applied to quantitative detection of corrosion damage. Use of GPR for locating reinforcing steel in concrete is well-documented. In this project, techniques were developed to detect corrosion damage using laboratory samples and then applied to inspection of 88 reinforcing bars on the Highway 210 Bridge, moving beyond location of reinforcing bars to condition assessment. The method compares the response in a known undamaged region to the response near the cold joint. Of the 88 reinforcing bars, 11 were found to be anomalous. Agreement was found between the GPR and MFL results for those locations that were inspected using both methods.

Each of the methods considered in this research provide useful and complementary information. GPR methods provide a rapid approach to identify reinforcing steel that has anomalous responses. The MFL technique provides similar detection responses but could be optimized to provide more quantitative correlation to the actual reinforcing steel condition. The GPR or MFL methods could be used to identify areas of concern. Radiography could then be used to give a visual image of the actual condition at those points, providing the final guidance needed to plan bridge maintenance actions. Use of modern, digital x-ray detectors would further improve the speed and cost of x-ray inspection, making this a more attractive option than in prior film-based radiography studies.

1   BACKGROUND

1.1   Review and Introduction

America's bridges play a crucial role in economics and public safety and yet are suffering along with much of our infrastructure from a lack of investment to sustain this critical resource. The American Society of Civil Engineers (ASCE) gave a C grade to our nation's bridges in their 2009 assessment of infrastructure health (ASCE 2009).

Given reliance on dependable transportation, the public expects continuous availability of safe roadways and bridges. With limited funding for repair/replacement of public works, accurate assessment of the health of our infrastructure and use of information to allocate resources appropriately where they are most needed is important. It is therefore prudent to assess capabilities of existing technologies and explore potential improvements.

In 1997, Chase and Washer provided an assessment of nondestructive evaluation (NDE) for bridge management that focused primarily on inspection needs associated with steel bridges and the assessment of reinforced concrete bridge decks. Detection of fatigue cracks, including weld inspection, was the primary concern for steel bridges, but some information was also provided for bridge substructures and stay cables. Table 1 summarizes the technologies considered in this and other studies.

While Table 1 provides a representative list of technologies, or methods and demonstrations previously published, it is not all inclusive of the results in the public domain. The table does, however, provide an indication of the body of work.

In 2001, the Federal Highway Administration (FHWA) supported a study to evaluate European prestressed concrete segmental and cable-stayed bridges, hoping to learn from Europe's experience given their construction was a decade to two older than similar structures in the US. Factors studied included durability, maintenance/repair/retrofit and replacement practices, and, to some extent, inspection approaches (Podolny et al. 2001). Inspection methods used by European authorities included gamma and x-ray radiography, ultrasonics, electrical resistance, magnetic perturbation, and ground-penetrating radar (GPR), although details of inspection parameters were not provided.

Also in 2001, Phares, contributed to a state-of-the-practice report on highway bridge inspection that considered then-current use of visual inspection to assess bridge health and emerging uses of nondestructive testing (NDT) (Moore et al. 2001). Survey results indicated an increase in the use of NDT compared to responses to a similar survey in 1993 and 1998 (Rens et al. 1997). Details of the methods and applications were not part of this report.

Table 1. Summary of literature results from prior work

Technique	Applications	Summary
Ultrasonic	Detection of fatigue cracks and other cracking in welds	New ultrasonic and magnetic analyzer for cracks (NUMAC), combined ultrasonic testing (UT)/magnetic inspection device in evaluation by the Colorado and Delaware DOTs in 1997 (Chase and Washer 1997)
		Evaluated time-of-flight diffraction for crack detection in steel bridges (Chase and Washer 1997)
	Assessment of stay cable anchorages to locate possible wire breaks	Applied pulse/echo UT to cables within epoxy-grouted portion of 12 anchorages to assess potential of rain/wind vibration-induced damage; anchorages ranged in size from 32 to 72 strands of 1.52 cm diameter with signal path of 1.5 m along the cables (Chase and Washer 1997)
Ground-Penetrating Radar	Location of reinforcing bars	Focus on development of truck-mounted, at traffic-speed, GPR assessment for bridge decks (Chase and Washer 1997)
	Location of post-tension tendons	Field implementation study (FDOT 2003)
	Detection of corrosion damage in dowel bars	Empirical study of chloride contamination of embedded bars (Wimsatt et al. 2009)
	Layer thickness, surface characterization, and moisture estimates in pavements	Evaluated up to 1GHz at highway speeds; issues with data analysis (Wimsatt et al. 2009)
	Characterization of geologic features and materials	Survey of current use of geophysics for natural and artificial foundation materials including bibliography (Sirles 2006)
Infrared Thermography	Delaminations in bare and asphalt-covered concrete	Dual wavelength and image processing used for crack detection; included 1 cm long fatigue crack detection at distance of 60 cm, under paint
	Characterization of the paving process	Infrared methods for characterization of the paving process (Wimsatt et al. 2009)

Technique	Applications	Summary
Laser Vibrometry	Deflection and vibration measurements for bridge modal analysis and damage detection	Measured bridge deflection under controlled loading (Chase and Washer 1997); used for force measurements during construction of the Craig Memorial Bridge in Toledo, Ohio (Ciolke and Mehrabi 2002) and for assessment of potential change in loads as a result of wind/rain vibrations in the Cochrane Bridge in Alabama (26 to 72 strands) (Ciolko and Yen 1999)
Wireless Telemetry	Strain and rotation measurements that transmit data wirelessly	Focus on cost-effective strain gaging for health monitoring, resolution of sub-centimeters (Chase and Washer 1997)
Acoustic Emission	Monitoring fatigue cracks in bridge structural elements	Considered for use during the construction process for quality assurance (Chase and Washer 1997)
Electromagnetic Acoustic Transducers (EMAT)	Applied to steel members to measure strain	(Chase and Washer 1997)
Eddy Current Inspection	Developed differential probe to address issues associated with magnetic properties of steel structures	Showed some success with both conductive and nonconductive coatings (Chase and Washer 1997)
	Alternating current field measurement (ACFM) for detection of cracks in the weld toe	
Magnetic Flux Leakage	Permanent magnet array developed for detection of corrosion or broken cables	(Chase and Washer 1997)
Laser-Optics	Application of laser imaging detection and ranging (LIDaR) to deformation, distance measurement, and aggregate characterization	Potential for continuous monitoring; requires line of sight
Impact-Echo	Detection of voids in grout on post-tensioned bridges	
Embedded Sensors	Embedded microsensor to measure chemical parameters such as acidity-alkalinity, chloride ion concentration, and temperature	Prototype integrated circuit fabricated (Chase and Washer 1997)

Technique	Applications	Summary
Microwave Sensors		Exploratory research for crack detection included assessment of liftoff effects from paint or other surface conditions (Chase and Washer 1997)
Fiber-Optic Sensors	Based on Bragg grating interferometry	Used to measure strains in concrete bridge beams (Chase and Washer 1997)
X-Ray Radiography	X-ray computed tomography (CT) for materials characterization	Applied x-ray CT to concrete and asphalt using 420 keV source and 512 linear array detector to characterize damage progression in concrete and moisture transport in asphalt (Wimsatt et al. 2009, Kear and Leeming 1994, Bligh et al. 1994, Brown and St Leger 2003, Derobert et al. 2002, DMJM Harris 2003, Hussein and Whynot 1989, Mariscotti et al. 2007 and 2009, Martz et al. 1993, Owen 1998, Pimentel et al. 2010, Pinna 2002)
	X-ray backscatter methods for corrosion, cracking, and other damage conditions in a variety of civil structures including pavement, bridges, airports, and water ports	Provides image that can be gathered at speeds up to 5 mph

Two recent reports from the Second Strategic Highway Research Program (SHRP 2) provide an update on usage of NDE (Wimsatt et al. 2009). Wimsatt et al. focused on methods to speed up the inspection process consistent with the SHRP 2 goals to reduce traffic disruption during renewal and reconstruction projects. A study performed on post-tensioned bridges provides insight into the issues associated with field implementation (FDOT 2003).

Deterioration of concrete has been a focus of several studies (Clemena et al. 2000, Al-Qadi et al. 2005). A recent National Cooperative Highway Research Program (NCHRP) synthesis report on geophysics provides useful references for GPR (Sirles 2006). (In Sirles 2006, NDE is distinguished from geophysics as techniques applied to engineered structures rather than geological features or materials, even though there can be considerable overlap between the methods.)

Table 1 provides a summary of the results of prior work tabulating the techniques, applications of those techniques to various civil structures, and a summary of the status. Again, this is not an all-inclusive summary of methods or public domain information. However, it does convey the numerous applications of physics and efforts to optimize those applications for the damage detection and characterization needs of the civil infrastructure community.

There are multiple technical challenges involved with the nation's aging infrastructure that can be addressed by NDE methods. One such challenge involves detecting corrosion damage to reinforcing steel that anchors concrete bridge barrier rails to the road deck of some bridge structures. Moisture and chloride ions reach the reinforcing steel or anchor bolts along the cold joint between the rail and the deck and cause general corrosion that can weaken the performance of the anchors and ultimately the barrier.

This issue was brought to the forefront in August 2008 when a tractor-trailer crashed into a barrier rail and departed from the William Preston Lane, Jr. Memorial Bridge (the Chesapeake Bay Bridge) near Annapolis, Maryland, resulting in a fatality. The crash is well documented by the National Transportation Safety Board (NTSB 2010).

Figure 1 shows the corroded condition of U-bolt anchors from the NTSB recommendations to the FHWA. For this particular bridge construction, it was possible to detect the condition of a fully-fractured anchor using ultrasound techniques; however, the NTSB identified the need to detect intact but degraded anchors as a high priority need.

Figure 1. Corroded conditions of several U-bolt anchors that were extricated from concrete bridge barrier rail (NTSB 2010)

Through a series of discussions between members of the Iowa Department of Transportation (DOT) Office of Bridges and Structures and the researchers in early 2011, the inspection of bridge barrier rails, such as the ones shown in Figure 2, was identified as a high priority issue.

Figure 2. Typical bridge barrier rail construction

Concrete bridge barrier rails provide protection of passing vehicles and are critical to public safety. A cold joint exists between the barrier rail and the bridge deck, either with or without an overlay. At issue is the corrosion of the reinforcing steel within the barrier rail, particularly at the joint of the barrier rail with the bridge deck.

The geometries of interest were defined with interest in two reinforcing steel sizes, 1/2 in. and 3/4 in., either with or without epoxy coatings. Of interest is the ability to detect the presence of corrosion and assess quantititatively the extent of material loss (i.e., the reduction in reinforcing steel diameter). Interest exists in determining when the diameter has been reduced by 25 percent, thereby indicating the need for repair/replacement.

1.2   Research Objectives

The objectives of this research were as follows:

- Provide a comparison of three inspection methods—GPR, magnetic flux leakage (MFL), and radiography—for applicability to bridge barrier rail inspection
- Determine the quantitative capability of each of the methods using controlled laboratory samples
- Provide a preliminary feasibility assessment that includes a limited field test at a typical barrier rail construction bridge

1.3   Project Scope

Given the complexity of detection and quantifcation of buried structures such as reinforcing steel in concrete, there are several potential solutions, which include GPR, MFL, and radiographic inspection. Each method has advantages and disadvantages.

This Phase I feasibility study was completed to compare the sensitivity and cost effectiveness of each of the methods in a laboratory environment. In addition, limited field testing of the GPR and MFL techniques were conducted.

Field testing of the radiographic technique was not planned for this Phase I work due to equipment portability constraints with the short duration of this project. (Recommendations include Phase II field prototype instrument development and a formal test.)

2 SUMMARY OF PRIOR WORK

2.1 Problem Statement

Locating the position of reinforcing steel in concrete structures is a routine procedure with a number of commercial-off-the-shelve (COTS) tools available such as GPR, radiography, and electromagnetic devices (such as the Rebarscope from James Instruments Inc.). While instrumentation and inspection service providers are available to support position verification, the ability to provide quantitative information about the condition of embedded reinforcing bars and other anchoring components, such as anchor bolts, is lacking.

Without quantitative information regarding the extent of degradation, condition-based decisions regarding the repair or replacement of reinforced structures are not feasible. The purpose of this project was to determine the feasibility of generating quantitative data showing extent of material loss and to provide recommendations on the fieldability of these approaches.

2.2 Literature Survey

Initial efforts focused on review of prior applications of each of the methods to reinforcing bar inspection. Radiography involves the use of an x-ray-generating source, which is placed, typically, on one side of the object to be inspected while the detector is placed on the opposite side, for a through-transmission inspection. Traditionally, the detector was radiographic film selected to match the resolution requirements for the component of interest and within the constraints of the inspection time.

Much early work used film as the detector with the primary conclusion being that the status of concrete structures could be determined very well using x-ray film radiography, but that there was a high cost in terms of money and time required for the inspection (Kear and Leeming 1994, Bligh et al. 1994, Brown and St Leger 2003, Derobert et al. 2002, DMJM Harris 2003, Hussein and Whynot 1989, Mariscotti et al. 2007/2009, Marz et al. 1993, Owen 1998, Pimentel et al. 2010, Pinna 2002). Our work on this project demonstrates that the new digital x-ray detectors reduce the costs incurred when using film greatly as discussed in section 3.2.

Previous studies have also shown the potential of electromagnetic NDE techniques for inspecting reinforcing steel and other ferromagnetic components in civil structures (Naito and Jones 2010). Among the techniques, eddy current (EC) methods have been employed in commercial instruments for locating reinforcing steel in concrete (Yu and Khazanovich 2005).

EC operates on the principle that when alternating current is passed through a coil, a changing magnetic field is produced. When this changing field is brought into close proximity to a conductive material, the field will induce a time-varying current that flows in closed circuit in the conductor. The induced EC produces its own magnetic field known as the secondary field, or EC field. The strength and direction of the induced field depends on several factors, including the electrical conductivity and magnetic permeability of the conductor under interrogation, the

amount of conductive material present for the eddy currents to form, and the distance between the conductor and the drive and/or sensing coils.

The latter forms the basis employed in commercial EC instruments for locating reinforcing steel. It is conceivable that any reinforcing steel damage, such as that caused by corrosion, will affect EC flow and lead to a change in EC field or coil impedance, which can be detected and used to characterize the extent of damage (Ciolko and Tabatabai 1999).

Magnetic inspection methods, such as MFL, offer an alternative method for inspecting ferromagnetic components in civil structures (Ghorbanpoor et al. 2000, Jones et al. 2010). MFL is a well-established technique for detecting defects in ferromagnetic materials such as pipeline steel (Blitz 1997).

The technique typically involves the use of an electromagnet or a permanent magnet yoke to magnetize the object being tested. The injected magnetic fluxes tend to flow through the ferromagnetic object as it has a higher permeability than air. Any defect or discontinuity in the test object causes leakage of magnetic fluxes from the object, which can be detected using magnetic field sensors such as Hall effect devices.

The use of MFL for inspecting steel in prestressed concrete members was studied by Kusenberger and Barton (1981) and Sawade and Krause (2007) and was later extended to other on-site inspections (Grosse 2007). Ghorbanpoor et al. developed an MFL sensor using permanent magnets to magnetize steel components in concrete and used the amplitude of detected MFL signals to determine empirically the flaw volume (Ghorbanpoor et al. 2000). DaSilva et al. also reported the use of MFL to estimate the amount of material loss of corroded steel strands in concrete (DaSilva et al. 2009).

In a comparison study of MFL and other NDE techniques, MFL was found to provide the closest and most reliable predictions of damage levels caused by corrosion and fractures (Naito and Jones 2010). Two other closely-related magnetic methods, induced magnetic field (IMF) and residual magnetic field (RMF), have been demonstrated in the laboratory and attempted in the field for detecting flaws or remaining cross-section of steel strands in concrete (Nims and Devabhaktuni 2001, Fernandes et al. 2012, Hillemeir and Scheel 1998, Scheel and Hillemeier 1997).

IMF has been studied regarding its potential use for detecting corrosion damage of pre-stressed strands in concrete up to 1.8 in. thick (Nims and Devabhaktuni 2001). The method utilizes a c-core electromagnet to magnetize steel strands in concrete and Hall effect sensors mounted on the pole surfaces of the electromagnet to measure the amount of magnetic field induced in the strands. The induced field depends on total magnetic reluctance of the magnetic circuit, which in turn depends on permeability and cross-sectional area of the strand. It has been claimed that IMF provides a direct measure of the remaining effective cross-sectional area of steel strands. However, it requires strong magnetization and accurate knowledge of the distance between the strand and the electromagnet (Nims and Devabhaktuni 2001).

The RMF method relies on detecting a residual magnetic field emanating from magnetized components, such as magnetized tendons or steel wires in concrete. RMF operates on the principle that a dipole magnetic field forms near a flaw or fracture, giving rise to a characteristic remnant magnetic leakage field pattern in the surrounding region that can be detected and used for flaw detection. Although RMF is useful in detecting fractures of steel strands, it does not measure the amount of material loss caused by corrosion (Hillemeier and Scheel 1998, Scheel and Hillemeier 1997).

3 TEST AND EVALUATION METHODOLOGY

3.1 Test Specimen Fabrication

Concrete test specimens were fabricated as shown in Figure 3 to represent typical concrete construction thicknesses and materials.
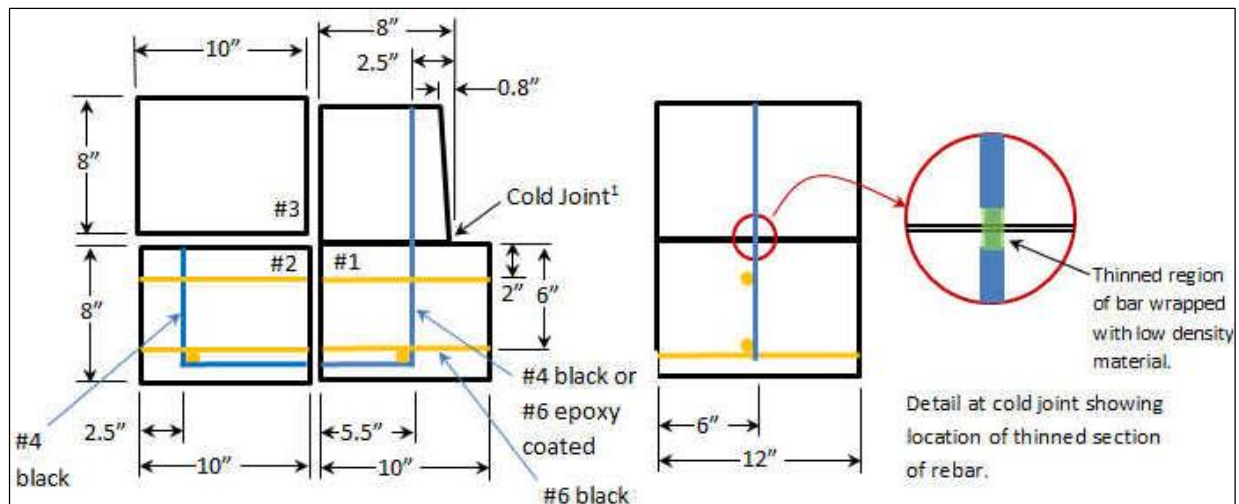
Figure 3. Configuration of test specimens

Simulation of differing levels of reinforcing steel corrosion was achieved by machining away varying amounts of the reinforcing steel's diameter. Five barrier rail test specimens were built, each with reinforcing steel in a different "corroded" condition. Two contained unmodified bare #4 and #6 epoxy-coated reinforcing steel, respectively. The remaining three contained reinforcing steel of which a segment of the steel was machined away to simulate corrosion: two contained bare #4 reinforcing steel with a 25 percent and 50 percent reduction in diameter, respectively, and the last contained epoxy coated #6 reinforcing steel with a 50 percent reduction in diameter. Other concrete blocks were constructed so they could be arranged around the barrier rail specimen in such a way that the combined structure would approximate a bridge barrier rail.

3.2 X-Ray Evaluation

As with prior work, we were able to demonstrate that locating corroded reinforcing steel in concrete bridge barrier rails using an x-ray technique is achieved easily in a laboratory setting. This is consistent with examples using film radiography found in the literature, but we extended the results to include digital radiography, which provides for much faster inspection.

Field tests were not performed due to regulatory and equipment limitations for such a small-scope project. However, these limitations need not prohibit future x-ray inspections of bridge barrier rails, as several references demonstrate. In fact, the use of digital imaging will produce quicker results with reduced radiation risks.

We also used our X-Ray Radiography Simulation (XRSIM) code to assist in optimizing the inspection setup. XRSIM is a tool developed at the Center for NDE over a number of years that allows the user to specify details of source, detection, and object under test and it provided useful guidance for this project.

For evaluation of radiography techniques, the concrete barrier specimens, x-ray source, and detector were configured as shown in Figure 4. The straight shot (for validation) shown on the left is called the reference angle or orientation later in this report. The 60 degree shot is called the realistic angle or orientation.
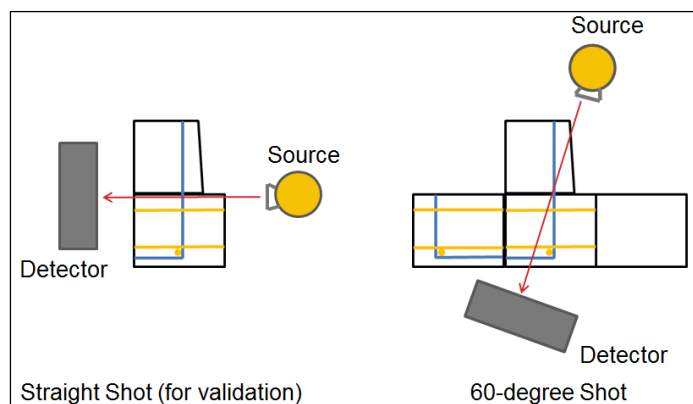
Figure 4. X-ray configuration of reference test and realistic test

Three different x-ray imaging systems were used during this phase of the investigation to determine their relative effectiveness. The three systems were a phosphor screen coupled to a charge-coupled device (CCD) camera, a phosphor plate imager used in computed radiography, and Agfa D7 radiographic film.

The first, and our primary, imaging system was a custom-built digital detector consisting of a cesium iodide (CsI) x-ray conversion screen viewed by a scientific-grade digital camera (CsI detector). The pixel size can be adjusted through use of different lenses and camera settings. For the bridge barrier rail images, we set the pixel size at 0.57 mm and the exposure time at 30 seconds. Commercially-available digital x-ray detectors can be expected to produce similar images, but generally with reduced exposure time.

The second system was the computed radiography (CR) system using a commercial phosphor imaging plate as the detector. The plate we used was a 14 by 17 in. General Electric (GE) IPC2. To read out the image after exposure, the plate is scanned with a laser. A second laser erases the image to prepare the plate for the next exposure. The CR scanner that we used was the GE CR^{x}Flex with 100 micron pixel size and 16-bit dynamic range (see http://www.ge-mcs.com/en/radiography-x-ray/digital-x-ray/crx-flex.html).

Finally, several x-ray film radiographs were captured using Agfa D7 radiographic film. The x-ray film provided a baseline for comparison with previous studies, a baseline for comparison with computer simulation results, and archival media.

The x-ray source used was a 320 kVp Comet x-ray tube operated at 290 kV with the current setting between 1 and 5 mAmps. This was the highest energy source available in our labs for these tests. Ideally, we would like to extend the measurements to higher energy. Concrete test specimens (described in section 3.4.1) were arranged to simulate real-world conditions. X-ray images were obtained in the simplest orientation to verify that the specimens were constructed properly and then in an orientation that represents conditions found typically in the field.

We used XRSIM to aid in the investigation. XRSIM is a computerized model that captures the physics of the generation of x-rays from an x-ray tube, the interactions of these x-rays with the specimen material, and the signal response of the x-ray detector (Xu et al. 1994, Gray et al. 1998). XRSIM can simulate x-ray inspections of any item that can be modeled in a computer-aided design (CAD) package. The CAD model can be reoriented within XRSIM to simulate any desired inspection orientation.

Accurate CAD models were created of all the bridge barrier rail specimens. The x-ray source and detector parameters, along with the physical properties of the concrete and reinforcing steel were included in the XRSIM model. The simulation tool was used first to speed up the early experimental setup by testing several examination angles and x-ray settings. Once the experimental setup was established, we compared the resulting experimental images with predictions from the XRSIM model. This comparison was made for both film and the CsI detector. X-ray film provided a cross-platform validation between laboratory results and the simulations.

A single-sided x-ray inspection would greatly simplify the evaluation of bridge barrier rails. X-ray backscatter imaging, as shown in Figure 5, is an approach that can, in principle, achieve this.
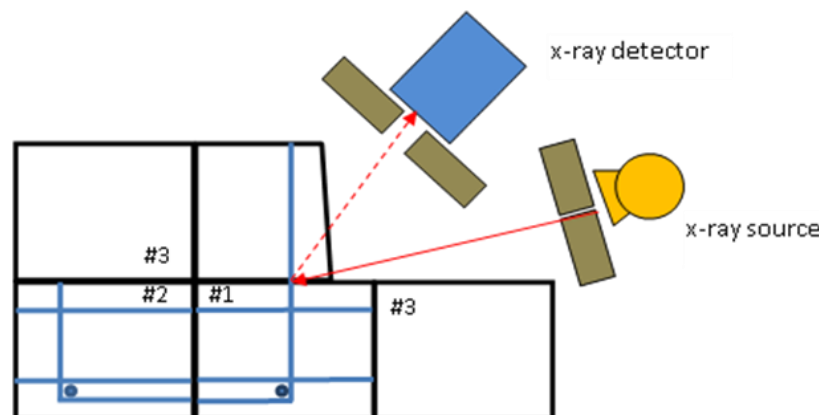
Figure 5. Configuration for back-scatter inspections

The method is used routinely, for example, in screening cargo at border crossings (Callerame 2006) and has been used by the National Aeronautics and Space Administration (NASA) to inspect the space shuttle external rocket (Dugan et al.). To evaluate this method, we set up a tightly-collimated x-ray source and detector as indicated in Figure 6.
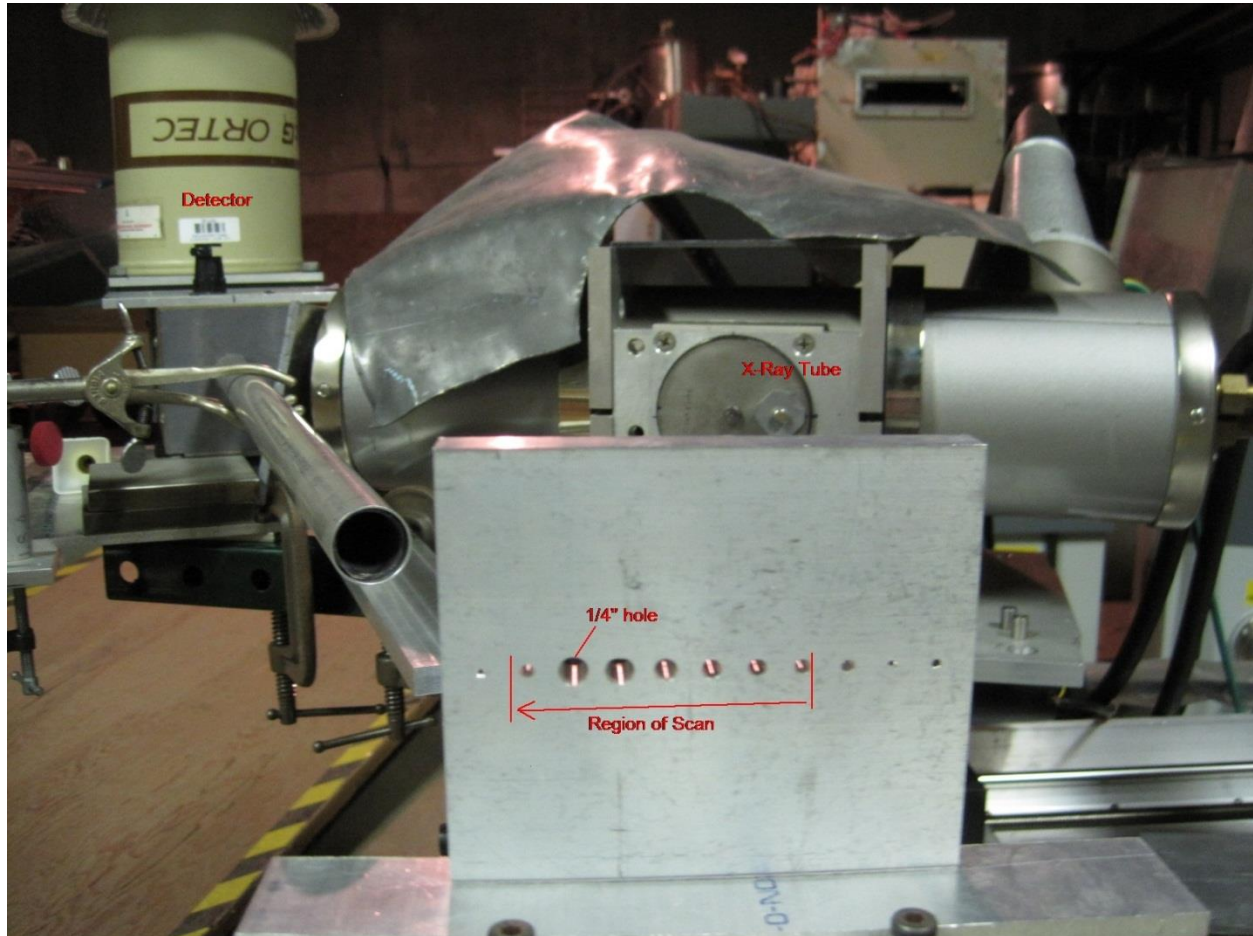
Figure 6. Setup used for x-ray backscatter studies

The diameter of the beam at the position of the specimen was measured to be 3 mm. The input to the detector was collimated with a long stainless steel tube that restricted the angular range of scattered x-rays to +/- 0.8 degrees around a central scattering angle of 148 degrees.

In our tests, we used an energy-sensitive high-purity germanium detector that allowed us to measure the energy of scattered x-rays, thereby providing validation of the scattering mechanism. In addition to scattering from the concrete bridge barrier, we measured backscatter from several samples of known, uniform composition, including aluminum, concrete, and steel. The specimens were placed on a computer-controlled table so that we could scan them through the x-ray beam. The results are discussed in section 4.1.2.

3.3   Evaluation of Electromagnetic Methods

A feasibility study was carried out in three stages to evaluate the potential of EC and MFL for detecting corrosion damage to anchoring reinforcement bars near the cold joint between the deck and barrier rails of bridges. In the first stage of the study, EC and MFL measurements were carried out on standalone #4 reinforcing steel with and without artificial defects of 25 percent and 50 percent material loss, using a commercial EC-based reinforcing steel locator and an MFL system that was developed by using GMR sensors to detect leakage fluxes from defects in reinforcing steel.

Both measurement techniques can detect the reinforcing steel readily at a distance of 2.5 in. The amplitudes of the EC and MFL signals vary monotonically with the amount of material loss, indicating the potential of using the techniques to quantify material loss of standalone reinforcing steel.

In the second stage of this evaluation, EC and MFL measurements were conducted on concrete test specimens described in section 3.1. Both EC and MFL signals were found to be affected by horizontal reinforcing steel underneath the cold joint. Nevertheless, the signals detected away from the interfering reinforcing steel are dependent on the amount of material loss of the vertical anchoring reinforcing steel near the cold joint, suggesting the possibility of using the techniques to detect reinforcing steel damage in bridge structures.

In the third stage of this feasibility study, a field test was carried out on Iowa Highway 210 over Interstate 35 (I-35) with the aim to evaluate the techniques in field conditions where the actual arrangement of reinforcing steel could be more complicated.

MFL line scans were performed across 18 reinforcing bar locations selected from four different sections of the bridge. The MFL signals measured by scanning the probe on the deck and at a height of 1.5 in. above the deck were compared. Thirteen inspected reinforcing bars show stronger off-deck MFL signals, suggesting possible damage in those reinforcing bars based on the test results obtained from the concrete test specimens, which show a larger signal in the presence of a defect.

The MFL tests give the same indications of the reinforcing steel condition as the GPR method discussed later for 16 of the 18 inspected reinforcing bar locations. The consistency between the MFL and GPR field test results indicates the potential of the methods for field inspection. Further study is recommended to validate the capability of MFL and GPR for detecting reinforcing steel damage, by using concrete structures that will be dissected and examined for damage, and to develop the techniques further for quantifying material loss.

3.4 Evaluation of Ground-Penetrating Radar Methods

GPR is routinely used to locate and map reinforcing steel in concrete structures. Detecting damage to embedded reinforcing steel is a much more difficult challenge. The equipment used for our measurements is shown in Figure 7.
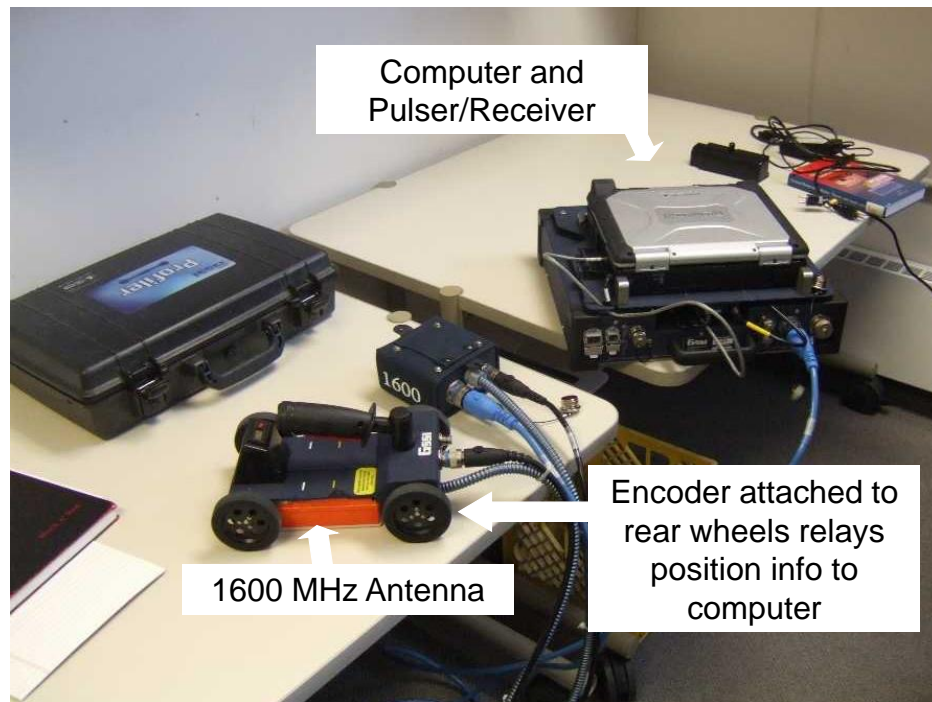
Figure 7. Portable GPR equipment used

This is a commercially-available, portable, battery-operated GPR unit manufactured by Geophysical Survey Systems, Inc. (GSSI). The operation of the GPR unit for reinforcing steel inspection is illustrated in Figure 8.

The pulser portion of the pulser/receiver sends a voltage pulse along the coaxial cable leading to the antenna. This produces a short-duration electromagnetic (EM) pulse radiated by the antenna. Some of this radiated EM energy strikes an embedded reinforcing steel and is reflected back toward the antenna. There, it is received, resulting in an output voltage signal in the coaxial cable, which is then amplified by the receiver electronics and displayed on the computer monitor.

As indicated in Figure 8, the GPR inspection process is analogous to that used in pulse/echo ultrasonic inspection, and tools developed on the ultrasonic side for analyzing data and modeling inspections can be adapted readily to GPR.

GPR Pulse/Echo Setup

Computer

Pulser / Receiver

Scan

Antenna

Air

Concrete

Path followed by a short duration EM pulse

Rebar (Seen end-on)

Antenna field extent

Analogy with UT

UT	GPR
Transducer	Antenna (dipole-like)
Wave speed depends on density, stiffness.	Wave speed depends on EM properties (permittivity, permeability)

For both, raw data is response (V) vs time

For both, Snell's Law governs refraction

For both, one can define "impedance" such that impedance change governs reflection/transmission of plane waves at flat boundaries.

For both, attenuation occurs during propagation due to scattering and absorption.

Figure 8. GPR pulse/echo inspection of reinforcing steel and analogy with ultrasonic inspection

For a one-dimensional scan of the antenna, a standard GPR display is referred to as a B-scan (with an example shown in Figure 9b). The horizontal axis indicates the antenna position, while the vertical axis displays either signal arrival time or inferred penetration depth. The gray-scale image then depicts echo strength, with white depicting a strong positive voltage value and black depicting a strong negative voltage.

The signal-voltage-versus-arrival-time plot observed at any fixed antenna position is called an A-scan or wiggle plot (with an example shown in Figure 9e). For the standard 1600 MHz antenna we are using, the EM radiation is in the microwave band. The wave speed and wavelength in concrete depend on the dielectric constant of the concrete, which varies somewhat for different grades of material. Typically, the wavelength in concrete is about a few inches, and the reinforcing steel diameter is thus smaller than either the EM wavelength or the broadcast envelope (radiation pattern size) of the antenna.

When the antenna is scanned across a concrete fixture containing reinforcing steel (Figure 9a), the reinforcing steel is sensed at many different antenna positions. The arrival time of the reinforcing steel echo depends on the distance between the antenna and the reinforcing steel, being smallest when the antenna is directly above the reinforcing steel. Because of the dependence of echo arrival time on antenna position, regions of high reflected amplitude in B-scans have a hyperbola-like shape as illustrated in Figure 9d. The slope of the hyperbola's asymptote depends on the EM wave speed in concrete, and a measurement of that slope can be

used to infer the wave speed and hence the dielectric constant of concrete on which the wave speed depends. This will be explicitly demonstrated later.
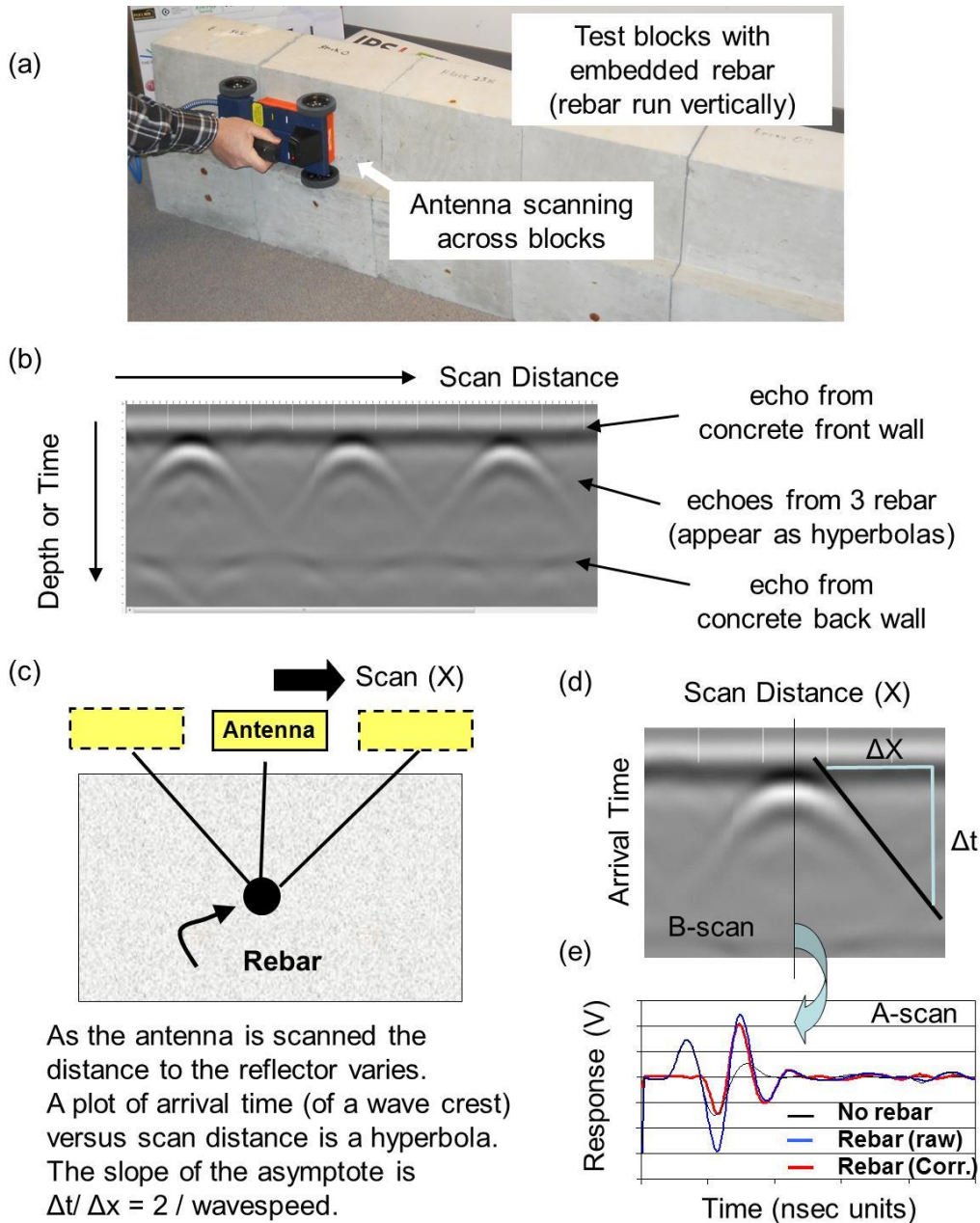
Figure 9. Scan of the GPR antenna, the resulting B-scan image, why B-scan responses have a hyperbola shape, and A-scan plot of output voltage versus time for the antenna position

Figure 9a shows the GPR antenna being run across three abutting test blocks, each containing one embedded reinforcing bar, to obtain a scan and Figure 9b shows the resulting B-scan image. Figures 9c and 9d show why reinforcing steel B-scan responses have a characteristic hyperbola shape. Figure 9e shows the GPR A-scan plot of output voltage versus time for the antenna position indicated by the vertical black line in Figure 9d.

In some practical cases of interest, the echo from the reinforcing steel partially overlaps the earlier-arriving echo from the air/concrete interface immediately below the antenna. There, researchers can use analysis tools to subtract the air/concrete echo, resulting in a reinforcing steel only A-scan, as demonstrated in Figure 9e.

4 TEST AND EVALUATION RESULTS

4.1 X-Ray Evaluation

4.1.1 Conventional Radiography

The concrete test specimens described in section 3.1 were examined by placing them on a table that allowed easy adjustment to obtain the two angles (straight shot for validation or reference and 60 degree realistic shot) shown earlier in Figure 4. In the straight shot, the x-ray path length through the concrete is less, which allowed us to verify the construction of the specimen and the extent of simulated corrosion. The orientation of the different reinforcing steel components is fairly easy to interpret in these images, as they are either along the beam axis or perpendicular to it. This reference image appears on the left in the figures that follow.

The 60 degree shot is more realistic for a field inspection. It requires higher x-ray intensities because of more concrete to penetrate. The resulting image is more difficult to understand due to the complicated geometry with multiple reinforcing bars at different depths. What are actually perpendicular reinforcing bars appear to be parallel in the projection images. This can lead to overlap with the reinforcing steel of interest and greater difficulty in interpreting the results. When this occurs in the field, it may be necessary to reposition the equipment to obtain additional images that give a clearer picture of the reinforcing steel of interest.

The digital images are recorded with a 16 bit dynamic range (65,536 grayscale values). For viewing on a computer screen, this data is windowed and compressed into 256 grayscale levels. That is why some regions of the images appear underexposed while other regions appear overexposed. The amount of corrosion can be quantified by counting the number of pixels that represent a full diameter compared to the reduced diameter of the corroded reinforcing steel. Digital detectors can be calibrated to allow the operator to measure the remaining diameter of the corroded reinforcing steel with relative accuracy (within about 10 percent or better).

Figures 10 through 14 display the images obtained for the five different barrier specimens using the CsI detector. As mentioned above, the reference images (on the left in the figures at x-ray settings of 290 kV, 30 sec, 1.6 mA) show very clearly the geometry of the specimens and give a clear picture of the corroded regions. For these images, there are basically two thicknesses of concrete that differ by about 25 percent. As a result, the dynamic range of the image can be set to capture the entire length of the reinforcing steel with good contrast.

The stone aggregate in the concrete produces a mottled look due to varying density. In some images, white horizontal bands indicate where a layer of plastic was placed to simulate a cold joint. Bright regions around some of the corroded sections show where there has been a loss of material.

The vertical reinforcing steel is the one of interest in these specimens. In some cases, it is noted that the reinforcing steel is tilted at a small angle. Two dark regions near the bottom of the image

correspond to reinforcing steel that is oriented perpendicular to the image plane. In the reference images, they are seen almost end on, though it is noted that some are tilted at different angles. In the images for the more realistic orientation, reinforcing bars that are physically perpendicular to each other appear parallel in the x-ray projections.

In some cases (particularly Figure 14), the projections can overlap, making it difficult to determine the status of a particular reinforcing bar. If such an image were observed in the field, it would be necessary to reposition the source and detector to obtain a different projection that enabled the two to be separated.

Only a limited range of the realistic images on the right (x-ray settings of 290 kV, 30 sec, 5 mA) appear to have good contrast. This is because the x-ray path length varies considerably from top to bottom of the image. The display has been optimized to emphasize the region where the corrosion is located. If desired, we could adjust the display settings to emphasize a different region. Still, the contrast is more limited than in the examples for the reference orientation on the left. We also found it was necessary to use lead to block some of the thinner regions of concrete to prevent a very high intensity signal from washing out an adjacent darker region.
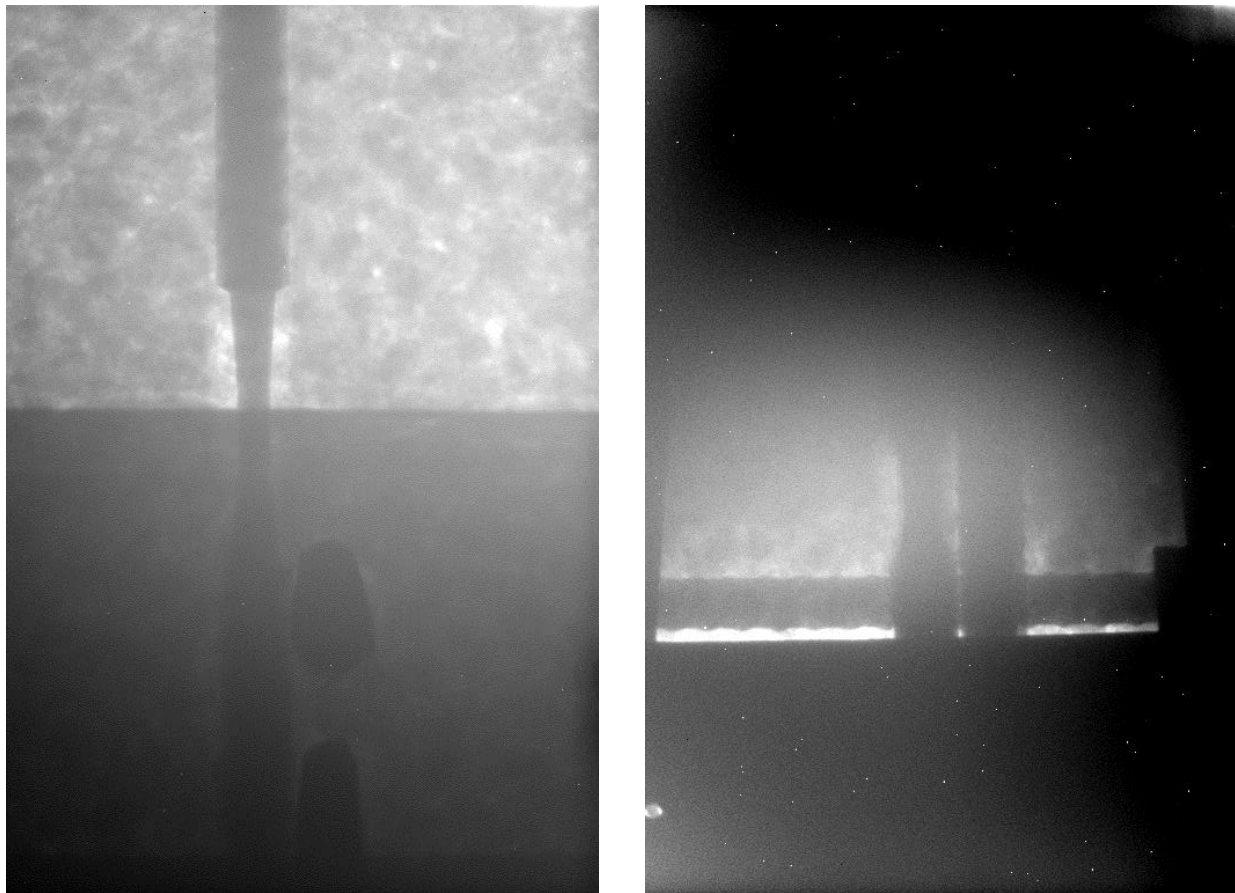
Figure 10. #6 Epoxy-coated reinforcing steel with simulated 50 percent corrosion loss at reference (left) and realistic (right) angles
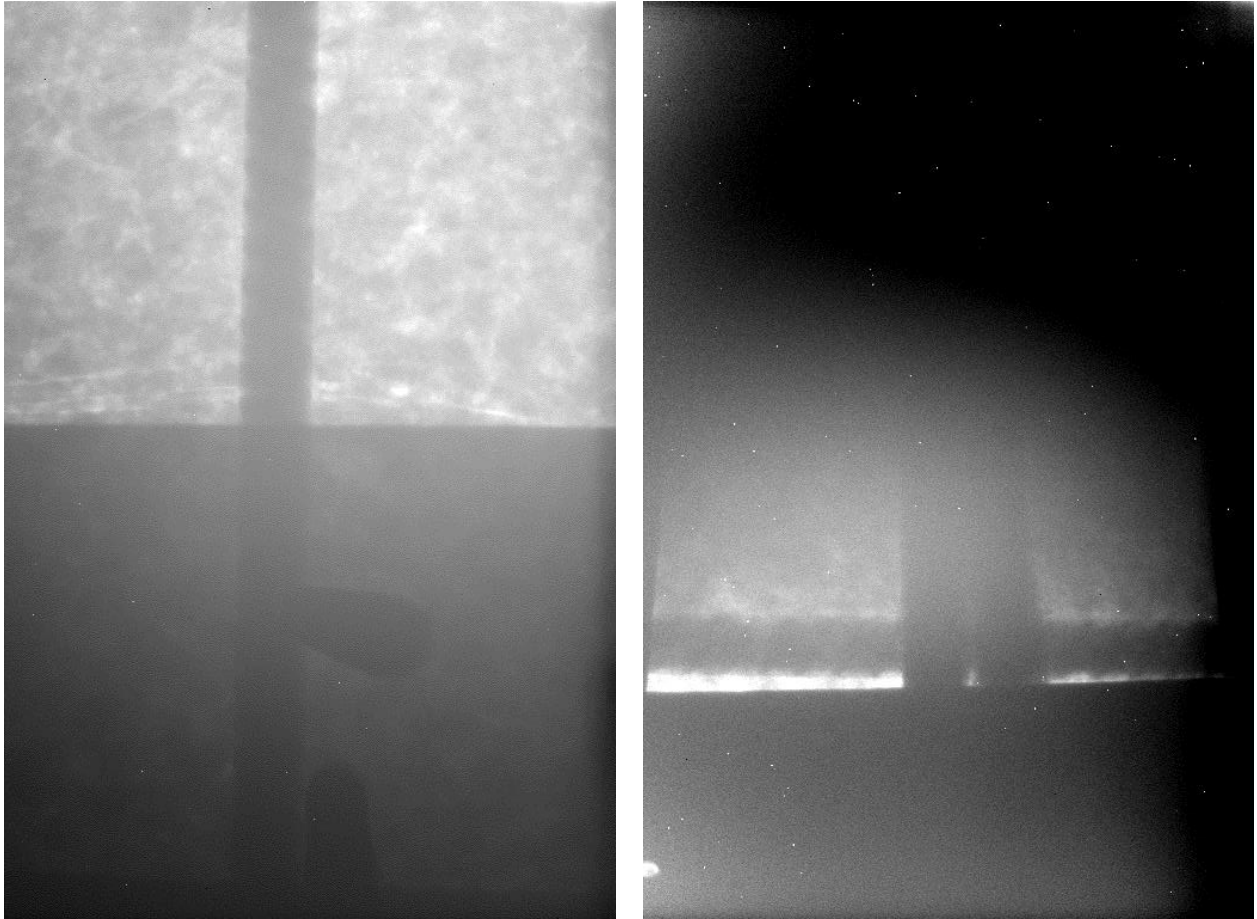
Figure 11. #6 Epoxy-coated reinforcing steel with 0 percent corrosion loss at reference (left) and realistic (right) angles
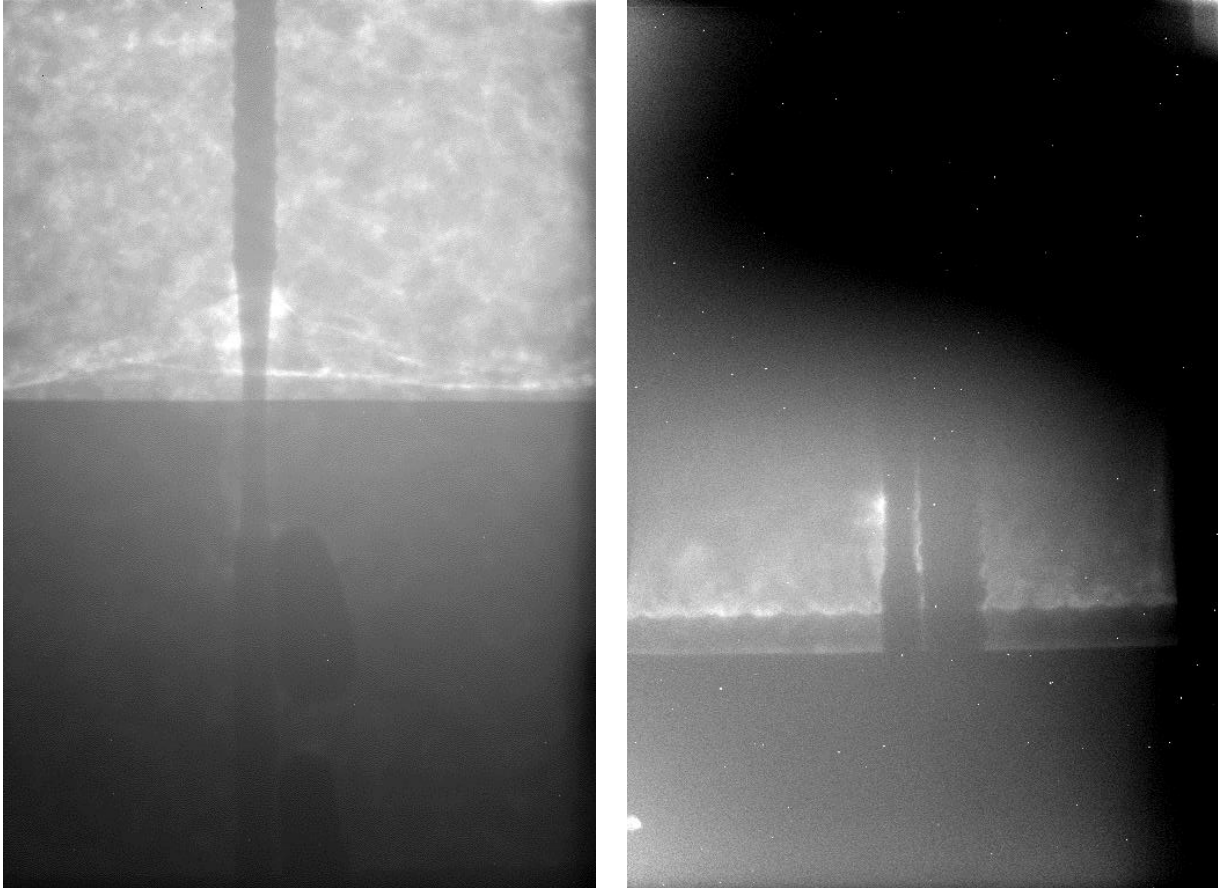
Figure 12. #4 Reinforcing steel with simulated 50 percent corrosion loss at reference (left) and realistic (right) angles
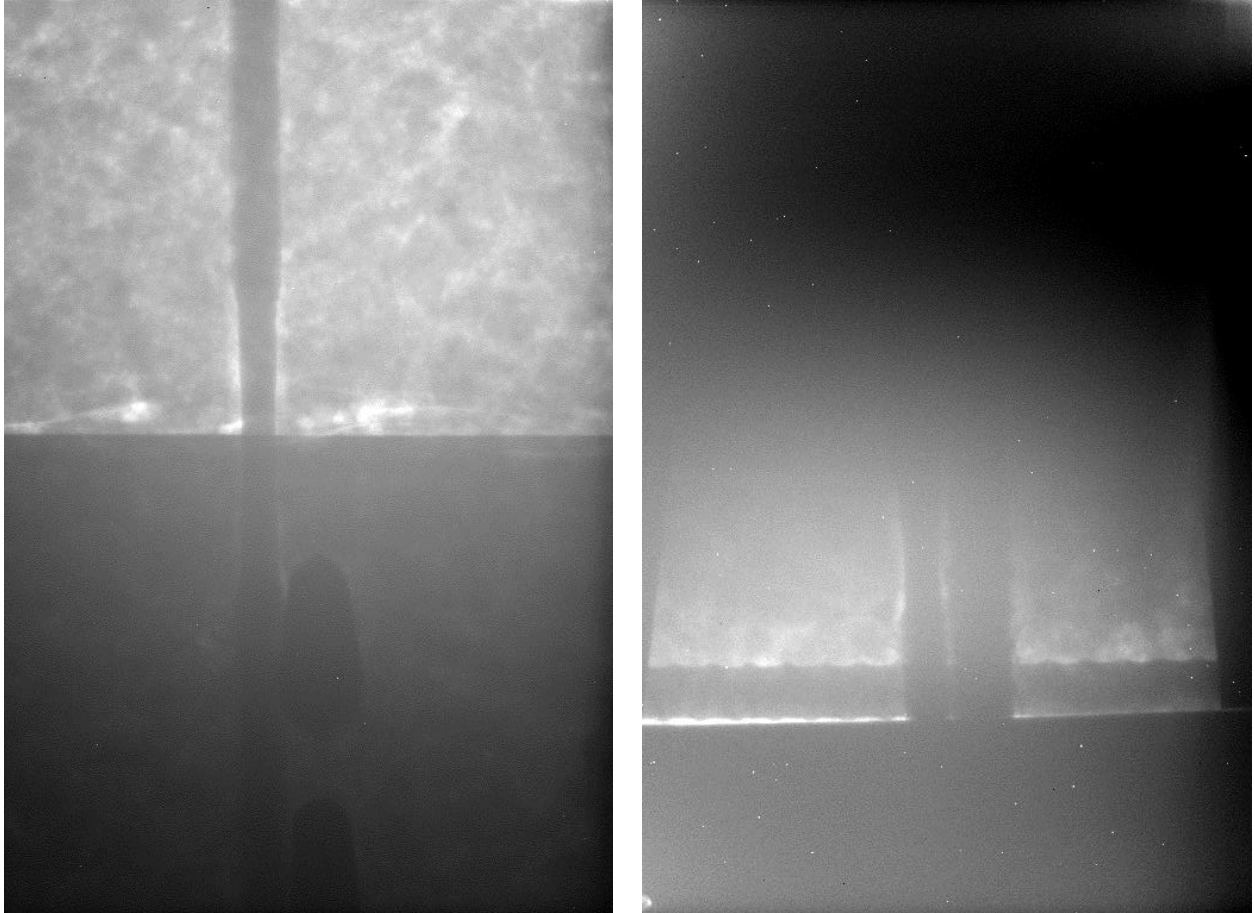
Figure 13. #4 Reinforcing steel with simulated 25 percent corrosion loss at reference (left) and realistic (right) angles
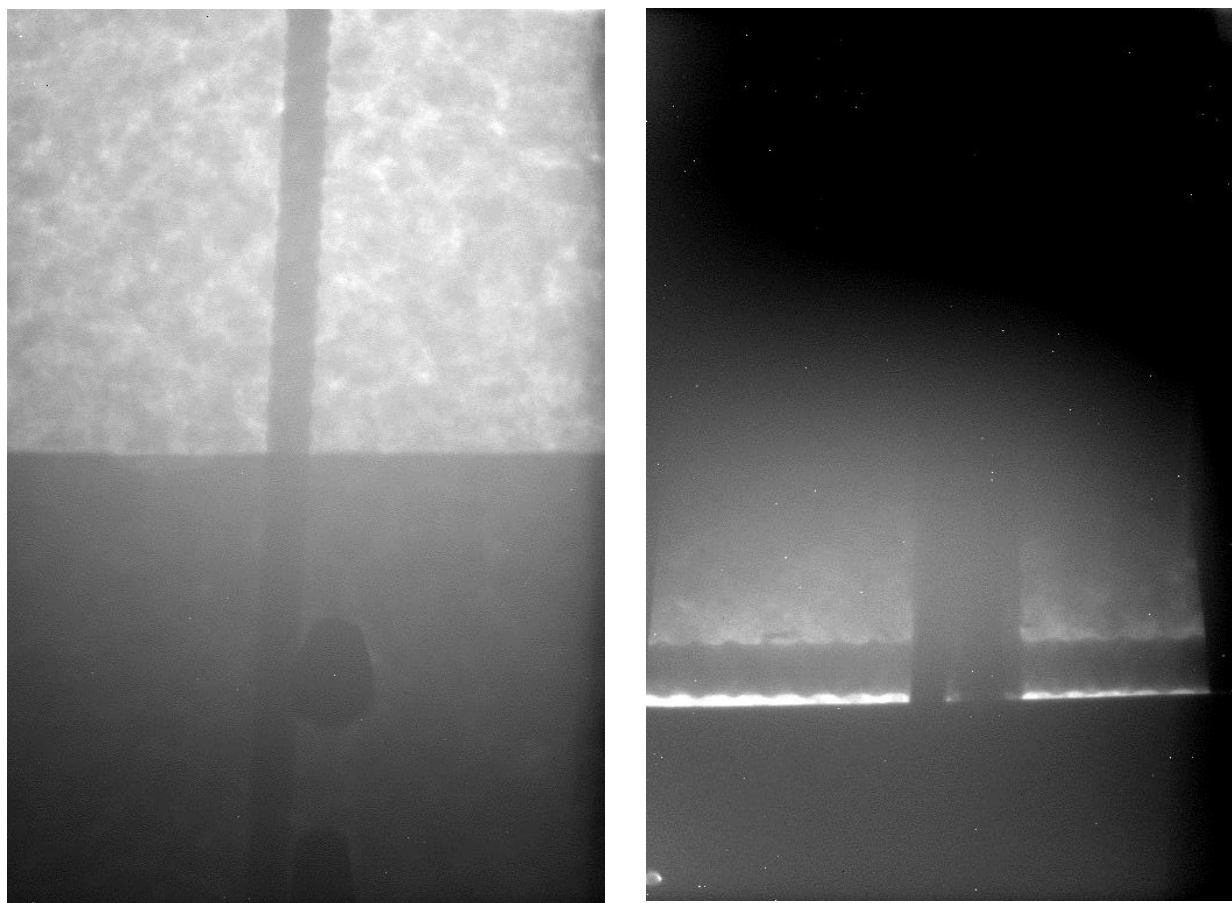
Figure 14. #4 Reinforcing steel with 0 percent corrosion loss at reference (left) and realistic (right) angles

There are several different varieties of digital x-ray imagers on the market. To compare a second type, we took advantage of demonstrations of the CR technique that a vendor was performing at our laboratory.

CR exposure procedures are very similar to those for film. The phosphor screen is placed in a light-tight cassette and positioned opposite the x-ray tube. Exposure times are generally much shorter than for film, though, and chemical development is not required. Instead, a laser scanner reads the latent image stored in the phosphor and produces a digital image in less than a minute. Total time to obtain an image is typically less than five minutes. Figure 15 shows an example of one of the images obtained using the GE ICP2 phosphor plate and the GE CR^{x}Flex reader (with x-ray settings of 290 kV, 3 minutes, 2 mA).

Comparing the image in Figure 15 to the corresponding reference image on the left in Figure 12, it can be seen that the two methods produce comparable results. Because the CR system was on loan for a demonstration, there was not sufficient time to set up the more realistic geometry (60 degree shot) and varying conditions.
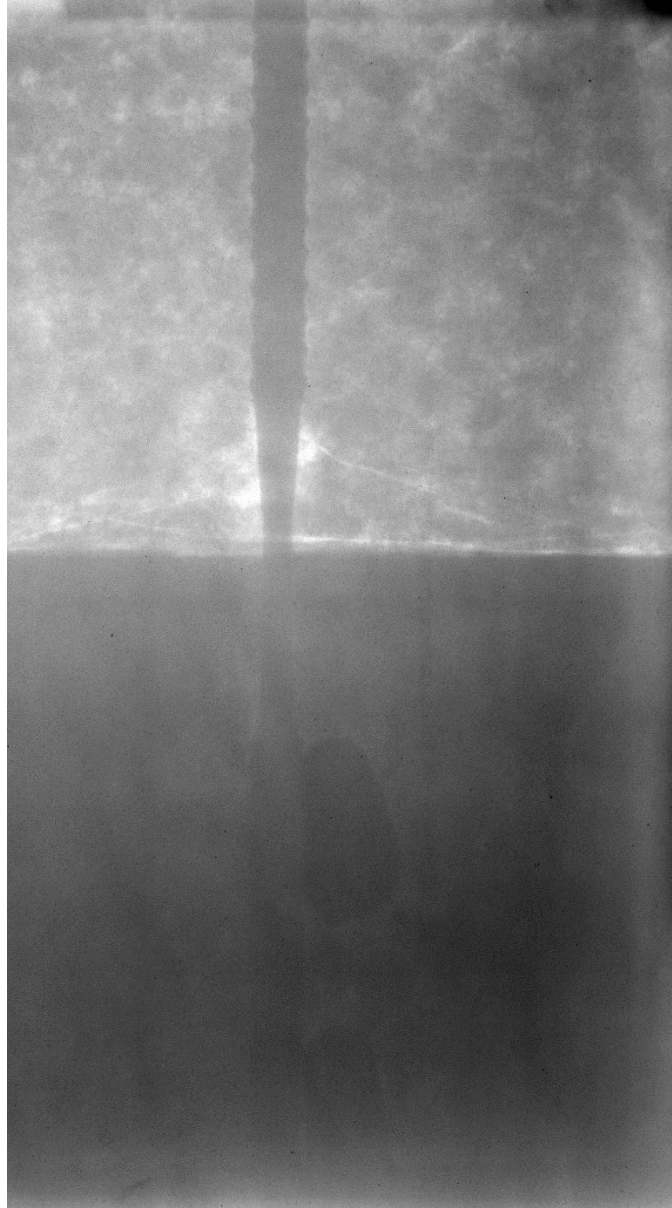
Figure 15. #4 Reinforcing steel with 50 percent corrosion loss at reference angle

For comparison with traditional film radiography methods, we imaged the specimen with #4 reinforcing steel with 25 percent corrosion. The resulting image (digitized with x-ray settings of 290 kV, Agfa D7 film, 15 minutes, and 5 mA) in Figure 16, compares favorably with the corresponding reference image on the left in Figure 13. Note that in the film exposure, lighter areas represent thicker concrete or denser reinforcing steel. The total time for exposure and development was about 30 minutes.
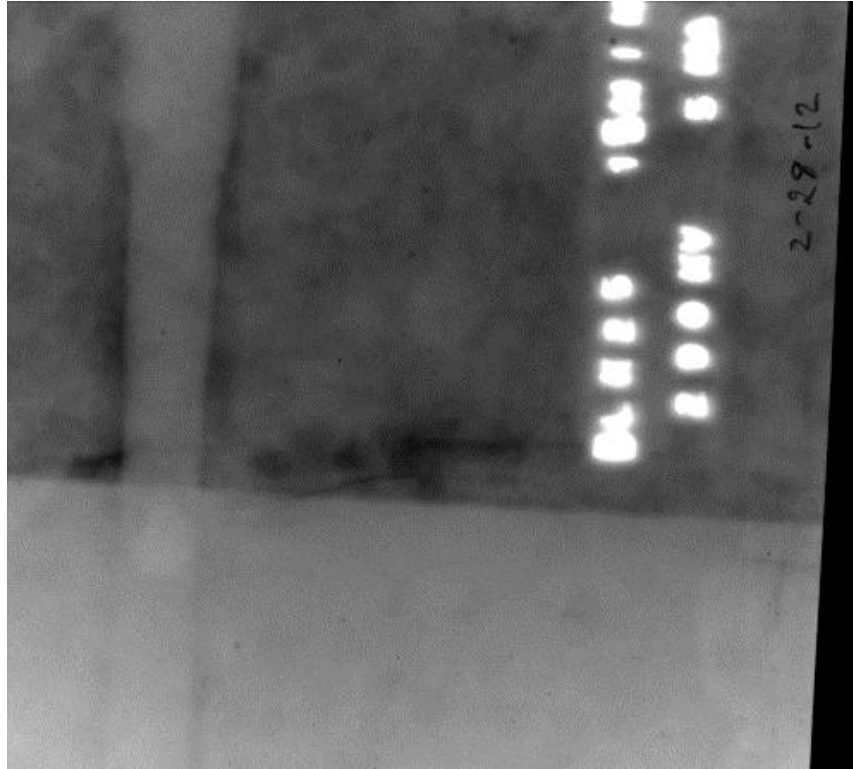
Figure 16. #4 Reinforcing steel with simulated 25 percent corrosion loss at reference angle

In parallel with the laboratory activities capturing the various x-ray images, we used the XRSIM program to simulate radiography of the various specimens at different orientations using different detectors. Figure 17 shows a screen capture of a typical XRSIM simulation for the concrete bridge barrier rail model.

The detector selected for this run was the Agfa D7 film (with x-ray setting of 290 kV). The setup orientation (reference angle) of the CAD model and x-ray tube are shown in the middle left side of the screen, and the simulated x-ray image on the right.

Figures 18 and 19 show simulations of the reference and realistic angles, respectively. For these images, the CsI screen and camera detector system (with x-ray setting of 290 kV) was modeled. Note that the contrast in the region of the reduced diameter is greater in the simulations because there is no material filling the void, whereas the specimens contained a low-density filler material around the simulated corrosion. The simulated reinforcing steel does not include any ribbing. In addition, the simulated images do not have a mottled appearance because the concrete is modeled using the average density for concrete and the aggregate is not included.
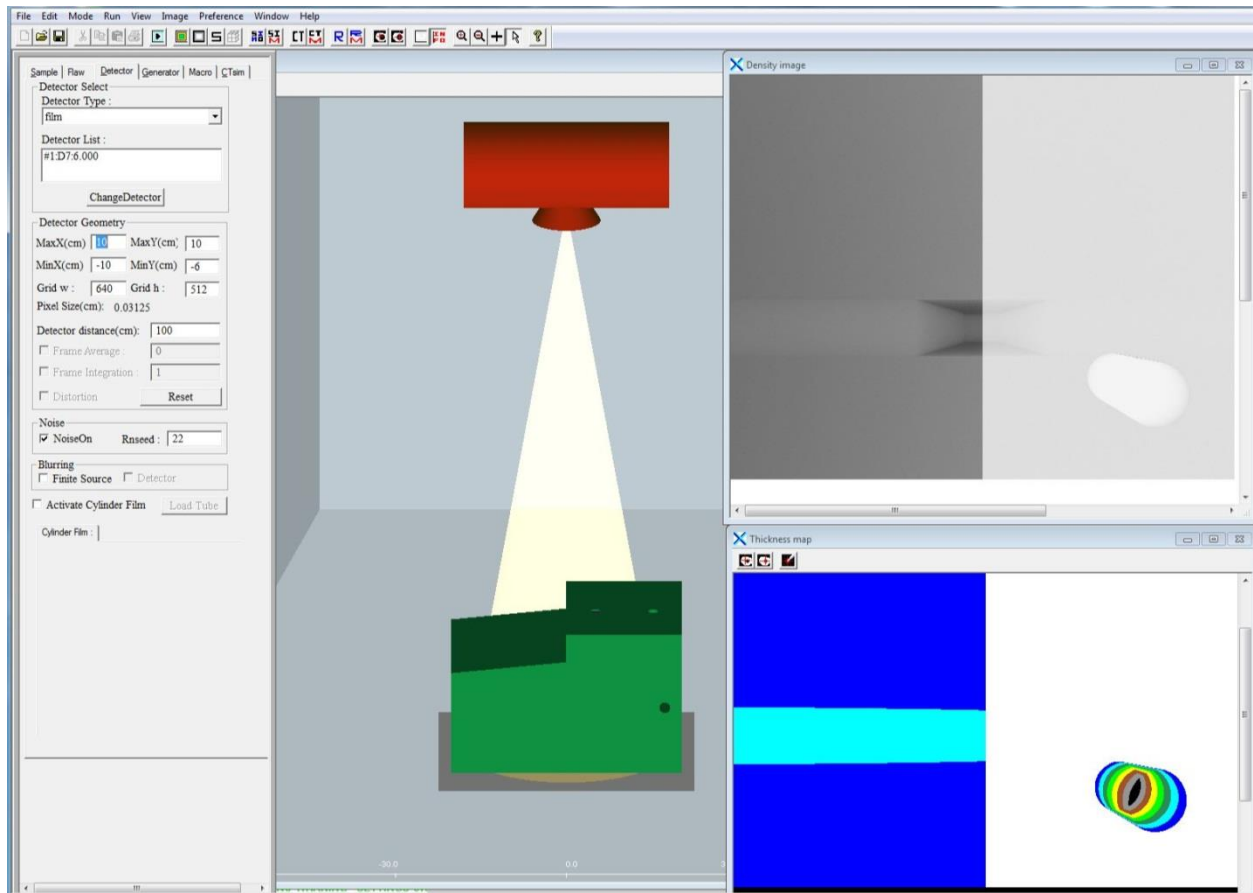
Figure 17. #4 Reinforcing steel with 50 percent corrosion loss at reference angle

These results agree with the geometry observed in the experimental images, although the intensity and contrast do not match very well. For such thick materials, x-ray scattering dominates the processes that produce the image. We have validated the XRSIM model for up to 6 in. of aluminum and up to 3 in. of steel, but not for the 8 in. or more of concrete as is the case in these specimens and would be typical of bridge barrier rails. The results from these tests point to further work that is needed in developing the scattering model for concrete, which is outside the scope of this project.
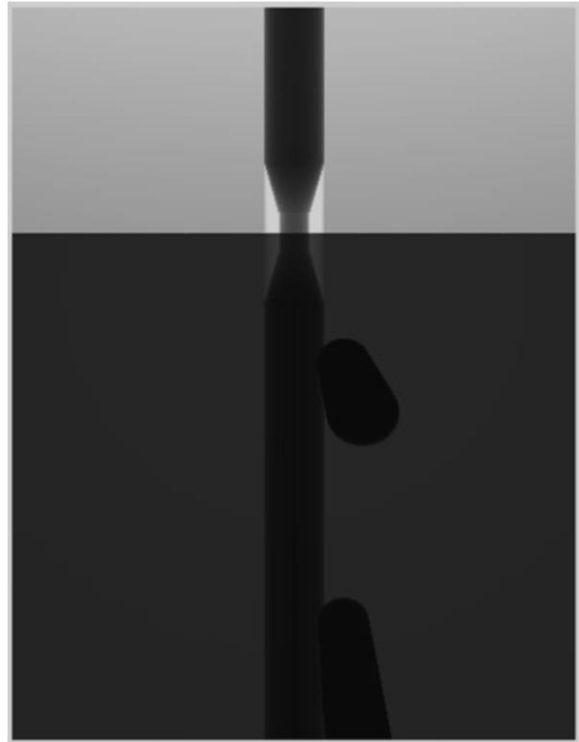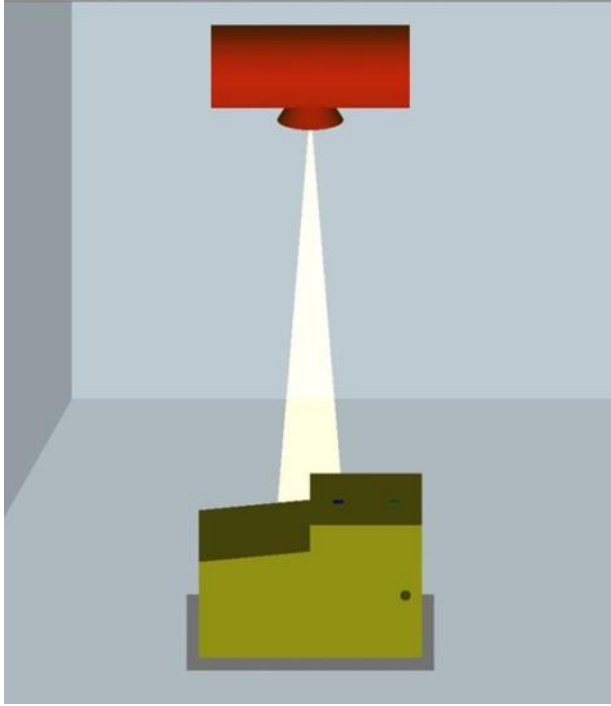
Figure 18. #6 reinforcing steel with 50 percent corrosion loss at reference angle
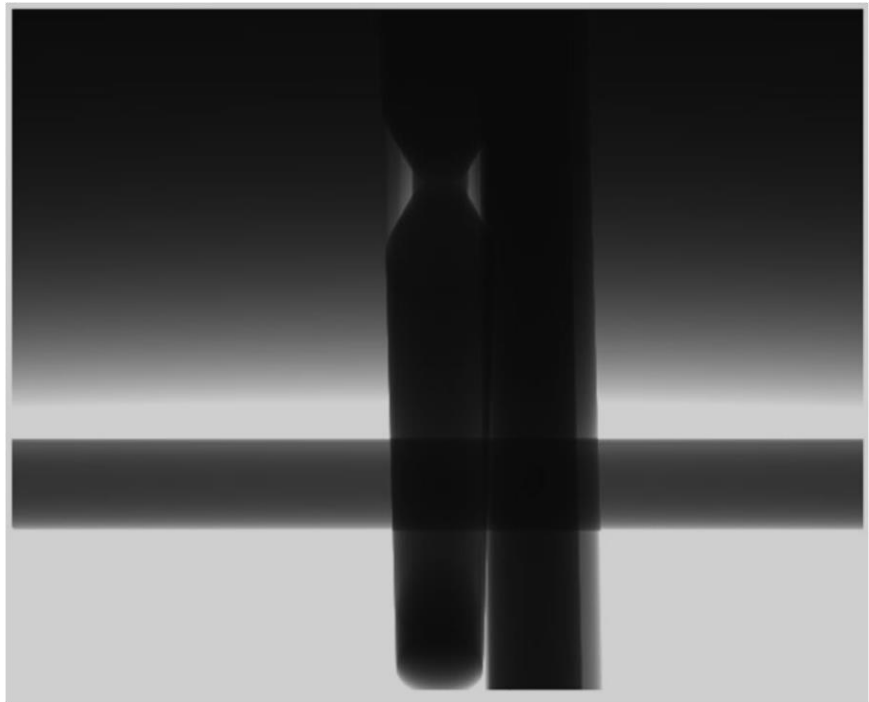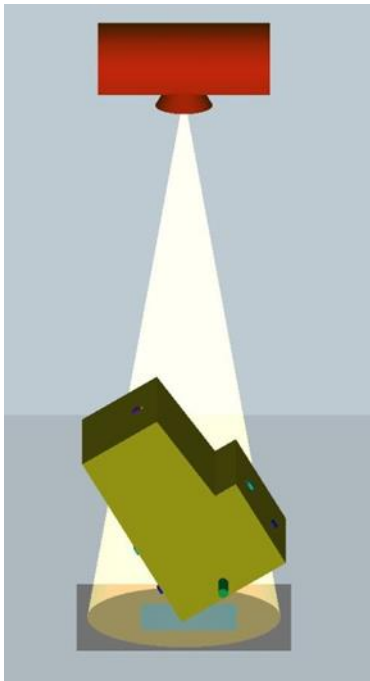
Figure 19. #4 Reinforcing steel with 50 percent corrosion loss at realistic angle

4.1.2   X-Ray Backscatter Studies of Reinforcing Steel Corrosion in Concrete

Some very preliminary studies of x-ray backscatter were carried out using the configuration shown earlier in Figure 5. Comparison of the x-ray spectra observed for scattering from concrete and steel is shown in Figure 20.
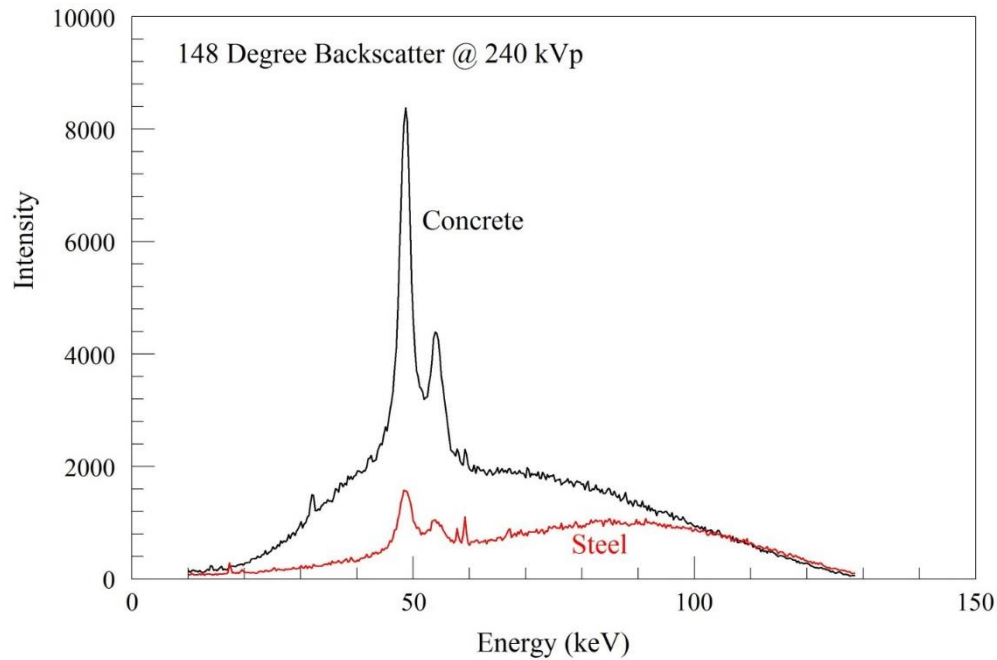
Figure 20. Backscatter spectra observed for concrete and steel samples

Both show the shift in energy expected from the Compton scattering of x-rays at 148 degrees. In particular, the characteristic peaks from the tungsten target in the x-ray tube and the endpoint of the spectra at 130 keV are as predicted. Note that backscattering from steel at low energies is strongly attenuated relative to that from concrete. This would imply good contrast between the two in backscatter imaging.

However, the above spectra were obtained at relatively small depths in the samples. As the inspection point moves deeper into the sample, most low-energy x-rays are absorbed, regardless of material. At the higher energies, the contrast between materials is not as great. To test the effect of material thickness on contrast, we used a sample consisting of a 1/2 in. thick aluminum plate with a series of holes drilled in it (as shown earlier in Figure 6). We then placed different amounts of aluminum in front of this plate as we scanned the beam across the holes. The results are shown in Figure 21. With 2 in. of aluminum in front of the plate, the contrast is greatly reduced.
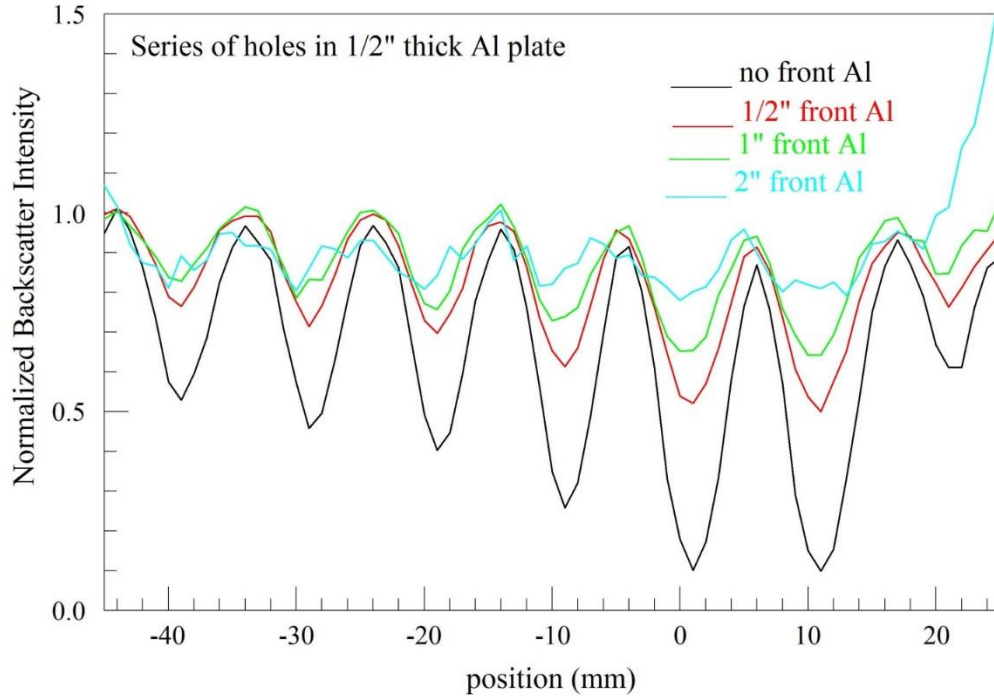
Figure 21. X-ray backscatter contrast at detector as a function of material thickness

The reinforcing steel in the bridge barriers is about 2.5 in. from the concrete surface at the point of the joint. Furthermore, concrete has a density similar to aluminum. The tests on aluminum predict that it will be difficult to obtain good contrast for observing deterioration of reinforcing steel using backscatter x-ray at the energy levels available with existing Center for Nondestructive Evaluation (CNDE) hardware.

During several scans across the region of the bridge barrier specimen where the reinforcing steel was located, we were not able to obtain a convincing signal for the reinforcing steel. As the transmission radiographs indicate, there is variation in the density of the concrete itself that causes further reduction in contrast. We did not observe any improvement with voltages up to 290 kVp. Further studies of this technique will require an x-ray source of higher energy.

4.2   Electromagnetic Methods

Two electromagnetic methods, EC and MFL, were chosen for the feasibility study in view of their potential as non-contact techniques for detecting defects in ferromagnetic components. Given the short duration of the project, it was decided to use commercially-available instrumentation, if available, for the study. A commercial reinforcing steel locator (Rebarscope III from James Instruments, Inc.) was acquired and its potential for detecting material loss in reinforcing steel was evaluated.

Commercial reinforcing steel locators are used primarily for determining the thickness of concrete cover typically up to a few inches. Some instruments can also measure the reinforcing

steel diameter with the resolution of one reinforcing steel size (i.e., 1/8 in. or 3.2 mm), although they are not intended for measuring material loss. However, if the size and depth of the reinforcing steel can be accurately determined by EC, it is perceivable that the technique can be developed further for detecting corrosion damage.

Commercial MFL systems are almost exclusively designed for specific NDE applications (e.g., pipeline inspections), with sensor probe designs and instrumentation optimized for the given inspection geometries and sensitivity needs (e.g., minimum detectable defect size). In view of this, an MFL sensor probe was designed and fabricated specifically for detecting reinforcing steel damage near the cold joint according to the inspection geometry shown in Figure 22.

Figure 22. (a) Bare #4 reinforcing steel specimens and (b) concrete test specimens consisting of either #4 or epoxy-coated #6 reinforcing steel

In this task, the feasibility study was carried out in three stages:

- Stage 1: Laboratory tests on bare, standalone reinforcing steel with or without artificial defects – The aims were to evaluate the sensitivity and limitations (e.g., depth range) of the EC and MFL techniques and to improve the MFL probe design and instrumentation if needed

- Stage 2: Laboratory tests on concrete test specimens containing multiple #4 (0.5 in. diameter) or #6 (3/4 in. diameter) reinforcing steel with or without artificial defects – The aim was to assess the effects of other nearby reinforcing steel in the barrier rail structure on EC and MFL defect signals from the vertical anchoring reinforcing steel

- Stage 3: A field test on the Highway 210 Bridge over I-35 barrier rails – The aims were to evaluate the techniques in field conditions where the actual arrangement of reinforcing steel could be more complicated and to identify areas for further development with regard to portability, inspection speed, and ease of use of the techniques

Three bare, 24 in. long #4 reinforcing bars with a nominal diameter of 0.5 in. were used in Stage 1 of the feasibility study. Two of the bars were machined to create artificial defects that correspond to approximately 25 percent and 50 percent material loss (see Figure 22a). The

diameter and length of the defects are shown in Table 2 for specimens R-2 and R-3, which were machined to produce artificial defects of 25 and 50 percent material loss, respectively. The length (L) and diameter (D) of the machined regions are given in Table 2.

Table 2. Dimensions of the artificial defects in bare #4 reinforcing steel

	Defect Dimensions	
Reinforcing steel specimen	Diameter D (in.)	Length L (in.)
R-2 (25% loss)	0.37	0.555
R-3 (50% loss)	0.25	0.533

Five concrete test specimens prepared in this project were used in the Stage 2 study. Three specimens contained #4 reinforcing steel, with two of the reinforcing bars machined to produce 25 percent and 50 percent material loss. The other two specimens contained epoxy-coated #6 reinforcing steel, with one machined to give a 50 percent material loss. The reinforcing steel sizes and amount of material loss are shown in Table 3.

Table 3. Concrete test specimens used in the Stage 2 study

Specimen	M1	M2	M3	M4	M5
Reinforcing steel	#4[+]	#4	#4	#6[*]	**#6**
Material loss	**0%**	**25%**	**50%**	**0%**	**50%**

[+] Nominal diameter = 0.5 in. (12.7 mm)
[*] Epoxy-coated #6 reinforcing steel with a nominal diameter of 0.75 in. (19.1 mm)

4.2.1   Commercial Eddy Current Instrument – Reinforcing Steel Locator

A commercial EC-based reinforcing steel locator (Rebarscope III from James Instruments, Inc.) was used in this study. The instrument is typically used for locating reinforcing steel inside concrete if the reinforcing steel size is known. This instrument was chosen because it offers a large inspection depth up to 4.5 in. for relocating reinforcing steel and can be used for sizing reinforcing steel with a resolution of one reinforcing steel size (i.e., 1/8 in.) without prior knowledge of the reinforcing steel depth. The instrument can be operated either in the short mode for detecting reinforcing steel up to 2.5 in. in depth, or in the deep mode for measurement depths ranging from 2.5 to 4.5 in.

Two types of readouts are displayed when the scope is used for locating reinforcing steel: the signal level in an arbitrary unit and the distance between the reinforcing steel and the sensor probe. The outer dimensions of the probe are shown in the inset of Figure 23, but the exact dimensions of the EC coil inside the casing are not known. The probe was mounted onto a XYZ

scanner stage (Figure 23a) that was under computer control for performing line or raster scans over the bare reinforcing steel or concrete test specimens.
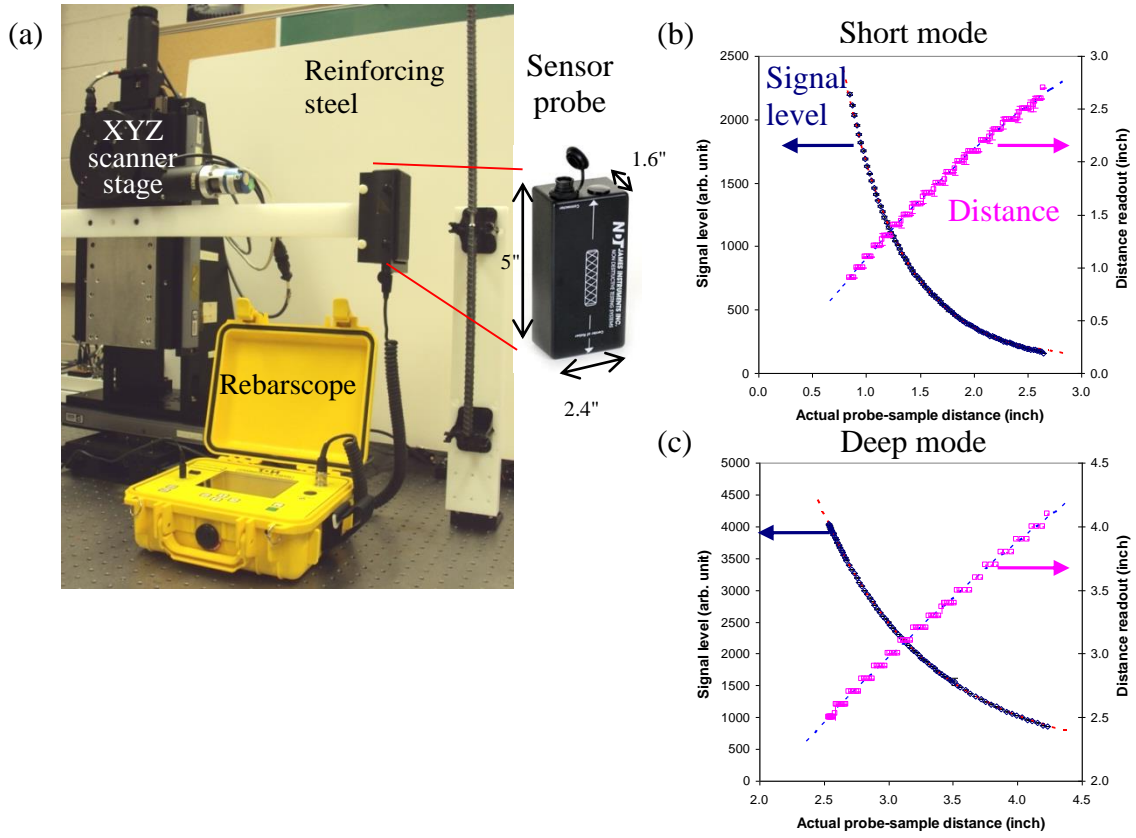
Figure 23. (a) Setup for EC scans on bare #4 reinforcing steel specimens and (b) and (c) signal level and distance readings versus actual probe distance

Figure 23a shows the experimental setup for EC scans on bare #4 reinforcing steel specimens using the Rebarscope III. The outer dimensions of the sensor probe are shown in the inset to the right of Figure 23a. The signal level and distance readings are plotted versus the actual probe distance from an intact #4 reinforcing steel when operating the instrument in the short detection mode in Figure 23b and in the deep detection mode Figure 23c. The dotted lines in the charts represent fits to the signal level and distance readout using equations (1) and (2), below, respectively.

Measurements were first carried out on a #4 reinforcing bar to calibrate the signal level and the distance readout against the actual distance between the reinforcing steel and the sensor probe. The signal level, Vs, was found to decrease as the probe-reinforcing steel distance, d, increases. The result can be described empirically by equation (1):

$$V_S = V_0 + A_0 \exp\left(-\frac{d}{d_0}\right)$$

(1)

where the values of the fitting parameters V_0, A_0, and d_0 are shown in Table 4 for the short and deep detection modes.

Table 4. Values of fitting parameters describing the dependence of signal level V_S and distance readouts, d_m, on the actual probe-reinforcing steel distance, d

	Signal Level V_S (equation (1))			Distance Readout d_m (equation (2))		
	V_0	A_0	d_0	a_0	a_1	a_2
Short mode	107.6 ± 3.9	9823.2 ± 104.6	0.543 ± 0.004	0.222 ± 0.031	1.431 ± 0.037	**-0.133 ± 0.011**
Deep mode	**388.7 ± 5.9**	**74201.3 ± 649.5**	**0.841 ± 0.003**	**0.622 ± 0.139**	**1.410 ± 0.086**	**0.072 ± 0.013**

The dependence of the distance readout, d_m, on the actual distance d can be described by equation (2):

$$d_m = a_0 + a_1 d + a_2 d^2$$

(2)

The values of the fitting parameters a_0, a_1 and a_2 are given in Table 4. Note that the resolution of the distance readings, d_m, is 0.1 in. In contrast, the signal level readouts in both the short and deep modes have more significant figures, therefore offering a better resolution for distance measurements based on the empirical calibrations (Figures 23b and 23c).

4.2.2   Magnetic Flux Leakage Measurement System

An MFL sensor probe was designed and fabricated using GMR sensors specifically for inspecting reinforcing steel near the cold joints of concrete structures as shown in Figure 24. The concept of the probe design is illustrated in Figure 25.
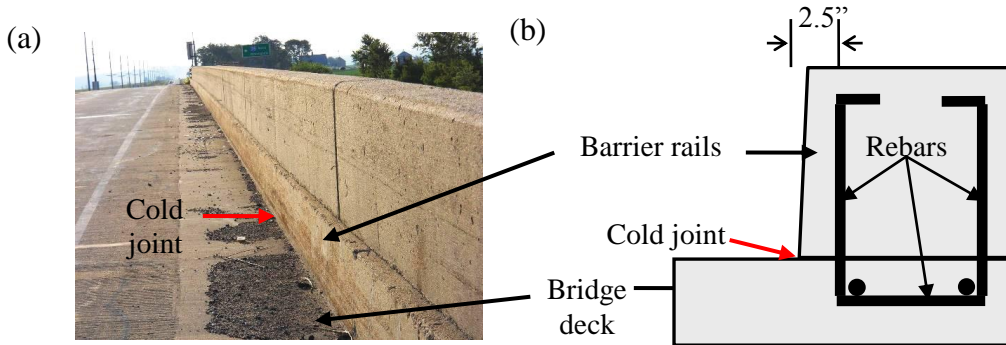
Figure 24. Bridge barrier rail showing the presence of a cold joint between the deck and the rail and locations of reinforcing steel that anchor the barrier rail to the bridge deck
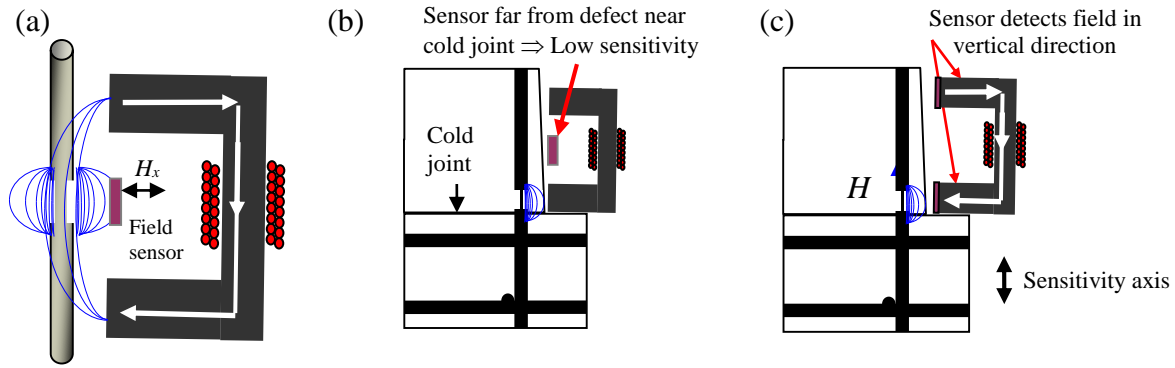
Figure 25. Conventional and alternative MFL probe design

Figure 25a depicts a conventional MFL probe design that utilizes a c-core electromagnet to magnetize the reinforcing bar and a magnetic field sensor to detect the leakage field component H_x perpendicular to the long-axis of the bar. Figure 25b depicts application of the conventional probe design to inspect reinforcing steel near the cold joint between the bridge deck and barrier rail. In this case, the field sensor is located far from the cold joint where corrosion damage most often occurs. Figure 25c depicts an alternative probe design developed in this research that utilizes field sensors mounted on the pole pieces of the electromagnet to sense the leakage field from the defect.

Consider a reinforcing steel that is magnetized under a direct current (DC) or alternating current (AC) field generated by a c-core electromagnet (Figure 25a). Any damage in the reinforcing steel will give rise to localized leakage field. Typical MFL probe designs use a magnetic field sensor, such as a Hall effect sensor, to detect the leakage field component, Hx, perpendicular to the reinforcing steel axis (Figure 25a).

The sensor is often located halfway between the pole-pieces of the electromagnet where the horizontal component of the magnetizing field from the electromagnet is minimal. This sensor placement helps maximize the signal difference (and hence the sensitivity) between damaged and intact reinforcing steel. One issue with such a design for inspecting the cold joints of bridge structures is that even if the probe is placed on the bridge deck (Figure 25b), the field sensor will be located well above the cold joint, thereby resulting in a low sensitivity to the leakage field. It is conceivable that reducing the dimensions of the electromagnet will help bring the field sensor closer to the cold joint, but it will also limit the inspection depth, rendering the design unsuitable for the targeted application.

The limitations of the aforementioned conventional design were circumvented by devising an alternative detection scheme as depicted in Figure 25c. Magnetic field sensors are placed directly on the pole pieces of the electromagnet. This placement allows the use of electromagnets large enough to magnetize reinforcing steel at the required depth and, at the same time, the field sensors can stay close to the cold joint where reinforcing steel corrosion most often takes place.

36

Given the horizontal component of the magnetizing field at the pole piece can easily dominate the leakage field from defects and overwhelms the field sensor, in our design the field sensors are aligned so that they are only sensitive to field component, Hy, in the vertical direction, which is minimal in the absence of any defect. This design aims to utilize the vertical component of the leakage field to maximize the sensitivity of the MFL signal to any defect or damage of the reinforcing steel.

The experimental setup for performing MFL scans on bare reinforcing steel and concrete test specimens in the laboratory is shown in Figure 26a. Figure 26b shows a close-up of the MFL sensor probe that consists of an electromagnet to apply the magnetizing field and two GMR sensors to detect the vertical component of leakage field at the pole-piece of the electromagnet.
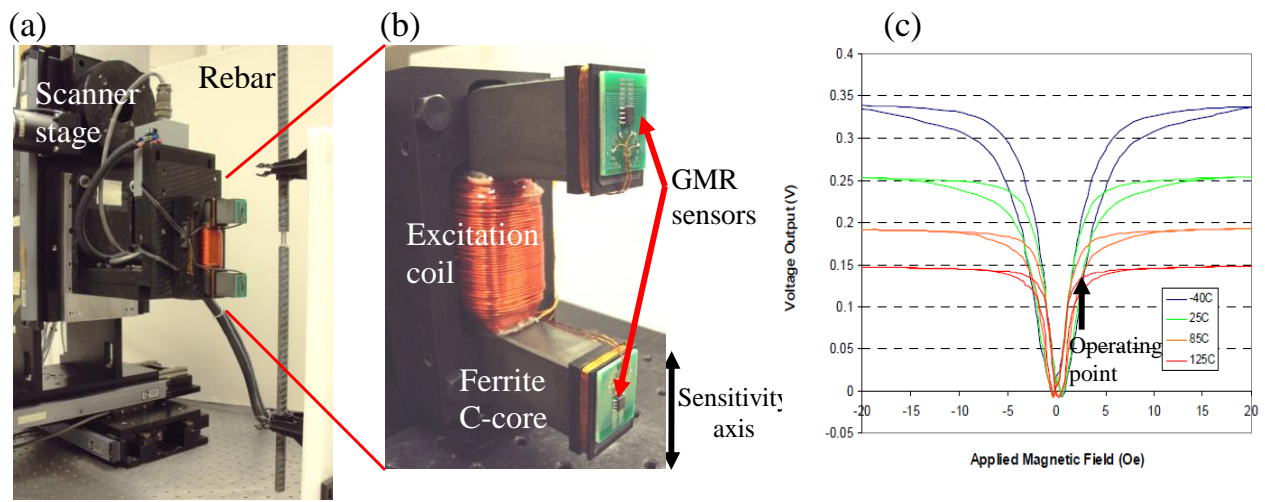
Figure 26. (a) Experimental setup for performing MFL scans, (b) close-up of the MFL sensor probe and (c) nominal output of the GMR sensors versus magnetic field (Bligh et al. 1994)

The sensor probe consists of a c-core electromagnet made of ferrite, which was driven using a bipolar power amplifier (Model: 20-20, Kepco, Inc.) to apply a low-frequency (20 Hz) sinusoidal magnetizing field to reinforcing steel samples. Two commercial GMR sensors (Model: AAH002, NVE, Corp) were mounted onto the pole pieces to detect the magnetic field in the vertical direction as shown in Figure 26b.

GMR sensors were used as they offer a substantially higher sensitivity than Hall effect sensors. Nevertheless, the GMR sensors have non-linear output characteristics (Figure 26c), rendering them more difficult to use than Hall effect sensors. In particular, GMR sensors are axial sensor, meaning that they give the same voltage output for both +ve or −ve fields. The sensor outputs also show hysteresis and become saturated at high fields, thereby having a limited detectable field range that often varies inversely with the sensor sensitivity.

In our measurements, a small DC current was applied to the electromagnet to produce a DC-biasing field. This aimed to set the operating point of the sensor close to the mid-point of the

detectable field range (Figure 26c). For the laboratory studies, the MFL sensor probe was mounted onto a three-axis scanner "stage" (Figure 26a) for performing line scans or raster scans over standalone reinforcing steel and concrete test specimens.

The outputs of the GMR sensors, which are typically in the order of 0.1 mV for reinforcing steel at a distance of 2.5 in., were detected using lock-in amplifiers (model: 5210, EG&G, Princeton Applied Research) to obtain both the amplitude and phase (relative to the excitation signal) of the MFL signals. The signal amplitude was used in constructing line-scan profile or C-scan images of MFL signals described in the following result section.

4.2.3   Stage 1: Laboratory Tests on Bare Reinforcing Steel with Defects

In Stage 1, the feasibility of using the Rebarscope III to detect material loss in reinforcing steel was studied by performing line scans (Figure 23a) over bare, standalone #4 reinforcing steel samples at a fixed distance of 2.56 in. (65.0 mm). This distance was chosen to allow the instrument to be operated in the deep detection mode that offers a higher sensitivity than the short detection mode (Figures 23b and 23c). The line scans performed are 10 in. long, centered on the mid-point of the reinforcing steel, where the artificial defects of samples R-2 and R-3 are located as shown in Figure 22a.

Figure 27 shows the signal level versus the vertical position of the probe. For reinforcing steel sample R-1 without any defect, the signal level remains relatively constant (Figure 27a). The signal decreases slightly near the ends of the scan as the probe approaches the ends of the reinforcing steel. For sample R-2 with a defect of 25 percent material loss, the signal detected near the defect is slightly weaker than that of R-1, and the signal level starts to drop off quickly when the probe center is about 2 in. off the defect. For sample R-3 with 50 percent material loss, the signal detected near the defect is even weaker.
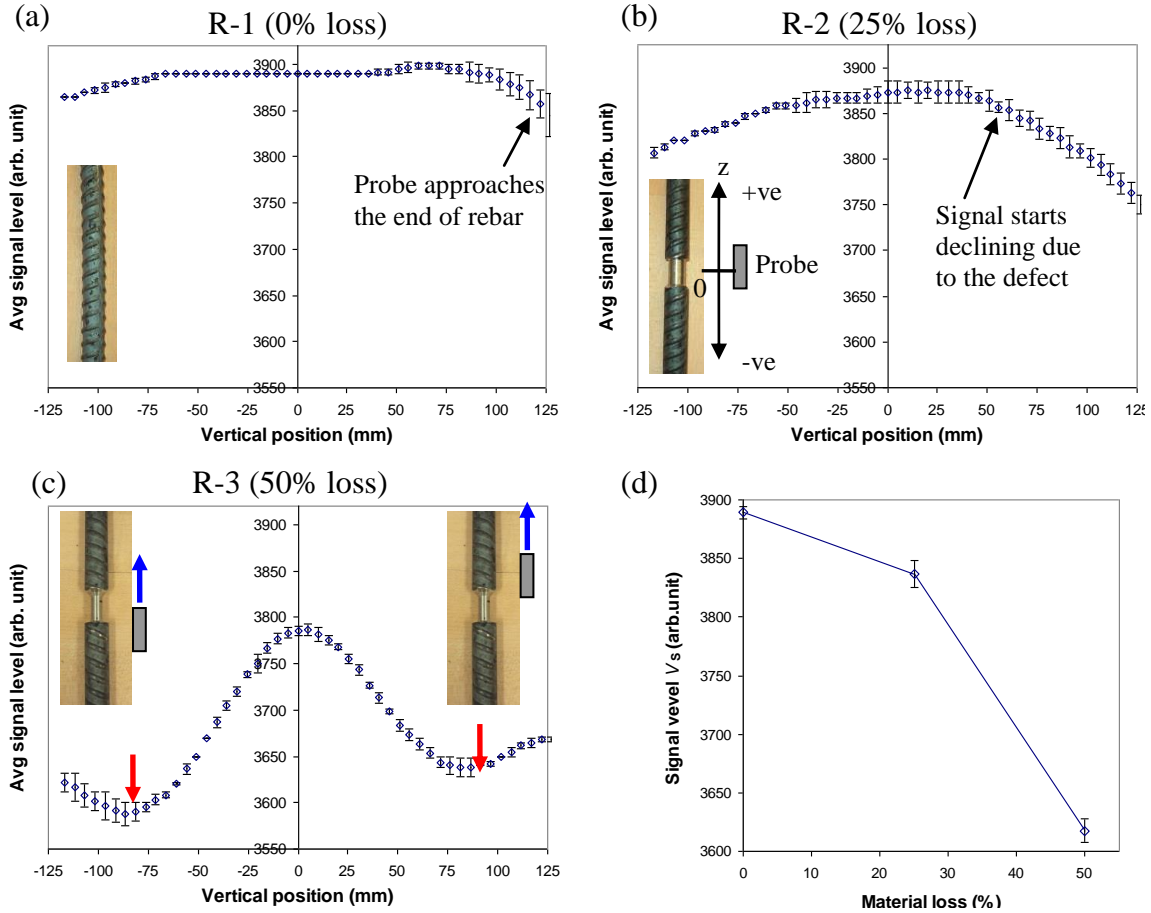
Figure 27. (a-c) EC signal levels (in arbitrary unit) versus vertical position of the sensor probe and (d) dependence of the averaged EC signal level detected at 3 in. from the defect on the amount of material loss

Figure 27a through 27c show the EC signal level (in arbitrary unit) versus vertical position of the sensor probe for reinforcing steel samples R-1 (intact), R-2 with 25 percent material loss, and R-3 with 50 percent material loss, respectively. The insets of Figure 27c show vertical positions of the sensor probe relative to the defect when the detected signal shows a minimum. Figure 27d shows the dependence of the averaged EC signal level detected at 3 in. from the defect on the amount of material loss. The error bars represent one standard deviation of three repeated scans over each sample.

Of special note is that the signal level reaches a minimum when the probe center is about 3 in. off to either side of the defect. This can be interpreted by considering typical EC signal patterns when using an oversized coil to detect a defect that is much smaller than the coil diameter. When a coil is placed on a conductor, the induced EC in the conductor is strongest underneath the coil winding rather than under the coil center. Therefore, when scanning an oversized coil over a relatively small defect, the signal change (changes in coil impedance) is largest when the defect is directly underneath the coil winding.

The situation is similar to the present EC tests on the reinforcing steel samples because, in this case, the coil length, which could be as much as 5 in. (127 mm), is substantially larger than the defect length of about 0.55 in. (Table 2). Therefore, when the probe center is about 3 in. (76 mm) below the defect, the top edge of the probe and hence the coil windings are close to the defect (illustrated by the inset of Figure 25c), resulting in the largest reduction of signal. Similarly, the bottom edge of the probe is close to the defect when the probe center is 3 in. above the defect.

The present results indicate the feasibility of using the reinforcing steel locator to detect material loss in reinforcing steel. Once the defect is located, the signal level detected at 3 in. (76 mm) away from the defect, where the coil winding is in close proximity to the defect, can be used to quantify the amount of material loss (Figure 27d).

4.2.4   MFL Study of Bare Reinforcing Steel Samples

4.2.4.1   Signal Dependence on Reinforcing Steel Distance

The measurement range of the MFL system developed in this study was evaluated first by performing line scans across an intact #4 reinforcing bar with the sensor probe at various perpendicular distances, ranging from 2.5 in. (63.5 mm), which is the minimum inspection requirement, to 4.5 in. (114.3 mm), from the reinforcing steel. As shown in Figure 28, the detected signal is the strongest when the probe is in front of the reinforcing steel.
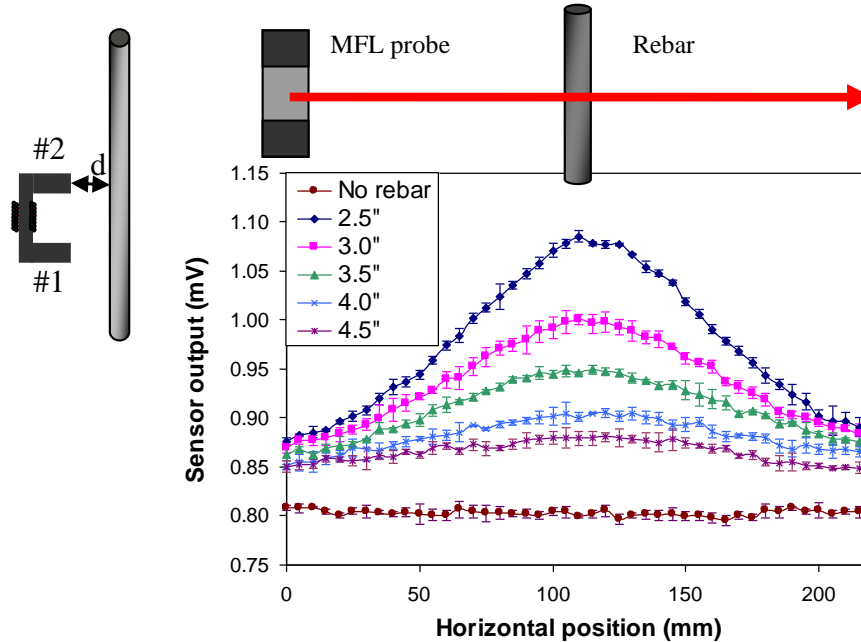
Figure 28. GMR sensor output versus the horizontal position of the MFL sensor probe at various perpendicular distances from the reinforcing steel

The maximum signal level decreases as the distance between the probe and reinforcing steel increases. The reinforcing steel is located at the center of the scans, where the sensor output is

the strongest. The results indicate that standalone reinforcing steel up to 3.5 in. away can be detected and located readily from the position of the signal peak.

4.2.4.2 MFL C-Scan Images of Bare Reinforcing Steel Samples

Raster MFL scans were carried out over the bare, standalone #4 reinforcing steel samples at a distance of 2.5 in. (63.5mm) as shown in Figure 29a. (Perpendicular distance d between the probe and reinforcing steel is 2.5 in.)
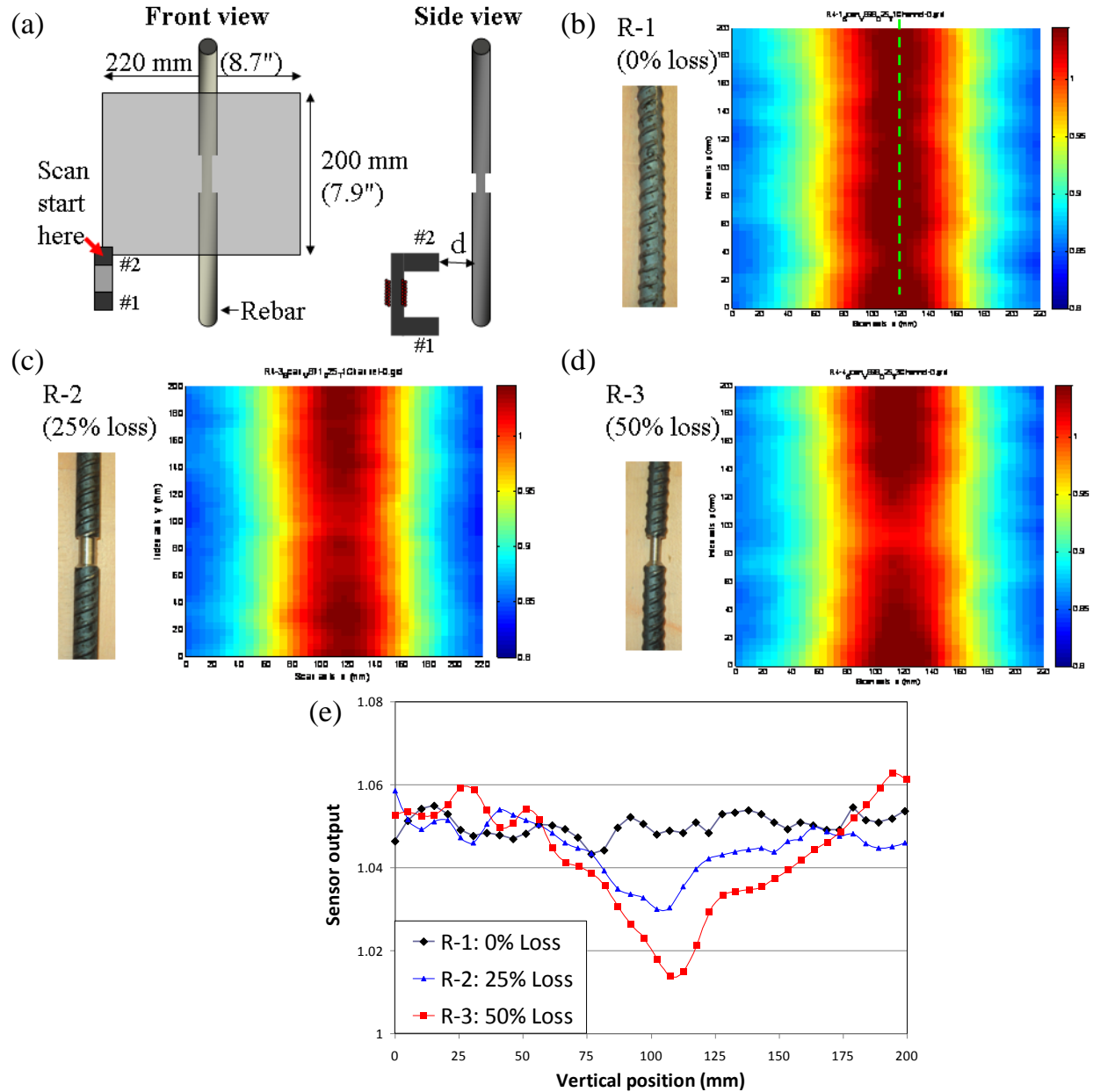
Figure 29. (a) Size and coverage of raster scans over bare #4 reinforcing steel, (b-d) C-scan images, and (e) profile of sensor outputs

Figures 29b through 29d are C-scan images measured using the GMR sensor #2 (mounted on the upper pole piece of the electromagnet as shown in Figure 26b) and plotted in the same color scale for samples R-1, R-2, and R-3, respectively. The scan size is 8.7 in. (220 mm) by 7.9 in. (200 mm). Reinforcing steel samples are detected readily in the C-scan images.

The sample R-1 image shows a relatively uniform, continuous pattern of the reinforcing steel in the middle of the scan. For sample R-2 with 25 percent material loss, the GMR sensor output decreases significantly at the center of the scan when sensor #2 scanned in front of the defect. A stronger defect indication was observed for sample R-3 with a 50 percent material loss.

Figure 29e shows a profile of sensor outputs (from along vertical dotted line shown on the scan image in Figure 29b) for the three different reinforcing steel samples. It is evident from this graph of the C-scan data that signal reduction detected near the defect is larger for a larger amount of material loss.

The results indicate the capability of the MFL method to detect defects in reinforcing steel and to quantify the extent of material loss based on empirical calibrations, provided that the distance between the reinforcing steel and sensor probe is known (e.g., measured independently using a reinforcing steel locator).

4.2.4.3   Differential Detection of Reinforcing Steel Defect

The sensitivity of the MFL technique to reinforcing steel damage can be improved by means of differential detection of the leakage fields from defects. Specifically, the difference between the outputs of the two GMR sensors (Figure 26b) can be used instead to help suppress the background signal coming from the undamaged portions of the reinforcing steel and thereby enhance defect indication. The C-scan images measured by the GMR sensors, as well as their differences, are shown in Figure 30 for the bare reinforcing steel samples.

Images in the top and second rows were measured by the GMR sensors #2 and #1, respectively. Images in the bottom row correspond to the difference in signals. All images are plotted in the same color scale for comparison.

For sample R-3, the output of sensor #2 decreases significantly when the sensor is near the defect (the top image of Figure 30a). At that instance, sensor #1 is in front of the intact region of the reinforcing steel and therefore the signal is strong and uniform (the middle image of Figure 30a). By subtracting the output of sensor #1 from that of sensor #2, a C-scan image of the difference in signals can be obtained (bottom image of Figure 30a), which shows a uniform, low-level background because the reinforcing steel signals are mostly canceled out, except near the defect at the image center. Similarly, a clear defect indication was observed in the difference in signal for sample R-2 with 25 percent material loss (Figure 30b). In contrast, the difference in signal of the intact reinforcing steel R-1 only shows a low-level background without any defect indication (Figure 30c).
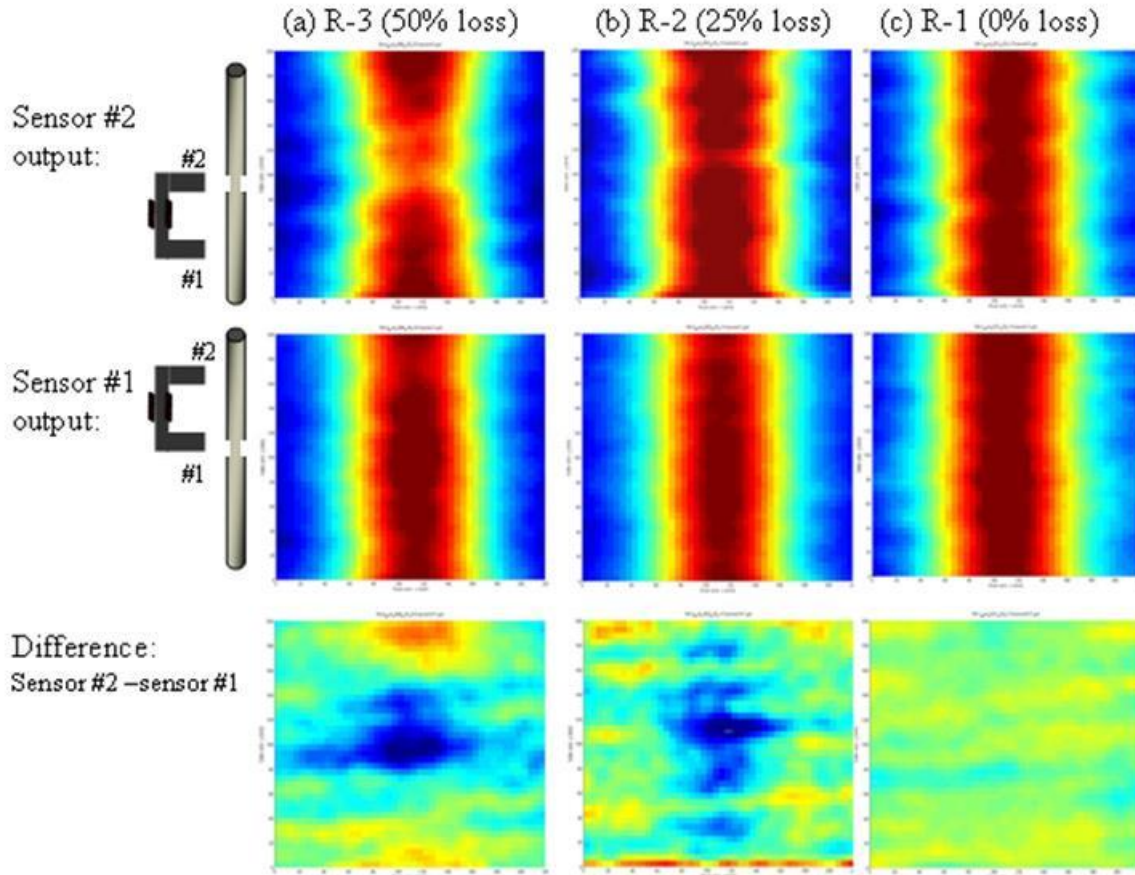
Figure 30. C-scan MFL images for bare reinforcing steel specimens

4.2.5   Stage 2: Laboratory Tests on Concrete Test Specimens

4.2.5.1   EC Scans on Concrete Test Specimens with # 6 Reinforcing Steel

EC line scans were performed on the two concrete test specimens M4 and M5 (Table 3) containing #6 reinforcing steel using the Rebarscope III. Figure 31a shows the experimental setup. Two types of line scans were carried out: horizontal scan from left to right with the EC probe maintaining a height of 0.12 in. (3 mm) above the cold joint (Figure 31b) and vertical scan upward in front of the vertical reinforcing steel (Figure 31c).

The results of the horizontal line scans are shown in Figure 32. For both concrete test specimens, the detected signal levels reach a maximum when the probe is in front of the vertical reinforcing steel. The signal level was higher for the 50 percent loss specimen. This is in contrast to the EC scan results obtained from the bare, standalone #4 reinforcing steel, which show a lower signal level near the defect (Figure 27).

43
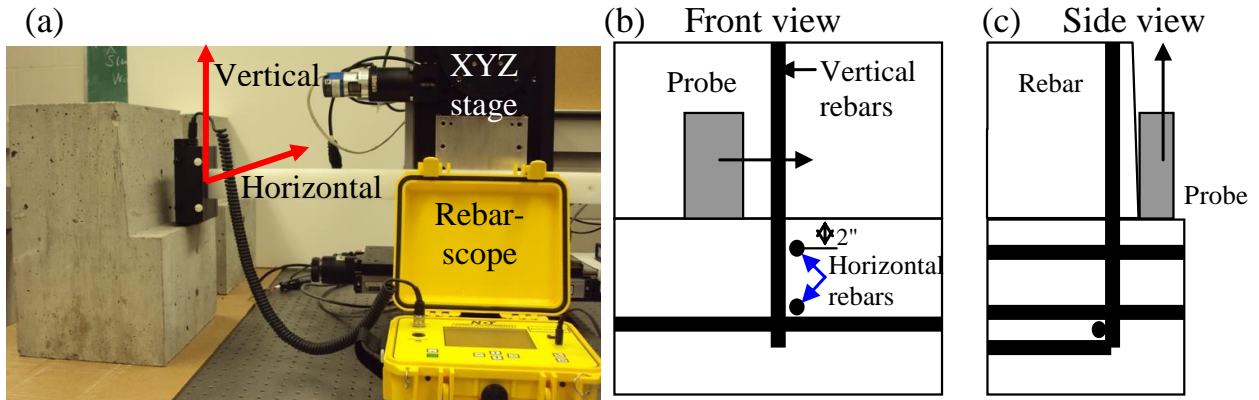
Figure 31. Experimental setup for performing EC line scans on the concrete test specimens
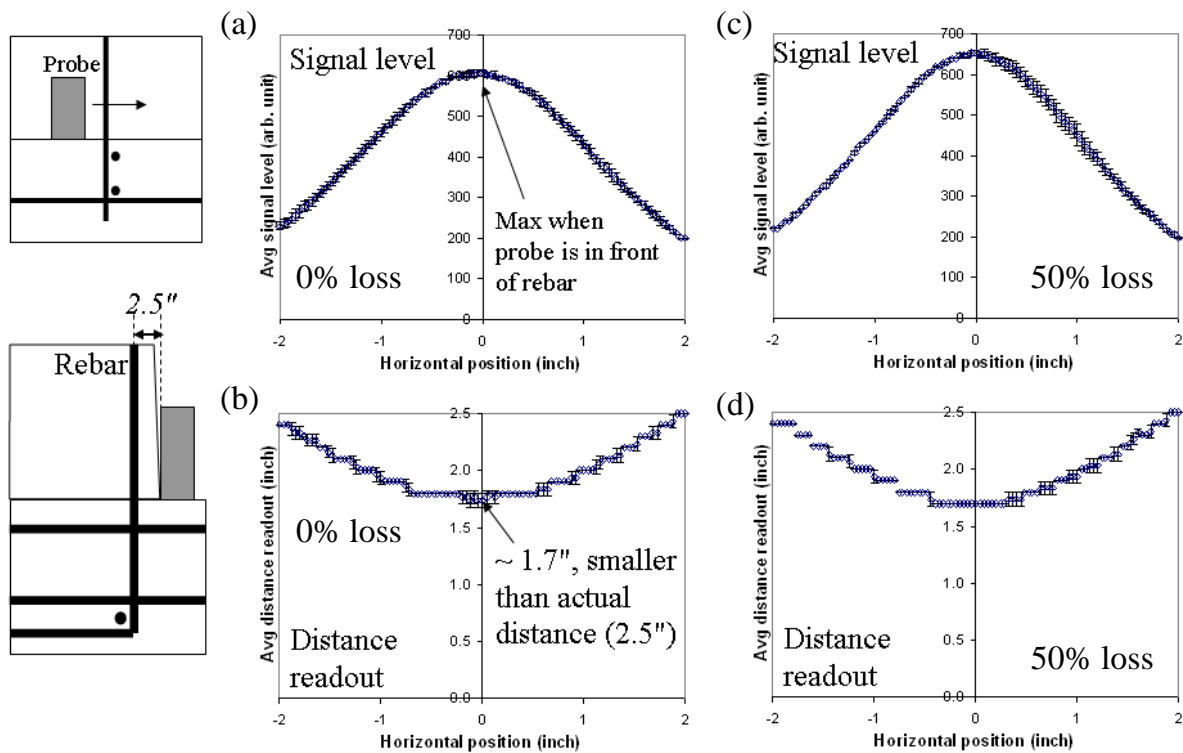
Figure 32. (a and c) EC signal levels and (b and d) distance reading obtained from horizontal line scans over the concrete test specimens

Figure 32a shows the EC signal level and 32b shows the distance reading obtained from horizontal line scans over the concrete test specimen M4 that consists of intact #6 reinforcing steel with 0 percent loss. Likewise, Figure 32c and 32d are for test specimen M5 with a defect representing 50 percent material loss. The schematic diagrams on the left show the scan (upper) and the location of the sensor probe relative to the vertical reinforcing steel inside the concrete block.

Of special note is that the signals from both test specimens are stronger overall than expected for a standalone #6 reinforcing bar at the same distance from the sensor probe. This is indicated by the distance reading (Figures 32b and 32d), which was found to be about 1.7 in. or less at the center of the scan for both specimens, significantly smaller than the actual distance of 2.5 in. between the probe and the reinforcing steel. The discrepancy is attributed to the fact that the sensor probe also picks up signals from the upper horizontal reinforcing steel (indicated in Figure 31b), which is merely 2 in. below the sensor probe when it is scanned in front of the vertical reinforcing steel. As a result, the detected signal becomes stronger than expected, leading to an under-estimation of the probe-reinforcing steel distance based on the built-in calibrations of the instrument for standalone reinforcing steel.

Interference of the horizontal reinforcing steel was also observed in the vertical EC line scans (Figure 33). For example, the signal level detected from specimen M4 (embedded intact #6 reinforcing steel with 0 percent material loss) shown in Figure 33a starts at a high value when the probe is on the cold joint. This result is attributed to the fact that the instrument picks up signals not only from the vertical anchoring reinforcing steel but also from the upper horizontal reinforcing steel.
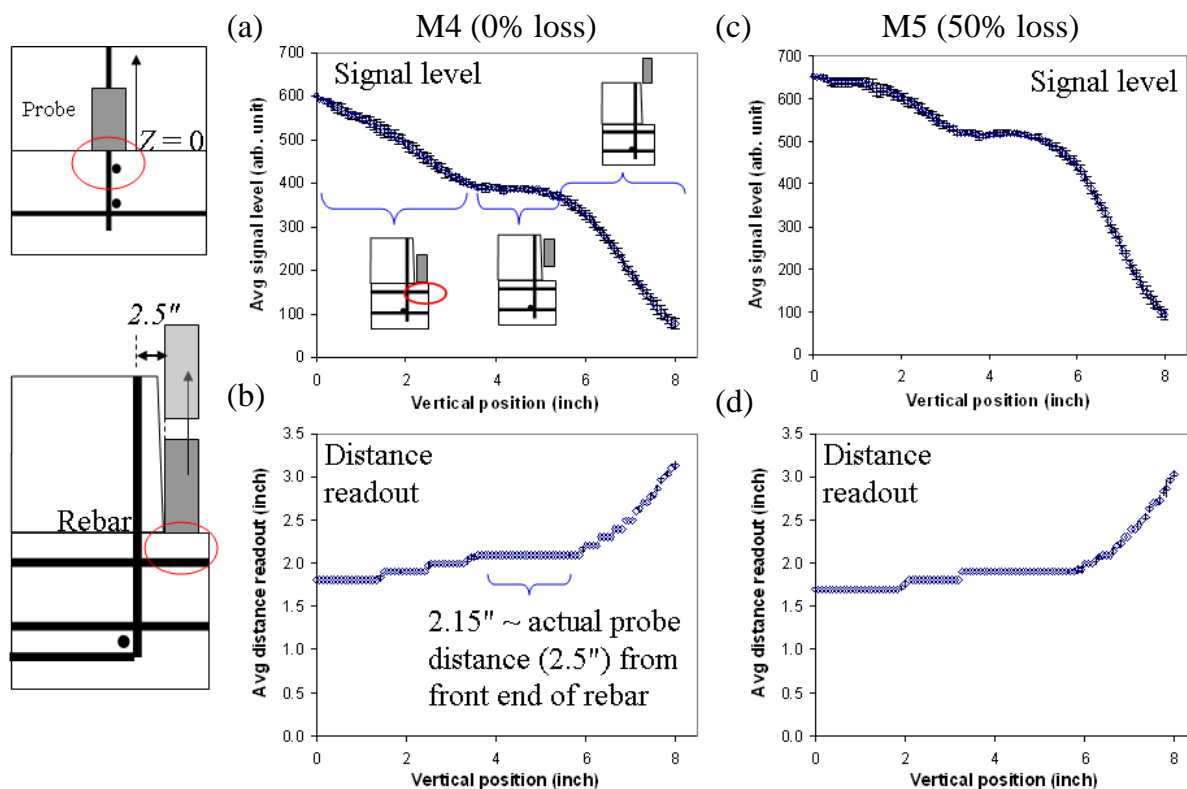
Figure 33. (a and c) EC signal levels and (b and d) distance reading obtained from vertical line scans over the test specimens

When the probe is elevated, the signal gradually decreases and eventually levels off when the probe is between 3.5 and 5 in. above the cold joint. The signal level of the plateau corresponds to

a distance reading of 2.15 in. (Figure 33b), which is closer to the actual distance of 2.5 in. As the probe is further elevated and approaches the upper end of the reinforcing steel, the signal level decreases significantly due to the end effect. The signal detected from specimen M5 (reinforcing steel with 50 percent material loss) shown in Figure 33c is stronger in general than that from specimen M4 (with 0 percent loss) shown in Figures 33a, consistent with the horizontal line scan results shown in Figure 30.

4.2.5.2   MFL Scans on Concrete Test Specimens

The feasibility of detecting reinforcing steel damage at the cold joint by MFL is evaluated by performing raster scans on all the test specimens (Figure 34).
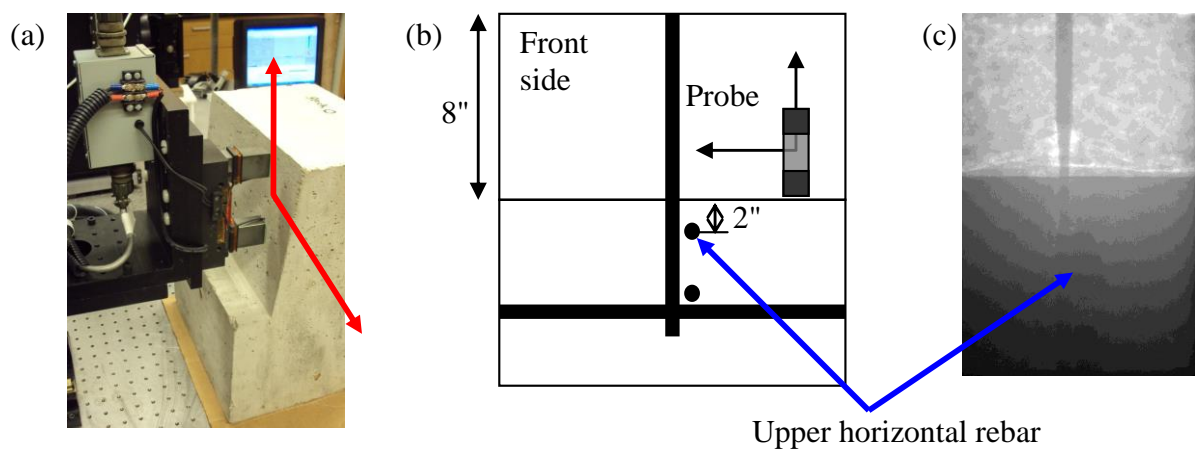
Figure 34. Experimental setup for raster MFL scans and x-ray image of test specimens

Figure 34c shows an x-ray image of test specimen M3 (#4 reinforcing steel machined to produce 50 percent material loss). (The upper horizontal reinforcing steel running from the front to the back wall of the lower concrete block is highlighted.) The scan size is 8.7 in. (220 mm) by 7.9 in. (150 mm), with the MFL probe starting at a height of 0.12 in. (3 mm) above the cold joint. The scan plane is fixed at a perpendicular distance of 2.5 in. (63.5 mm) from the vertical reinforcing steel inside the concrete.

Figure 35 shows the C-scan images for the test specimens M1, M2, and M3, which consist of vertical #4 reinforcing steel with 0, 25, and 50 percent material loss, respectively. All images are in the same color scale.

For test specimen M1, a pattern of strong signal levels highlighting the vertical reinforcing steel is observed (Figure 35a). However, unlike the C-scan images obtained from the standalone #4 reinforcing steel (Figure 27), the signal pattern broadens towards the bottom of the scan, indicating the possibility that the GMR sensor also detects signals from the upper horizontal reinforcing steel (Figure 34b).
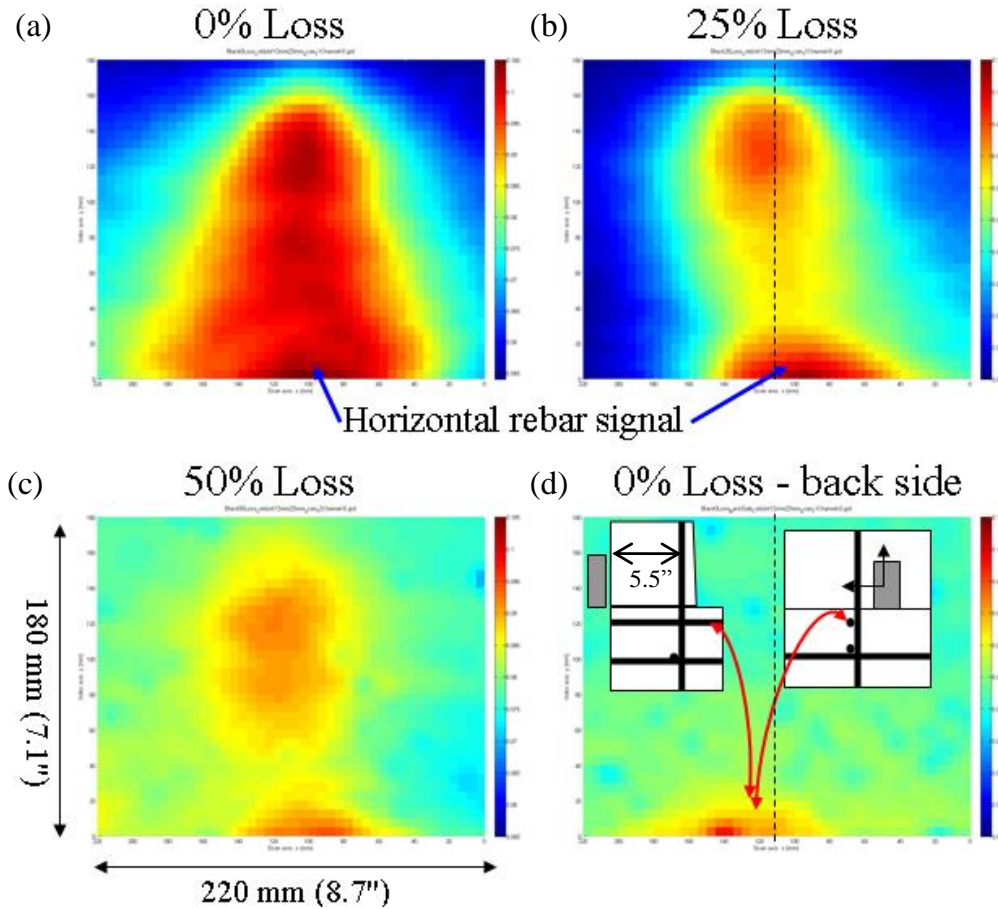
Figure 35. C-scan images of test specimens and the regions of strong signal levels caused by the horizontal reinforcing steel

The influences of the horizontal reinforcing steel are more prominent in the C-scan images of specimens M1 and M2, in which strong signals are detected consistently over the same region (Figures 34a and 34b), below which the upper horizontal reinforcing steel is located. The arrows on Figures 35a and 35b indicate the region where strong signals were observed consistently due to the upper horizontal reinforcing steel.

To confirm the observed signal patterns along the bottom edge of the scan are contributed to by the horizontal reinforcing steel, a raster scan was performed on the back side of specimen M1. As shown in Figure 35d, strong signals were once again detected near the upper horizontal reinforcing steel. The vertical reinforcing steel was not detectable in this case because it is at least 5.5 in. (140 mm) away from the sensor probe and is thereby beyond the detectable range of the MFL system.

Note that in Figure 35b and 35d, the regions of strong signal levels caused by the horizontal reinforcing steel are on the opposite sides of the centerline (denoted by the dotted line down the center of the image).

A trend was observed by comparing the C-scan images in Figure 35, in which the signal level tends to decrease with the amount of material loss. This is consistent with the MFL results obtained from the bare, standalone #4 reinforcing steel (Figures 29 and 30), indicating the possibility of detecting reinforcing steel damage even in the presence of other reinforcing steel nearby in the bridge deck.

The C-scan images of the two test specimens, M4 and M5, with #6 reinforcing steel are shown in Figure 36a and 36b, respectively.
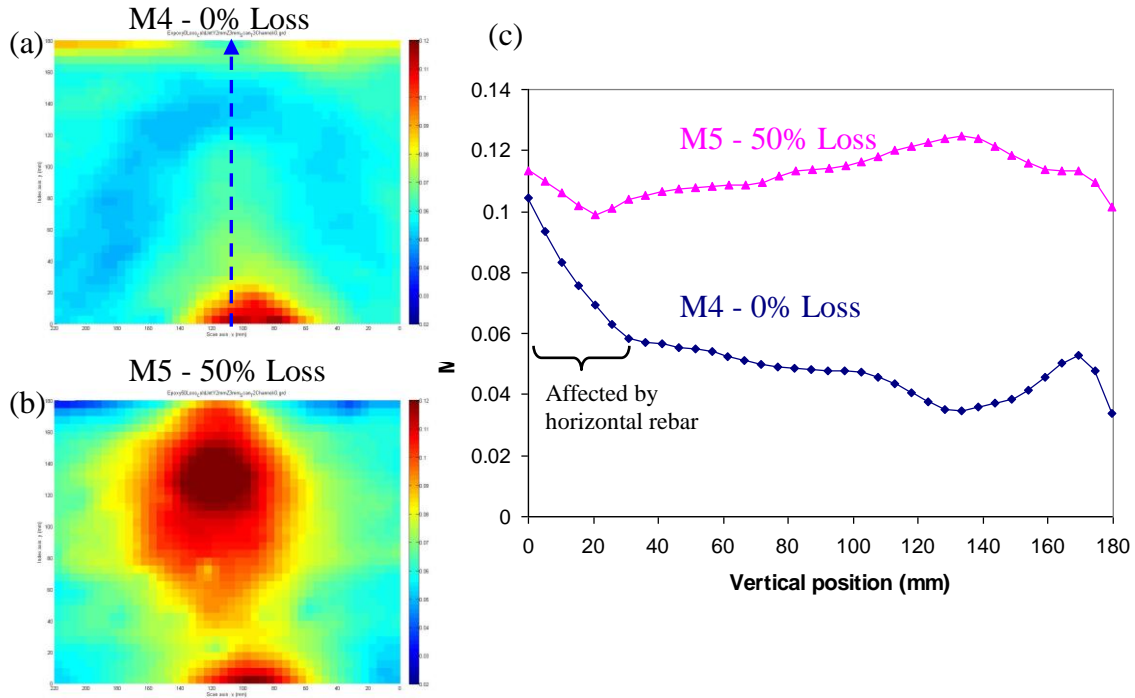
Figure 36. C-scan images of the test specimens and comparison of signal levels

For specimen M4 with 0 percent loss, the horizontal reinforcing steel once again gives a strong signal, while the vertical reinforcing steel shows a relatively weaker signal level. In comparison, the specimen M5 with 50 percent material loss shows a stronger reinforcing steel signal. For comparison, variations of the signal along the length of the vertical reinforcing steel (indicated by the dotted line in Figure 36a) are shown in Figure 36c. The signal levels extracted from the C-scan data are shown as a function of the vertical position of the sensor probe.

The detected signals at the bottom are affected by the upper horizontal reinforcing steel, but its effect gradually diminishes as indicated by the initial decline in the signal level as the probe is elevated by 1.2 in. (31 mm) above the cold joint (Figure 36c). Beyond that, the MFL signal is consistently stronger for specimen M5 with 50 percent material loss than for specimen M4 with 0 percent loss, similar to the results of the EC tests on these test specimens, which also show stronger EC signals for specimen M5 than for specimen M4 (Figures 33a and 33c).

4.2.6 Stage 3: Field Test on Iowa Highway 210 Bridge over I-35 Barrier Rails

4.2.6.1 Details of MFL Field Tests

Following the laboratory tests on bare reinforcing steel and concrete test specimens, a field test was conducted on the Highway 210 Bridge over I-35 near Slater, Iowa (see Figure 37).
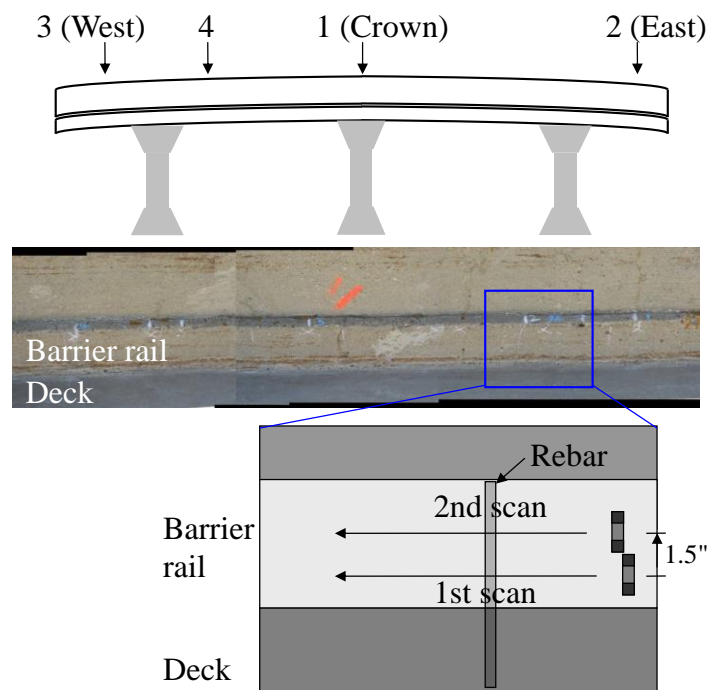
Figure 37. Iowa Highway 210 Bridge MFL field testing

The MFL measurement system was modified to improve its portability for the field test. Specifically, the outputs of the GMR sensors were amplified by a factor of 500 using instrumentation amplifier integrated circuits (ICs) (AMP02F, Analog Devices). The amplified signals were then acquired directly into a laptop computer using a multi-channel data acquisition card (USB-6251, National Instrument, Inc.). A LabView program was written for data acquisition and real-time signal analysis to obtain the amplitude and phase of the MFL signals. These modifications alleviated the use of lockin amplifiers to detect sensor outputs, thereby reducing the hardware needed for the field test.

The upper right drawing in Figure 37 depicts the locations and numbering of the bridge barrier rail sections that were inspected using the MFL method: crown, east end, west end, and section between the crown and west end of the bridge (denoted as section 4). The MFL measurements were preceded by GPR tests performed by team members on the same sections for comparison.

Due to time constraints, only three to four reinforcing bars were selected from each section for MFL measurements. Two MFL line scans were carried out on each. The bottom right drawing in Figure 37 depicts two MFL line scans over a selected reinforcing bar.

In the first pass, the probe was scanned on the deck across a selected reinforcing bar. In this case, the GMR sensor (#1) mounted on the lower pole piece was about 1.42 in. (36 mm) above the deck. This minimum scan height was chosen to minimize interference from any horizontal reinforcing steel in the bridge deck. The probe was then raised by 1.5 in. (38.1 mm) and scanned across the same reinforcing steel in the second pass. This aimed to examine if there is signal difference between the two passes, which may indicate corrosion near the cold joint between the deck and the barrier rail.

The results of MFL line scans performed on the four sections are shown in Figures 38 through 41. The reinforcing bars selected for MFL tests are show in each figure. The arrows indicate the range of line scans for each. The on-deck and off-deck MFL signals are shown in the charts.
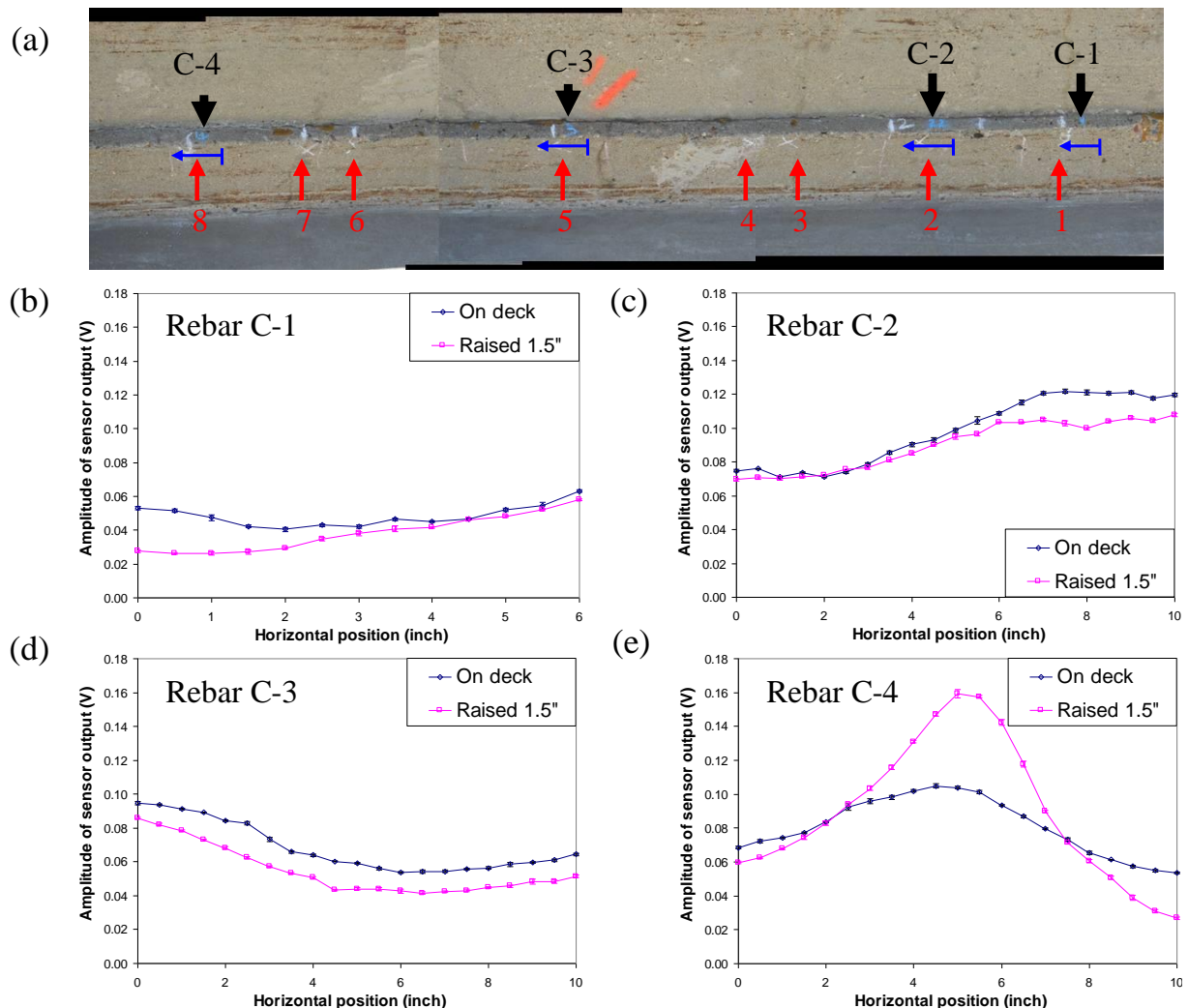
Figure 38. Crown section of the Highway 210 Bridge barrier rail

The reinforcing steel selected for MFL tests are indicated as C-1 through C-4 on the image in Figure 38a. For reinforcing steel C-1, C-2, and C-3 of the crown section, the detected signal levels in the first pass (on deck) are either comparable or stronger than those detected when the probe is raised by 1.5 in. (off deck). In contrast, for reinforcing steel C-4, the off-deck signal is stronger than the on-deck signal. The observed signal difference is interpreted as follows.

According to the Iowa DOT, the anchors in the Highway 210 Bridge barrier rails are probably either #6 (0.75 in.) or #7 (0.875 in.) reinforcing steel. Meanwhile, it was found in the Stage 2 study on the concrete test specimens M4 and M5 that the MFL signal detected from the damaged reinforcing steel tends to increase with height above the cold joint (Figure 36c). Based on these results, we can infer from the stronger off-deck signals of reinforcing steel C-4 that the reinforcing steel may suffer from material loss.

It is conceivable that the extent of damage can be estimated from the MFL signals, provided that the distance between the reinforcing steel and the probe is known, and extensive calibrations of the MFL signal as a function of both the percentage of material loss and probe distance are available. The latter is identified as one of the topics recommended for the next phase of the study.

The numbers (in red) in the bottom row on the image in Figure 38a indicate the reinforcing steel detected in the GPR scans. The arrows indicate the range of line scans for C-1 through C-4. The MFL signals measured during the first pass on the deck and the second pass after the probe was raised by 1.5 in. are shown in Figures 38b through 38e for reinforcing steel C-1 through C-4, respectively.

Again, reinforcing steel C-4 (or reinforcing steel 8 in the GPR scans) shows significantly stronger off-deck MFL signal levels and thereby possible reinforcing steel damage, consistent with the GPR results that also identify this reinforcing steel as possibly damaged.

As shown in Figure 39a, the east end of the Highway 210 Bridge barrier rail was found to have several reinforcing steel doublets (i.e., two reinforcing bars close to each other). Due to the limited scan range, most of the MFL line scans do not entirely cover both reinforcing bars of the doublet.

For example, the scan shown in Figure 39b covers only parts of reinforcing steel E-1 and E-2, as indicated by the signal maxima near both ends of the scan. Similarly, double peaks were also observed for two other doublets (reinforcing steel pairs E-3 and E-4 and E-5 and E-6). The on-deck and off-deck MFL signals are shown in Figures 39b through 39e for the selected reinforcing bar pairs: E-1 and E-2, E-3 and E-4, E-5 and E-6, and E-7 and E-8.

For the E-1 and E-2 doublet, a stronger off-deck MFL signal was observed from E-2, indicating possible damage of the reinforcing steel. Similar behavior was observed for E-4 of the E-3 and E-4 doublet and the other two doublets, E-5 and E-6 and E-7 and E-8, of the same section.
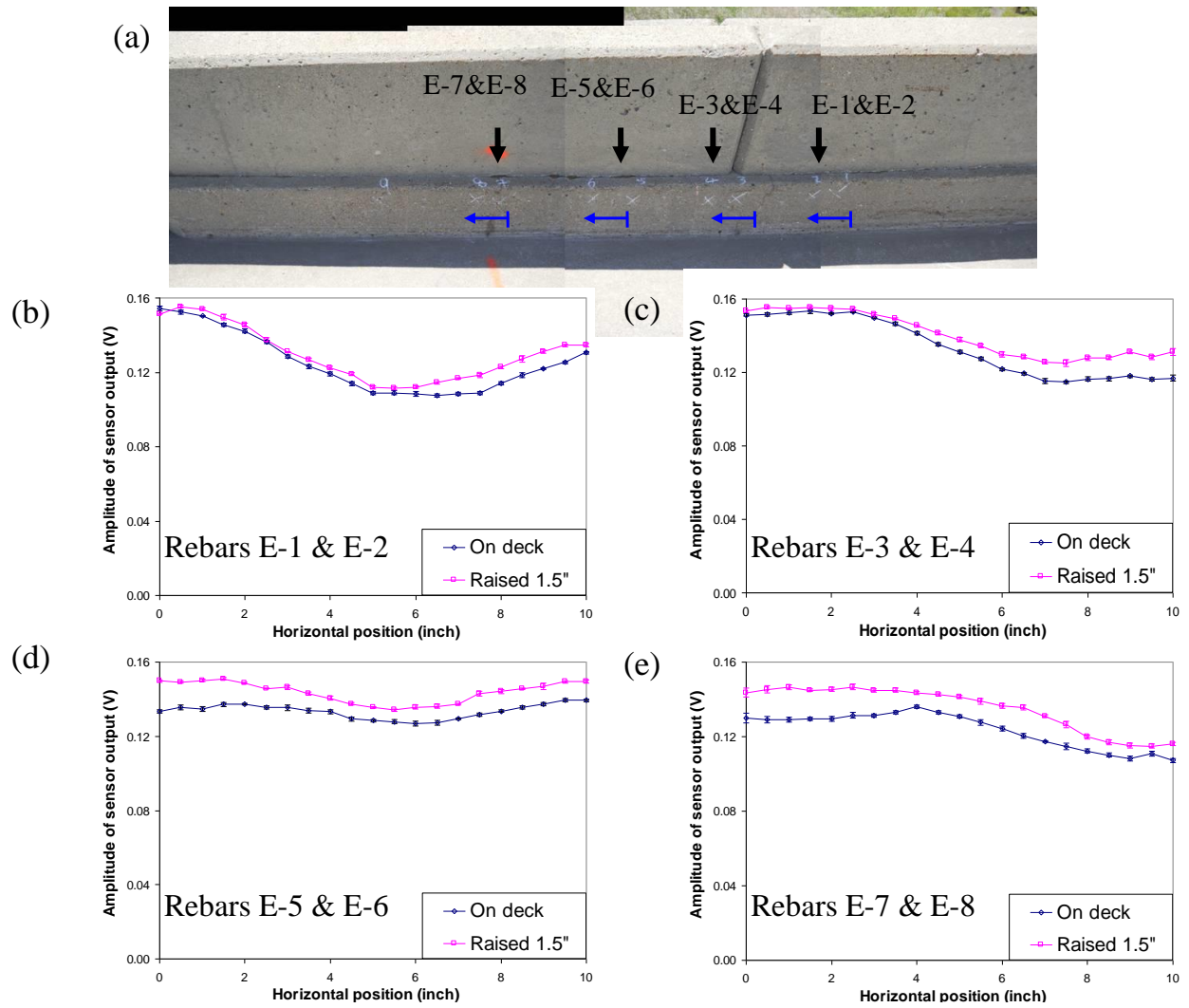
Figure 39. East-end section of barrier rail

As shown in Figures 40 and 41, all the reinforcing steel selected for MFL tests in the west end and section 4 show stronger off-deck signals and thereby possible reinforcing steel damage.

(a)

(b)

Rebar W-1

(c)

Rebar W-2

(d)

Rebar W-3
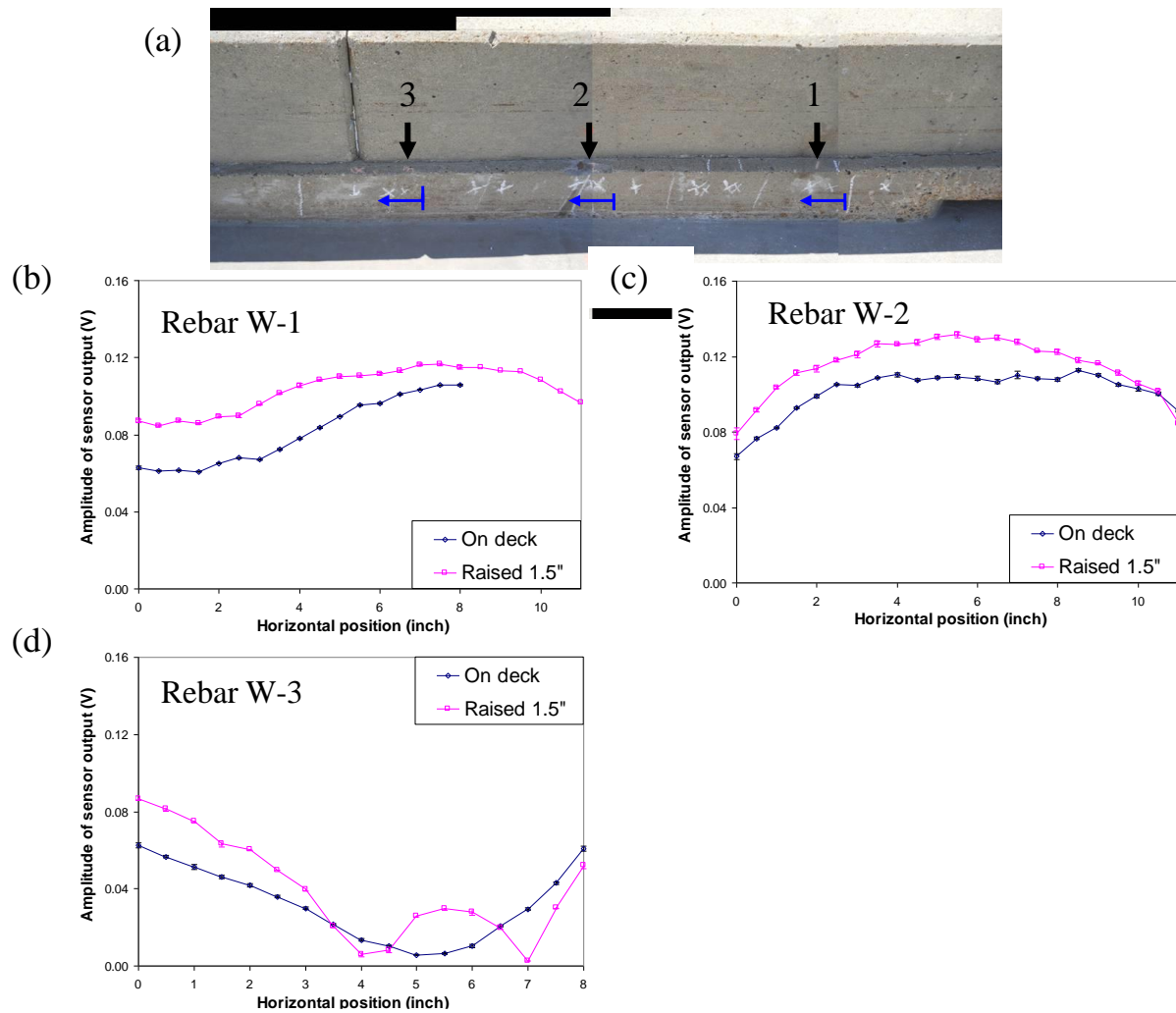
Figure 40. West-end section of barrier rail
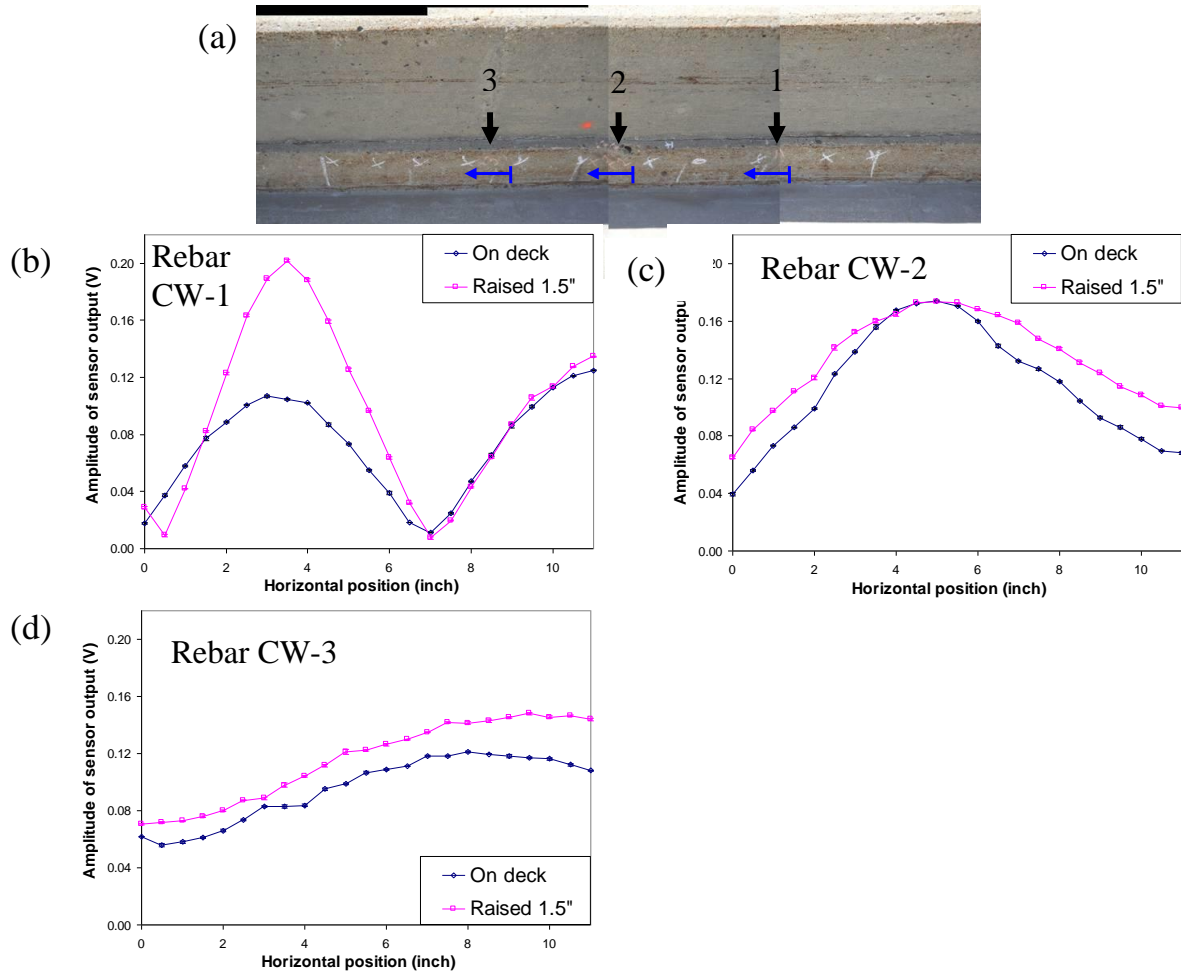
Figure 41. Section 4 of barrier rail

The field test results are summarized in Figure 42, which shows the rms values of the on-deck and off-deck MFL scan data for all of the tested reinforcing steel. To evaluate the significance of the observed difference between the on-deck and off-deck signals, the uncertainty of rms values of the line scans was determined to be 2.6 percent by repeating line scans over the same reinforcing steel. Figure 42 therefore shows that most of the tested reinforcing steel, particularly those in the west and east ends of the bridge barrier rail, show stronger off-deck signals beyond the experimental errors, suggesting the possibility that the reinforcing steel in those sections may suffer from material loss. The arrows highlight the reinforcing steel that show larger off-deck signals than on-deck signals beyond the experimental errors and thereby possible damage.

In contrast, only one of the tested reinforcing bars in the crown section gives indication of possible reinforcing steel damage. This can be interpreted by considering the fact it is more likely for water to accumulate and cause corrosion damage to reinforcing steel near the ends of the bridge than in the crown section.
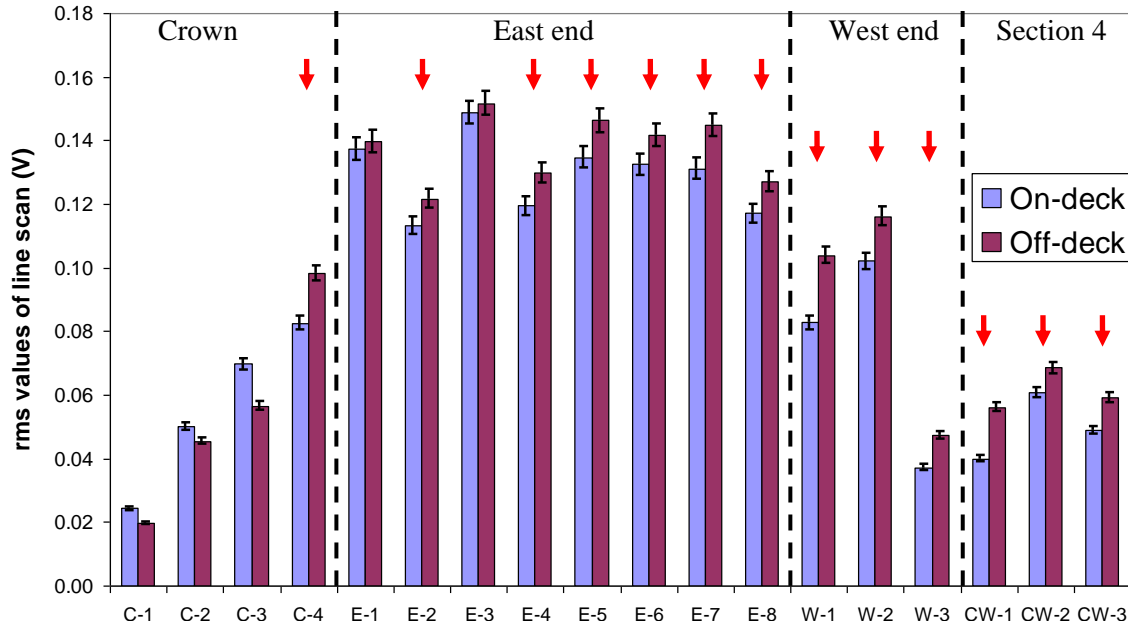
Figure 42. rms values of the on-deck and off-deck MFL line scan data from the selected reinforcing steel in the field test

4.3 Ground-Penetrating Radar

GPR is used routinely to locate and map steel reinforcing bars (reinforcing steel) in concrete structures. Detecting damage to embedded reinforcing steel is a much more difficult challenge. In this section, we report on efforts to develop a GPR approach to quantify corrosion-induced reinforcing steel thinning in concrete. The specific bridge inspection problem being addressed, detecting reinforcing steel thinning at the cold joint between the bridge deck and barrier rail, is illustrated in Figure 43.
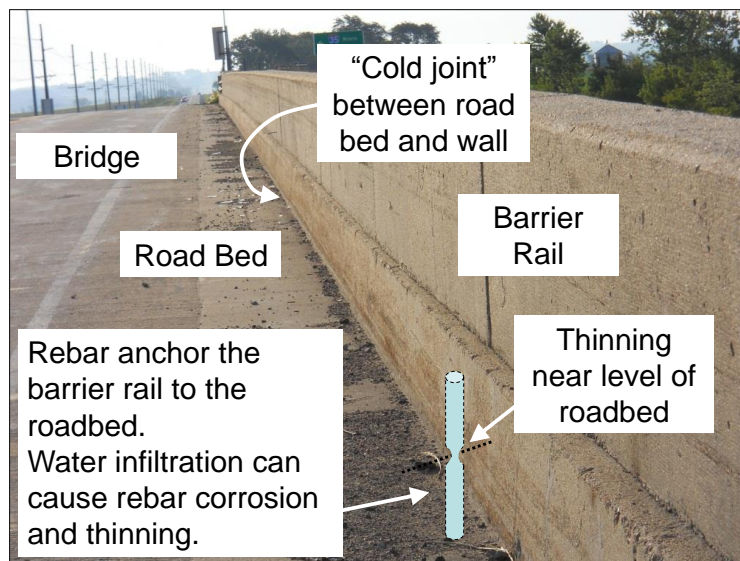
Figure 43. Bridge inspection problem

On concrete bridges, vertical reinforcing steel is used to anchor the bridge barrier rail to the deck. The concrete for the deck is placed first. Partially-embedded reinforcing steel is included in the placement along the edges of the deck to use eventually as anchors for the concrete barrier rails, which will embed the exposed vertical reinforcing steel.

Water infiltration at the cold joint between the roadbed and the bottom of the barrier rail can cause corrosion to the reinforcing steel. Over time, this can lead to reinforcing steel thinning and failure. The ability to quantify the extent of damage can provide input into decisions regarding management of bridge assets, specifically timing for repair or replacement.

For this part of the project, the two goals were to assess amplitude-based GPR as a technique for detecting reinforcing steel thinning and to use the bridge inspection problem as a vehicle for developing tools to enhance and quantify GPR inspections in general.

The reflected signal from an embedded object depends in part on the size of the object relative to the EM field that is incident upon it. Other things being equal, smaller objects will return smaller reflected signals than larger objects. Thus, the peak amplitude observed in a scanned measurement (i.e., the amplitude at the top of the hyperbola in the B-scan image) is expected to depend on the size of the embedded object. Our approach to reinforcing steel inspection is a straightforward measurement of peak-reflected amplitude. In particular, for a given reinforcing steel target:

1. Scan the antenna across the embedded reinforcing steel.
2. Observe the associated hyperbola pattern seen in the B-scan image.
3. Locate the A-scan (near the top of the hyperbola) where the reinforcing steel response is largest in amplitude. As a measure of amplitude, we use the so-called peak-to-peak voltage, i.e., the difference between the highest positive voltage and the lowest negative voltage in the A-scan signal.
4. Use this maximal peak-to-peak amplitude to quantify the reinforcing steel response.

The assumption here is that reinforcing steel containing a thinned region (i.e., presenting a smaller physical target to the incoming microwave pulse) will reflect more weakly than unthinned reinforcing steel, resulting in smaller peak-to-peak amplitude.

4.3.1   Feasibility Study Using Laboratory Reinforcing Steel in Concrete Specimens

The feasibility study used the five embedded reinforcing steel specimens, fabricated by the Bridge Engineering Center, which were designed to simulate reinforcing steel thinning at a bridge deck-barrier rail joint. Three of the specimens contained standard black 0.5 in. diameter reinforcing steel. Of these, one was intact and two had metal removed from a small region to simulate thinning at diameter reductions of 25 and 50 percent relative to undamaged reinforcing steel. The remaining two specimens contained 0.75 in. diameter epoxy-coated reinforcing steel, with one specimen intact and one having a 50 percent diameter reduction.

One difficulty in using GPR here is illustrated in Figure 44.

5 Test Specimens:
1/2"-diameter "black" rebar: 0%, 25%, 50% thinning
3/4"-diameter epoxy-coated rebar: 0%, 50% thinning
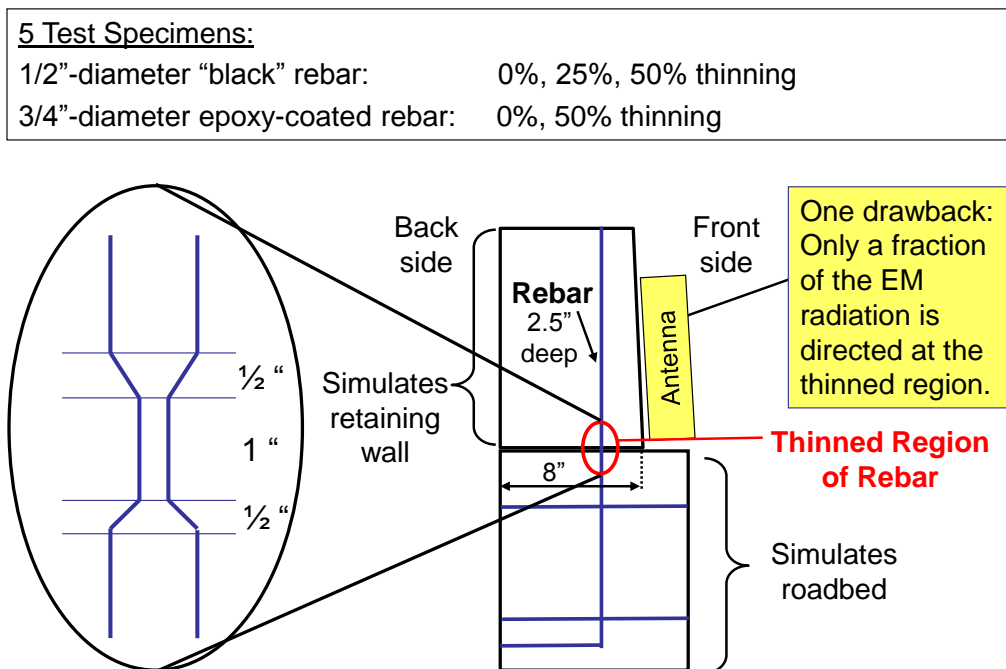
Figure 44. Relative positions of the GPR antenna and thinned reinforcing steel in laboratory test specimens

For the GPR system to operate correctly, the antenna carriage must be rolled along a surface with the carriage wheels turning properly and sending accurate position information to the computer. In our case, the antenna carriage is rolled along the vertical barrier rail surface just above the simulated bridge deck. In this orientation, the center of the antenna is aimed above the thinned region of the reinforcing steel. Thus, that thinned region is not illuminated with the strongest portion of the broadcast microwave field. Nonetheless, some of the microwave radiation does strike the thinned region and is reflected back to the antenna. Although the setup is not optimal, there is still an opportunity to search for signal amplitude differences arising from reinforcing steel thinning.

Measurements were taken to determine whether the amplitude of GPR-reflected signals could be used to distinguish between the different reinforcing steel test specimens. The five specimens were aligned as shown at the top of Figure 45 so that that the antenna carriage could be scanned across them in a continuous fashion.

Two measurement tests were conducted: one in which the antenna carriage rolled right-to-left (J004) and one in which it rolled left-to-right (J005). The B-scan image for the second test is shown in the lower portion of Figure 45. There, the reflection from the air/concrete interface appears as the horizontal band near the top of the image.
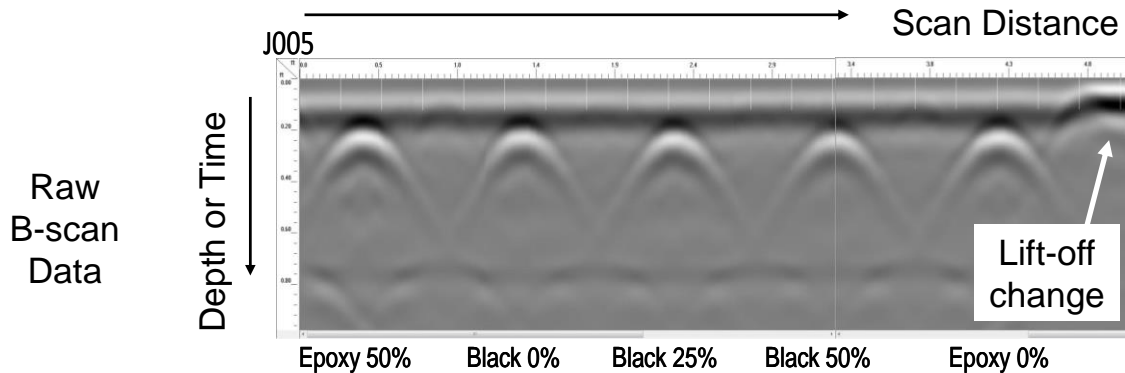
Figure 45. B-scan (bottom) obtained by scanning the GPR antenna across the five aligned test specimens (top)

Note the perturbation of this band near the far right edge; this is a consequence of the change in the liftoff between the bottom of the antenna housing and the concrete surface. Such liftoff variations can occur when a carriage wheel slips off a surface or rolls over an obstacle. To a lesser extent, liftoff can also change due to unevenness of the rolling surface, or to compression of the carriage wheels when the hand-applied pressure varies while scanning. In this particular case, the liftoff change occurred when the front wheels of the carriage rolled off the right-most concrete block, causing the antenna to tilt slightly.

The GPR data from the laboratory test blocks were examined to locate and quantify the peak responses for each reinforcing steel target. Here the front-wall interface response (air/concrete echo) partially overlaps the reinforcing steel echo. In addition, the front-wall response (and hence reinforcing steel responses) vary a bit due to minor local liftoff variations. When comparing reinforcing steel echoes from different test blocks, researchers can either ignore the overlap and liftoff effects (i.e., just report raw reinforcing steel amplitudes) or try to correct for them. Both approaches were used for this project.

For the corrected data, the steps followed are illustrated in Figure 46.

First, using the B-scan image, the maximal response from each reinforcing steel target was located, and the corresponding response-versus-time waveform (A-scan) was plotted. A reference signal was obtained by scanning the antenna across the back sides of the test blocks where the physical distance to reinforcing steel targets is larger, and reinforcing steel responses are consequently seen later in time. The early-time portion of the reference signal was then used to represent the air/concrete interface response when no reinforcing steel is present.
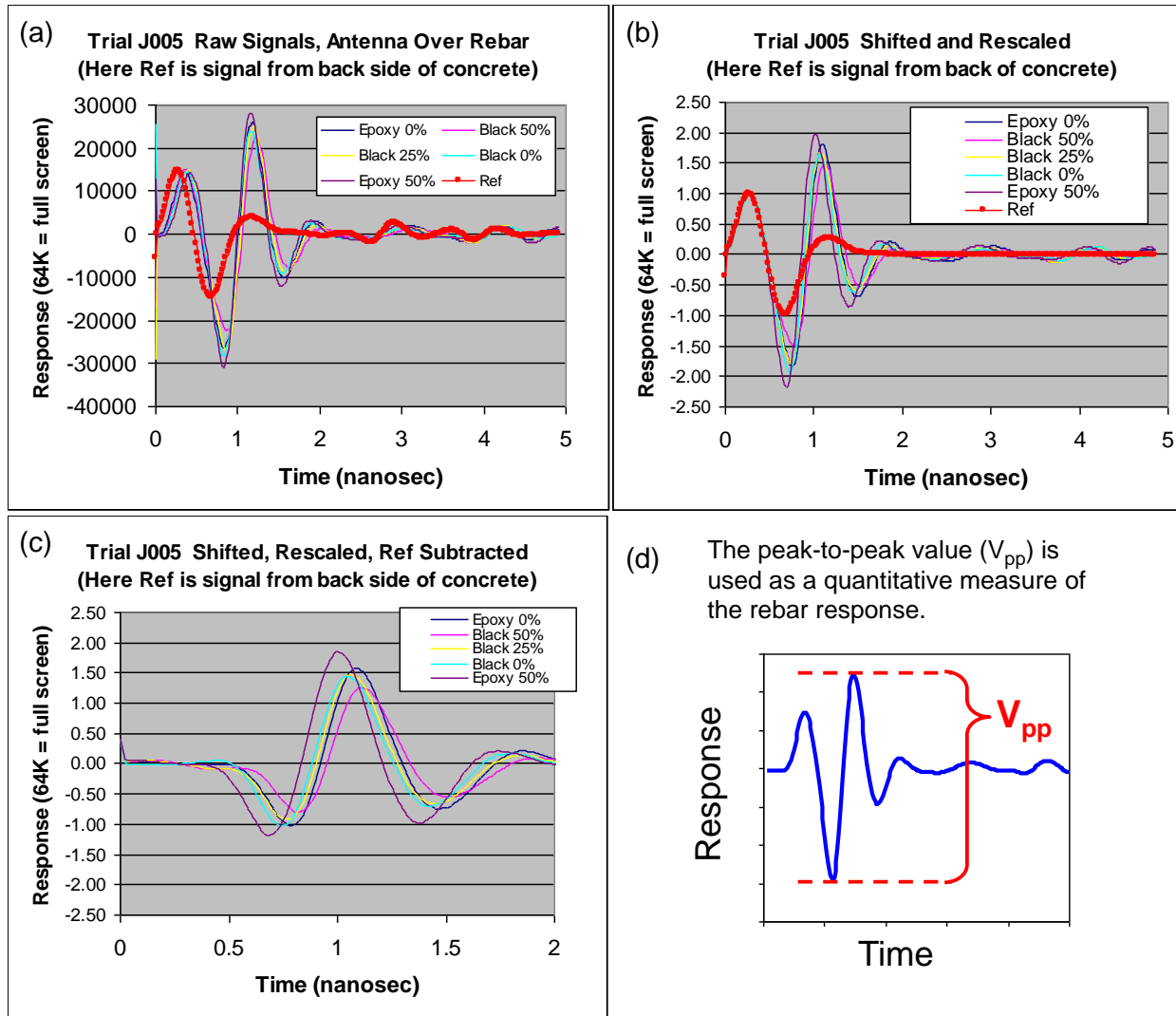
Figure 46. Processing of GPR waveform (A-scan) data from test specimens

Figure 46a shows the raw reinforcing steel responses and a no reinforcing steel reference signal. The portion of the waveform from 0 to 0.5 nanoseconds is due solely to the air/concrete interface reflection. Ideally, all of these early-arriving portions should be identical in the absence of liftoff differences.

In step 2, we forced them to be identical by shifting waveforms slightly and rescaling each waveform such that the early-arriving positive peak near 0.3 nsec had an amplitude of unity. Figure 46b shows shifting and scaling to align the early-time portions of the waveforms. For each reinforcing steel response, the portion of the waveform beyond about 0.5 nsec is a superposition of the responses from the reinforcing steel itself and the air/concrete interface.

In step 3, the reference signal is subtracted, leaving an estimate of the reinforcing steel only signal. Figure 46c shows subtraction of the reference signal to obtain reinforcing steel only responses.

59

Note that this reinforcing steel only waveform has been normalized, with unity now representing the amplitude of the positive peak of the air/concrete interface echo. Figure 46d depicts how the peak-to-peak amplitude of a raw or corrected waveform is reported.

For the GPR inspections of the test blocks, Figure 47 summarizes the measured reinforcing steel responses.
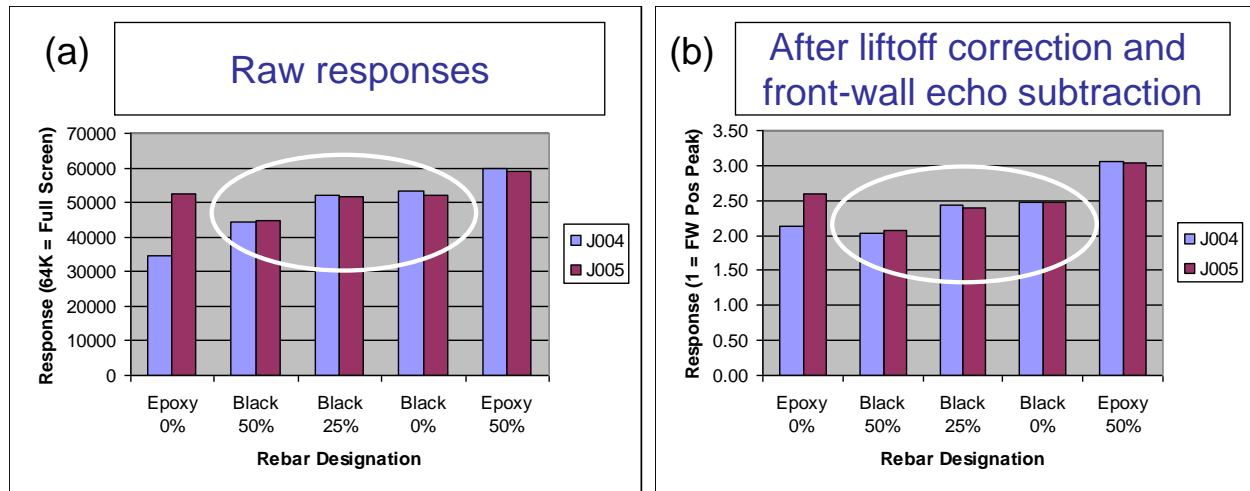
Figure 47. As-measured (a) and corrected (b) peak-to-peak responses for the vertical reinforcing steel in the five test specimens for right-to-left (J004) and left-to-right (J005) measurements

Results are shown for both the as-measured and corrected signals. In either case, as illustrated in Figure 46d, the bar graph displays the peak-to-peak amplitude of the maximal response from each reinforcing steel. Several points can be made in summary:

- For standard black reinforcing steel (see white ovals), the GPR amplitude measurements could readily distinguish a localized diameter thinning of 50 percent (i.e., Black50% versus Black0%), but not a thinning of 25 percent (Black25% versus Black0%).

- The two epoxy-coated reinforcing steel specimens could also be distinguished from each other, but there, the thinned reinforcing steel returned a higher response than the unthinned one. The reason for this is not yet known, but may be associated with the thinned epoxy reinforcing steel being somewhat closer to the antenna than its unthinned counterpart, as indicated by signal arrival times. Given the blocks for the epoxy-coated reinforcing steel specimens were on the ends of the five-block laboratory lineup (see Figure 45), liftoff problems were more severe there, caused by one pair of carriage wheels being off the concrete surface during the beginning and end portions of each scan.

- Processing to correct for liftoff variability reduces the differences between the left-to-right and right-to-left measurements.

Comparing the raw and corrected reinforcing steel amplitudes in Figure 47, the correction procedure does not change the overall trend of the results. However, for ultrasonic inspection, making such amplitude corrections when warranted is considered to be a sound data-analysis practice.

4.3.2   Field Tests at the Highway 210 Bridge

As illustrated in Figure 48, GPR measurements were taken on embedded reinforcing steel on the Highway 210 Bridge barrier rails. The bridge spans about 200 ft (over I-35) and five 6 ft long sections were selected for study, near the crown of the bridge where water drains quickly and near the ends where water tends to collect.
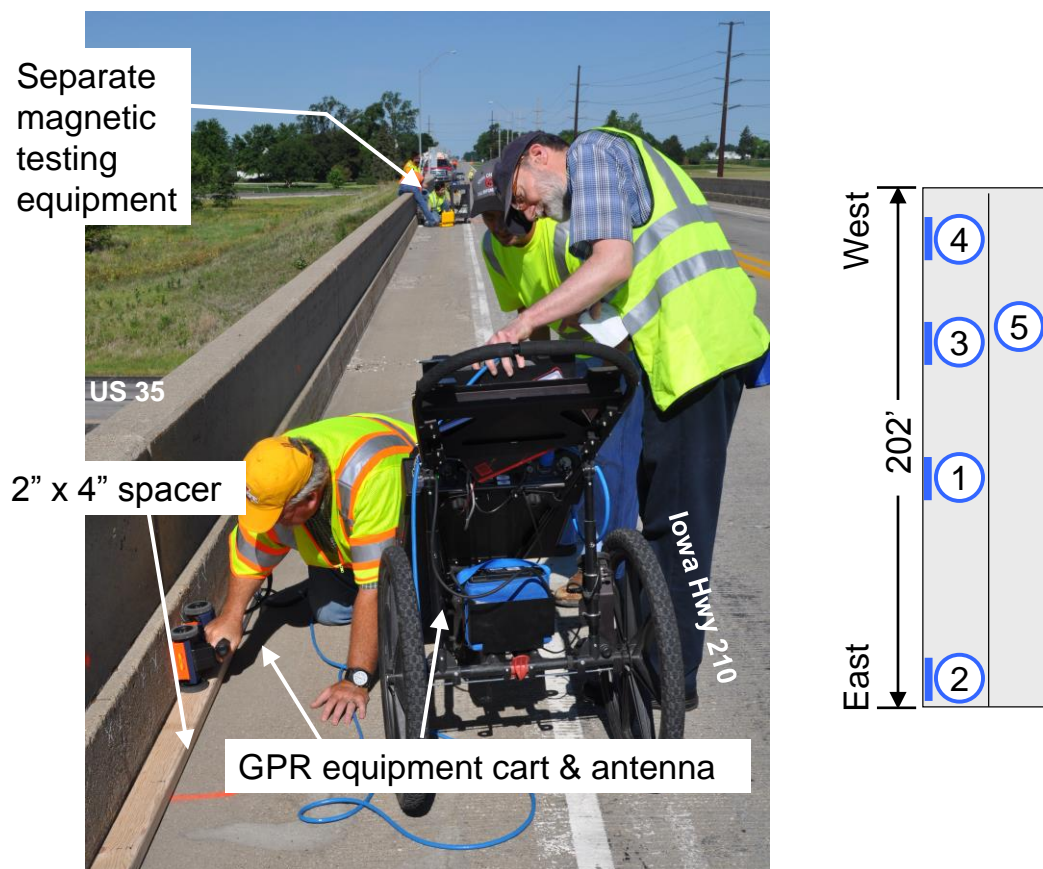
Figure 48. GPR scan showing 2 by 4 being used to elevate antenna above the bridge deck

For the laboratory test blocks discussed earlier, we knew (by design specifications) the degree of reinforcing steel thinning in each concrete test specimen. For the field testing on the bridge, this information was not available. All of the reinforcing steel studied may have been sound; or all or some may have been corroded. As a possible way to distinguish the presence of thinning at the bridge deck, the following strategy was adopted.

Each section was scanned with the antenna carriage flush with the bridge deck and with a (nominal) 2 by 4 in. board placed between the antenna carriage and the bridge deck. The wooden spacer served to elevate the antenna approximately an additional 1.5 in. above the deck and 1.5 in. further from the thinned reinforcing steel zone if thinning was present. It was hypothesized that the difference in signal amplitudes (between a flush-with-deck measurement and elevated measurement) would be larger for thinned reinforcing steel than for sound reinforcing steel.

Each scan was repeated four times: twice with left-to-right antenna movement and twice with right-to-left movement. Therefore, a total of 40 GPR datasets were collected: five sites × once with spacer and once without spacer × two left-to-right scans and two right-to-left scans). GPR data for one of the tests is shown in Figure 49.
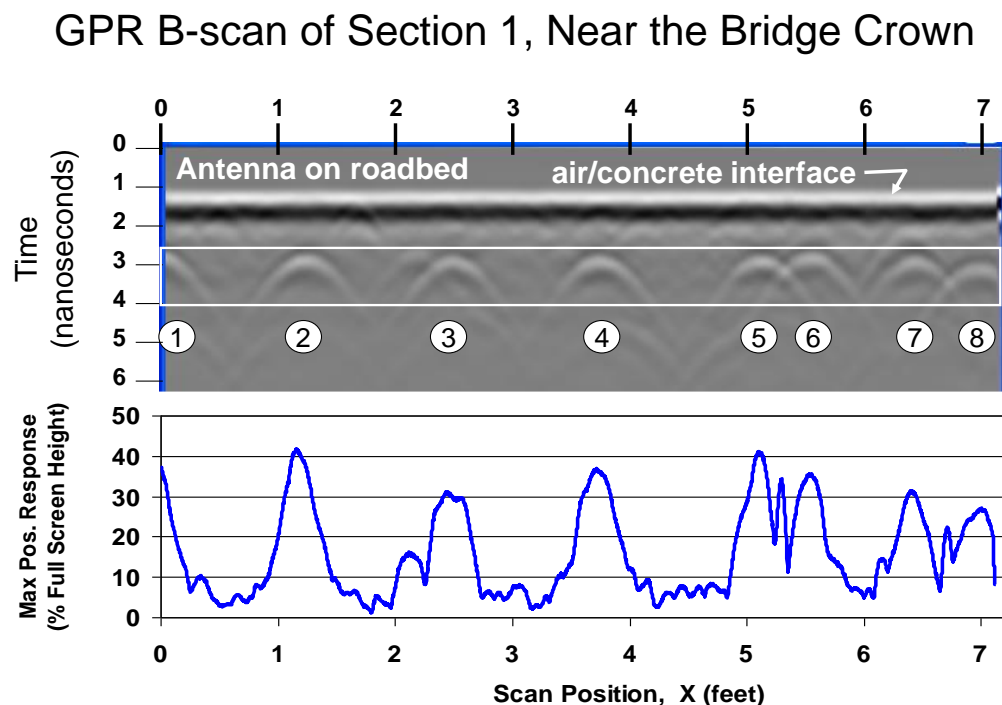
Figure 49. Sample GPR data from field test

The top of Figure 49 shows a B-scan of section 1 near the crown of the bridge with responses from eight reinforcing bars having similar depths in the concrete barrier rail. The graph at the bottom of Figure 49 shows peak positive amplitude versus scan position corresponding to the boxed area (white outline) of the B-scan.

In this case, the region scanned was located at the crown of the bridge and the antenna carriage was flush with the bridge deck (no spacer used). From the B-scan, responses from eight reinforcing bars can be identified; based on arrival signal times, these are all located at roughly similar depths within the barrier rail. The graph in Figure 49 displays the peak positive amplitudes of the eight reinforcing steel echoes; these range from about 25 to 40 percent of full-screen-height at the gain setting used.

Figure 50 compares GPR B-scans for section 2, located at the east end of the bridge.

GPR B-scans of Section 2, Near One End of the Bridge
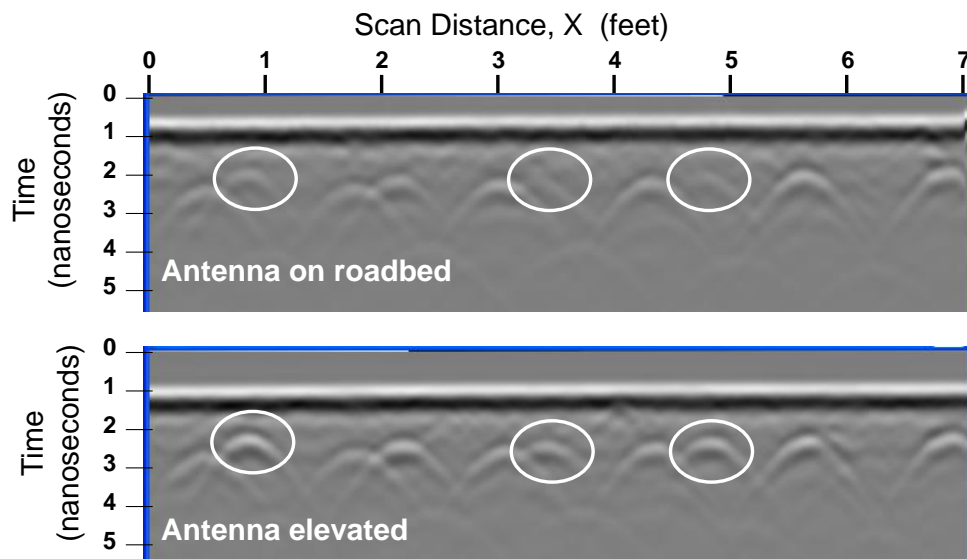
Figure 50. Comparison of GPR B-scans for antenna carriage flush with bridge deck (top) and carriage elevated by the 2 by 4 (bottom)

The white-circled areas identify cases where the reinforcing steel response increases significantly when the antenna is elevated above the roadbed. Such changes may signal reinforcing steel thinning at the bridge deck/barrier rail joint.

Figure 51 summarizes measured reinforcing steel amplitudes for the full set of GPR measurements.

The horizontal axis for each chart identifies bridge sections and enumerates the individual reinforcing bar within each section. The vertical axis displays the measured peak positive amplitude of the reinforcing steel response using a scale where 100 percent denotes the full-display-screen-height (FSH) at the fixed gain used for all measurements.

Blue diamonds denote measurements made with the antenna carriage flush with the bridge deck. Red squares denote measurements made with the 2 by 4 spacer in place on the deck along the edge of the barrier rail.

For each reinforcing steel response, there are four on-deck and four off-deck measurements, corresponding to the four separate measurements taken in the field tests. For a given reinforcing bar, the vertical spread in amplitude for points of a given color/shape is an indication of the measurement uncertainty. Of chief interest here is the average separation between on-deck and

63

off-deck points for a given reinforcing steel, indicating the effect on the reinforcing steel response of elevating the antenna by the thickness of the spacer board.
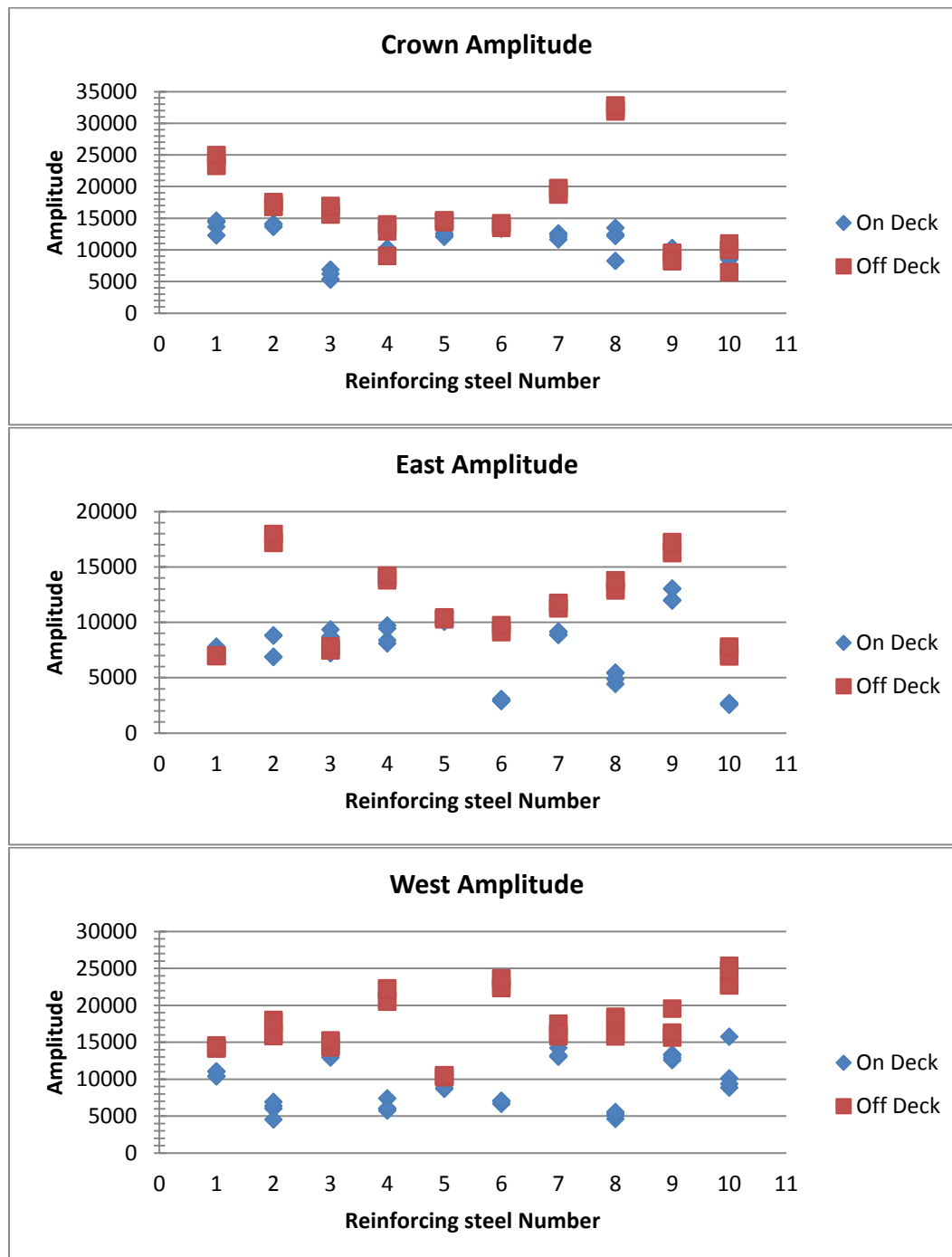
Figure 51. Summary of measured peak reinforcing steel responses for GPR inspection of the bridge barrier rails

In Figure 50, a number of cases are seen where the antenna elevation results in a substantial increase in the reinforcing steel response. One possible explanation for such cases is localized thinning of the reinforcing steel near the bridge deck.

Quantitative data analysis of the individual reinforcing bars for three sections of the south side of the bridge barrier rails reveal suspected reinforcing steel material loss. When plotting the amplitude of the signal for the reinforcing steel within each section, suspected material loss can be identified based on the separation of the reinforcing steel's amplitude when comparing the on-deck versus off-deck signals. The on-deck signal shows lower amplitude overall. However, the suspected reinforcing steel will have a greater separation of the compared signal than the reinforcing steel where no material loss is suspected.

In examination of the arrival time for response, the off-deck signals showed a shorter time of flight than the on-deck reinforcing steel signals. This is primarily due to the geometry of the barrier rail. Assuming that the reinforcing steel were mounted perfectly vertical in the barrier form, and given the slope of the deck-facing surface of the barrier, there is slightly less material (concrete) for the GPR signal to penetrate through for on-deck panels, therefore resulting in a shorter time to the reinforcing steel. This can be seen in Figure 52.

When taking into account the amplitude and the time for the response, we plot the amplitude versus time to understand the combined responses better. For clarity, different symbols were used for the plotted points from different bridge sections in Figure 53.
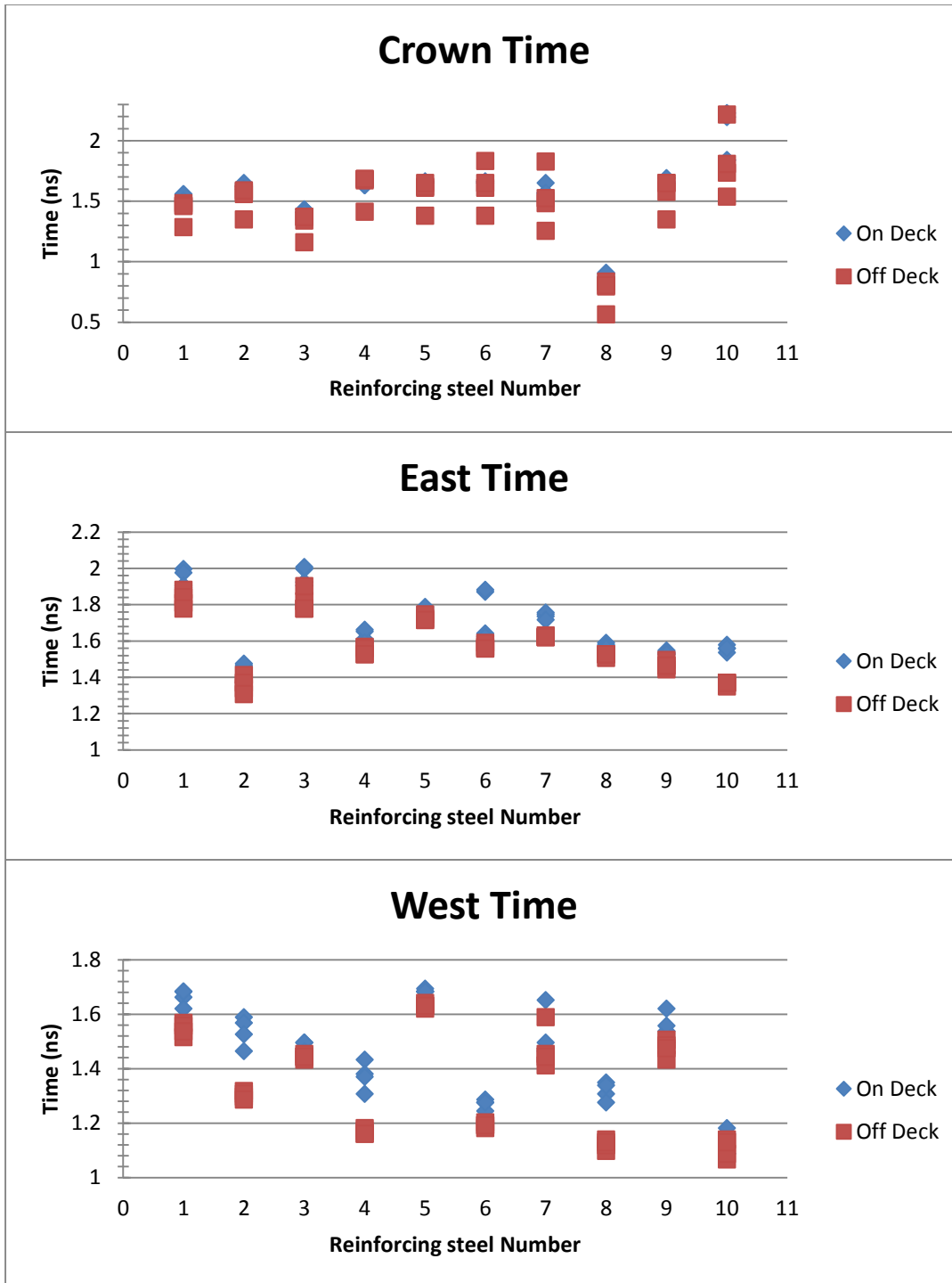
Figure 52. Reinforcing steel signal time of flight on deck versus off deck number for locations near the east, crown and west end of the bridge
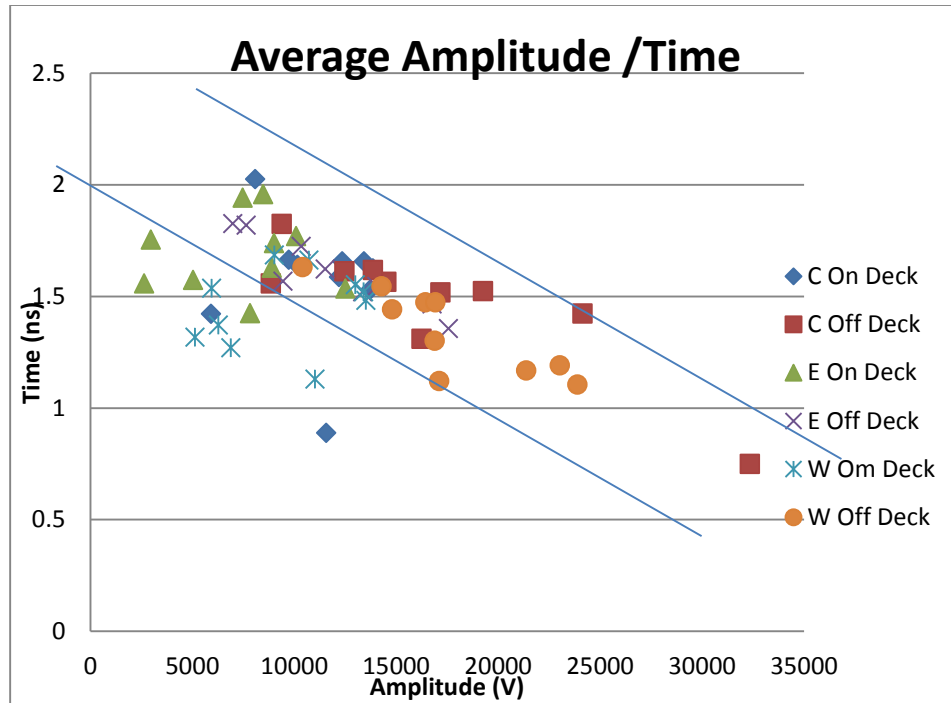
Figure 53. Average time versus average amplitude for all reinforcing steel

As expected, there is a general trend or band where the response falls, with higher amplitude responses correlated with lower time of flight. This general pattern holds true for reinforcing steel that did not show a visual indication of decreased amplitude when comparing the on-deck with the corresponding off-deck response. For reinforcing steel that show a decrease in amplitude, they appear to fall outside of the trend lines shown in Figure 53. Those markers outside the band of concentration are suspect to material loss and are identified in greater detail in Figure 54 with amplitude differences provided in Figure 55.
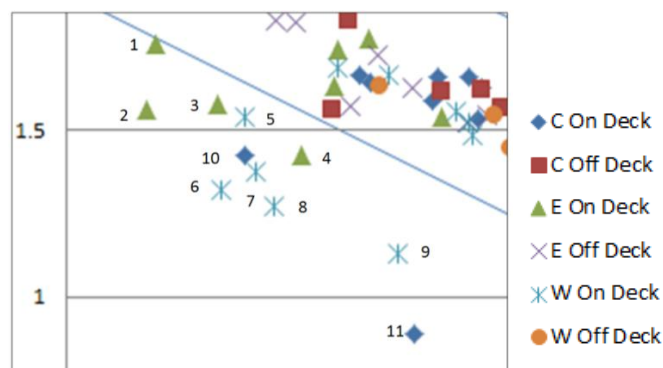
Figure 54. Identification of suspect reinforcing steel

Rebar #	On Deck Average (V)	Off Deck Average (V)	Difference
1	2966	9449	6483
2	2634	7376	4742
3	5044	13359	8315
4	7835	17569	9734
5	5955	16890	10935
6	5133	17112	11979
7	6288	21377	15089
8	6894	23024	16130
9	11015	23886	12871
10	6181	16891	10710
11	11578	32344	20766
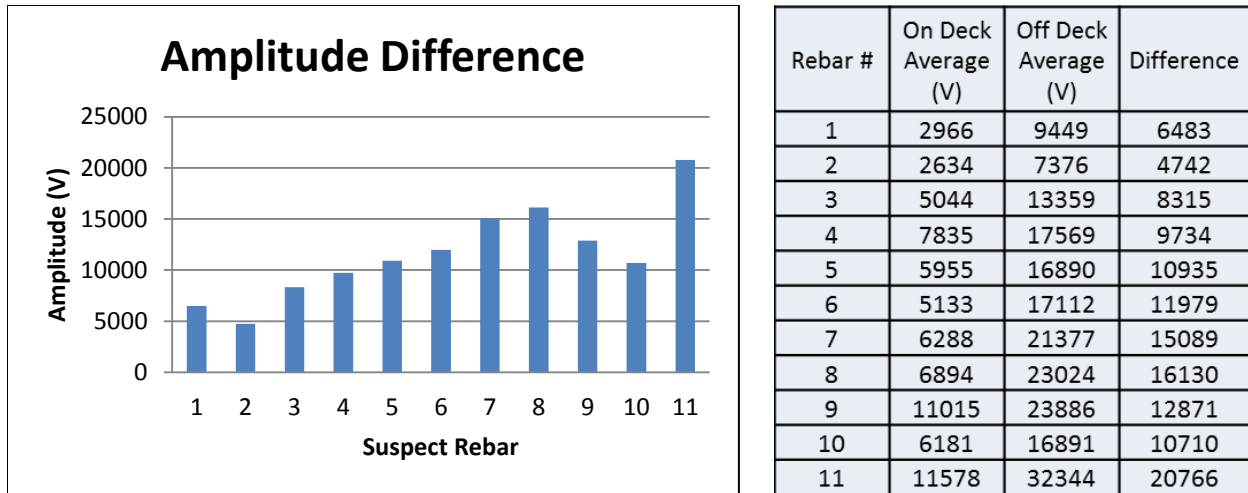
Figure 55. Amplitude difference data for the 11 suspect reinforcing bars

Figures 56 through 58 provide the images of the raw scans as taken in the field. Each reinforcing bar is identified by both the number given to it in Figure 55 (in parentheses) and by the actual number assigned to it in the data processing. Both on-deck and off-deck scan images are shown to illustrate the decreased amplitude of the reinforcing steel, as identified by the area inside the red circles.

Reinforcing steel #

8   (11)   3 (10)

File 002 Crown On Deck

Reinforcing steel #

8   (11)   3 (10)

File 006 Crown Off Deck
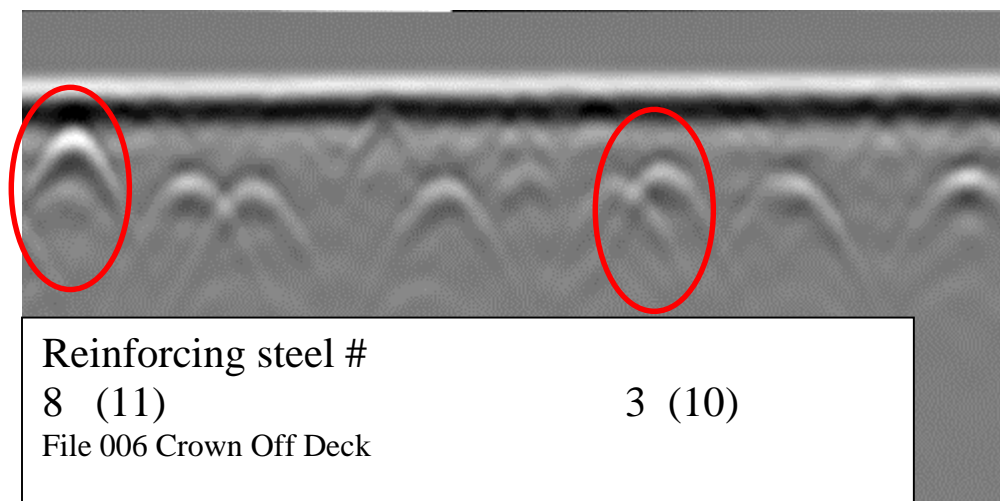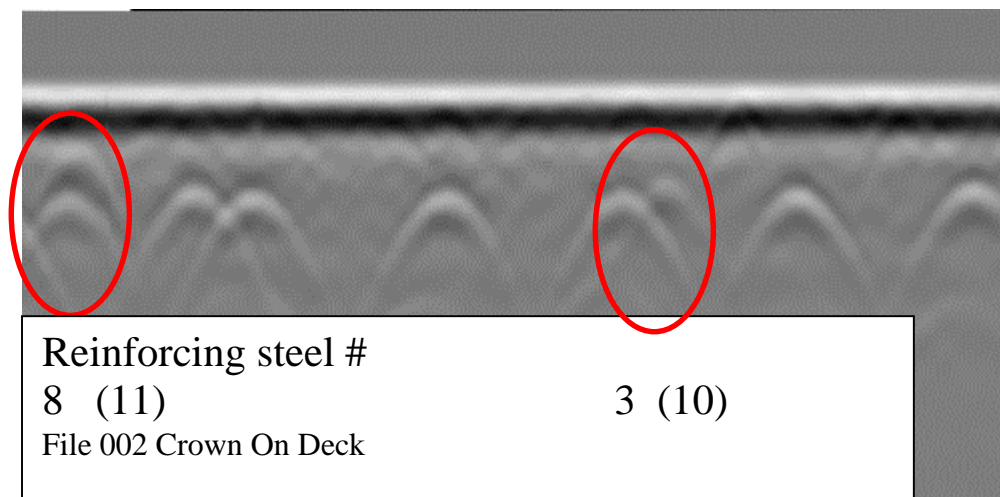
Figure 56. Suspect locations in the crown section

Reinforcing steel #
10 (2)   8 (3)   6 (1)   2 (4)
File 010 East On Deck

Reinforcing steel #
10 (2)   8 (3)   6 (1)   2 (4)
File 010 East Off Deck
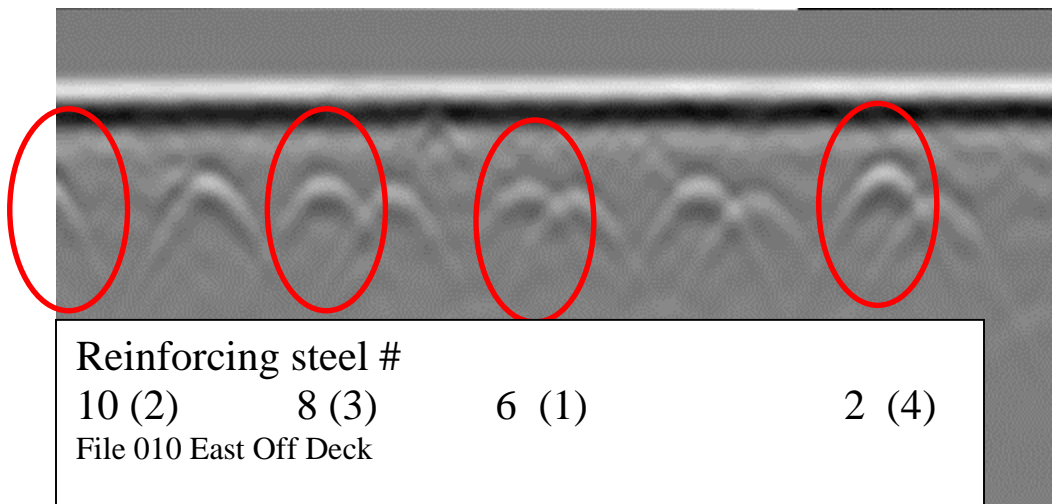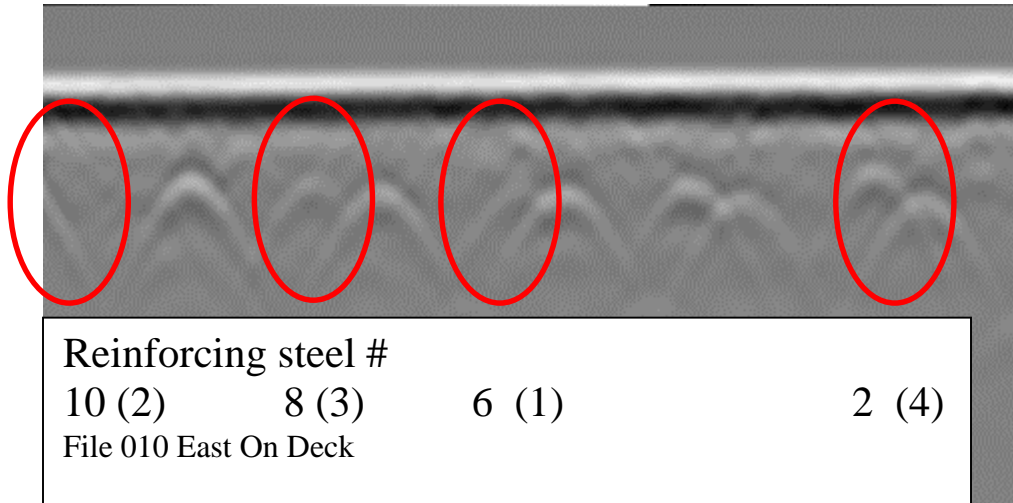
Figure 57. Suspect locations on the east end of the bridge

Reinforcing steel #
10 (9) 8 (6)   6 (8)   4 (7)   2 (5)
File 026 West On Deck

Reinforcing steel #
10 (9)   8 (6)   6 (8)   4 (7)   2 (5)
File 026 West Off Deck
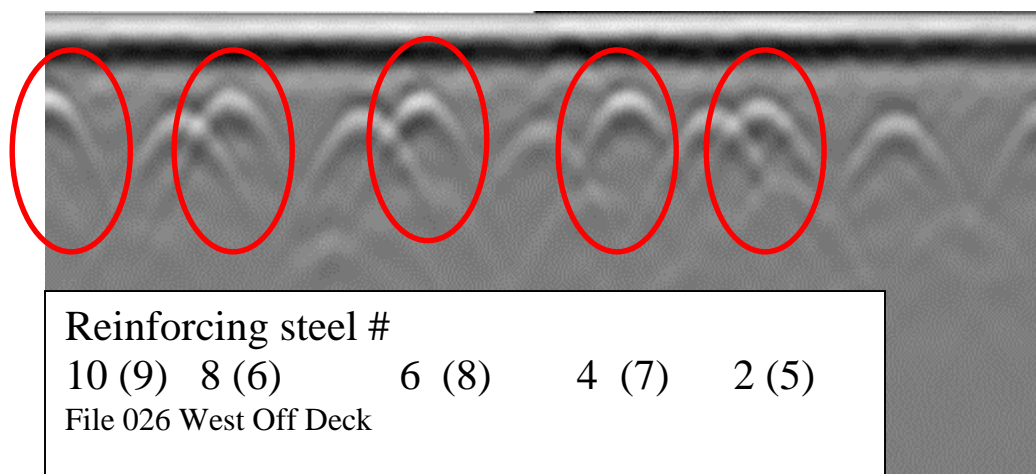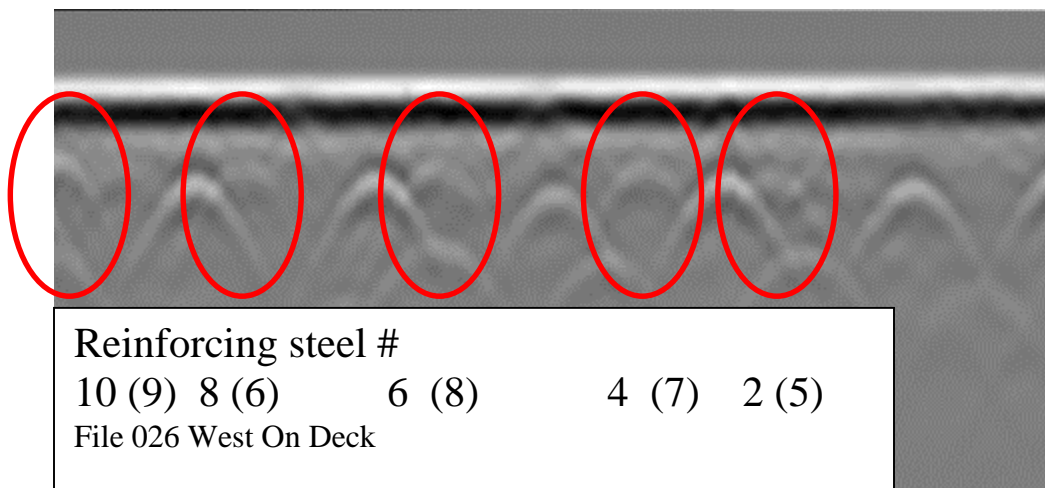
Figure 58. Suspect locations on the west end of the bridge

4.3.3   Summarized Results of the GPR Field Tests

- GPR scans were taken on five sections of the bridge, with each section containing approximately 10 reinforcing bars to reinforce the attachment of the bridge barrier rail to the bridge deck.

- Two measurement setups were used: one with the GPR antenna carriage flush to the bridge deck and one with the carriage elevated by 1.5 in. (1.5 in. further from the zone where corrosion and thinning typically occurs).

- For each bridge section and each setup, four measurement runs were made to check reproducibility. Result-to-result variability was fairly small with the peak positive reinforcing steel response typically varying by about 5 percent of full screen height (FSH).

- In most cases, elevating the antenna had little impact on the reinforcing steel response. This was the case for about 82 percent of the 70 reinforcing bars studied. However, for 11 reinforcing bars, elevating the antenna resulted in a marked increase in peak response, consistent with the expected effect if corrosive thinning were present.

4.3.4   Development of GPR Analysis and Modeling Tools

To field a practical amplitude-based system for detecting thinned reinforcing steel, it is necessary to quantify and assess the many factors that contribute to GPR signal amplitude changes. These include variability arising from the reinforcing steel itself (e.g., reinforcing steel location and thinning) and from other factors (concrete properties; antenna position and orientation; equipment characteristics; etc.). For example, a decrease in the reinforcing steel response during antenna elevation (like those illustrated in Figure 54) might be due to reinforcing steel thinning alone or might be a consequence of a change in some other parameter that influences measured amplitudes.

Analogous to earlier ultrasonic modeling efforts at CNDE, we began work to develop a measurement model that can be used to simulate GPR inspections. One eventual goal is a simulation tool to predict how the pulse/echo response from a given reinforcing bar depends on the degree of thinning and on the position and orientation of the reinforcing steel relative to the antenna. As illustrated in Figure 59a, the simulation tool will predict the reinforcing steel response A-scan, given the inspection geometry and pertinent information about reinforcing steel and concrete properties.

As illustrated in Figure 59b, several physical processes must be understood and modeled to predict the reinforcing steel A-scan response.
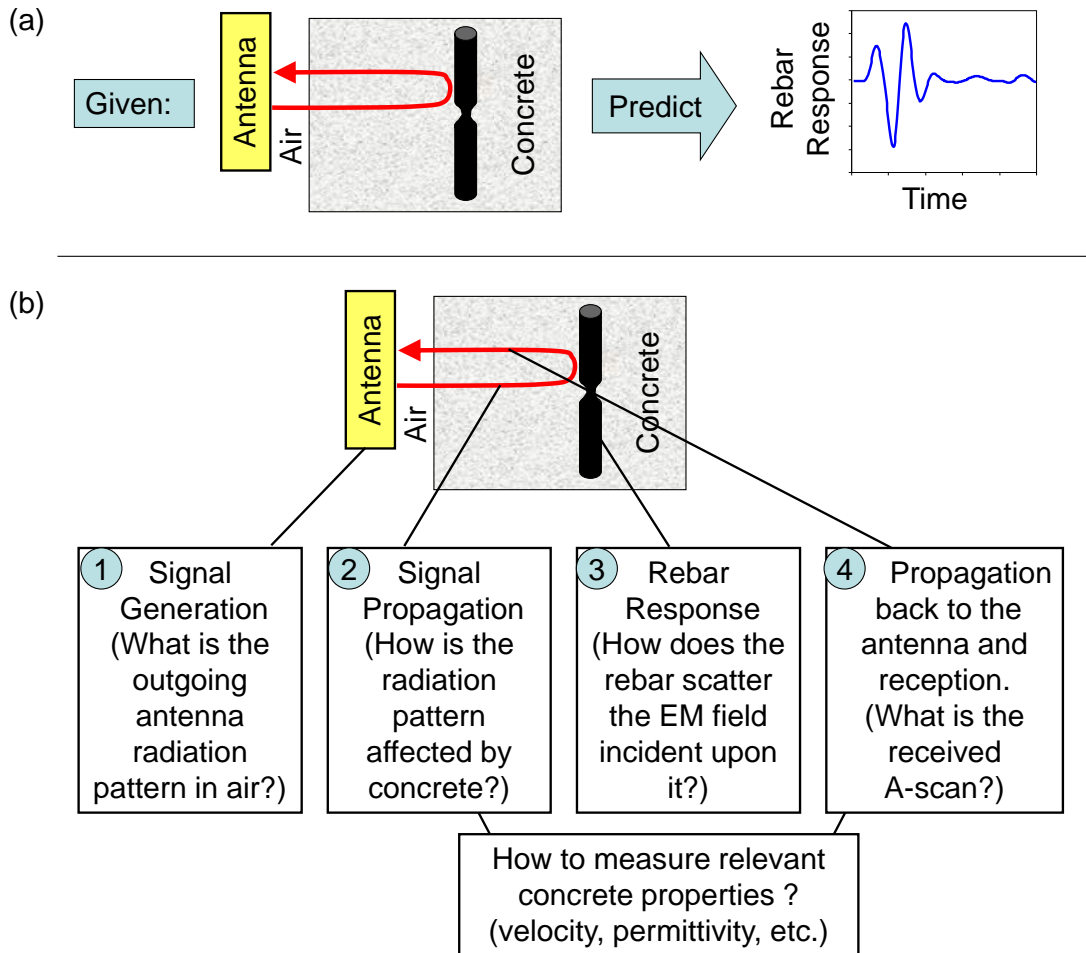
Figure 59. (a) Simulation tools under development to predict GPR reinforcing steel responses and (b) several processes contribute to the measured response

These processes include the following:

- Outward radiation of EM energy by the antenna
- Modification of the broadcast radiation pattern by refraction and absorption during propagation through concrete
- Scattering by the reinforcing steel of the incident EM field
- Backward propagation of the scattered field and its reception by the antenna

In addition, the researchers must develop sensible methods for measuring pertinent properties of the materials involved, such as the wave speed and attenuation in concrete. In these modeling and measurement endeavors, we are proceeding in analogy to prior ultrasonic work performed at CNDE, essentially bringing well-tested UT approaches to bear on GPR inspection problems.

Some aspects of this ongoing development work are described briefly below.

The commercial software that accompanies the GSSI GPR instrument is geared primarily toward providing and manipulating B-scan images for visual interpretation by the user. A-scan data can be viewed graphically, but there is no option for outputting an A-scan in numerical form, i.e., as a list of (time, voltage) pairs from which peak responses can be readily obtained. Such numerical values are required to quantify reinforcing steel responses accurately and to construct comparative graphs like those shown in Figures 51 through 55.

In the early stages of this reinforcing steel research project, it was necessary to develop special-purpose software to read the raw GSSI data files and to analyze those data in various ways as shown in Figure 60.

```
Program GPR_Stats     Version 2.0      15Aug2012

Do you wish to  :

0:  Stop the program.
1:  Read a primer about using this program.
2:  Input a raw GPR data file.
3:  Compute statistics for one hyperbola.  (Do 2 first).
4:  Output max and min responses versus X  (Do 2 first).
5:  Output selected A-scans ("wiggle plots").  (Do 2 first).
6.  Estimate EM wave speed from one hyperbola shape.  (Do 2+3 first).
7.  Apply synthetic aperture focusing techniques (SAFT)  (Do 2+6 first).
8:  Output a reduced-area Tiff image (Do 2 or 2+7 first).
        Enter your choice :
```

Figure 60. Data analysis operations available in the special-purpose software written to analyze GPR data collected and stored by the GSSI instrument

Software development is ongoing with new analysis tools being added as needed. Analysis tools are generally first developed and tested using Fortran code, and then translated into the C+ language, which facilitates implementation of graphical user interfaces (GUIs) and other user-friendly features.

Options 3, 4, and 5 of the software in Figure 60 are used routinely to extract numerical values for tabulation or graphing, such as the peak response seen when the GPR antenna is scanned over a given reinforcing steel target. Separate inspection simulation models that are under development require as inputs certain material parameters, such as the EM wave speed in concrete.

Option 6 in Figure 60 provides one way of estimating the EM wave speed. Recall from Figure 44c that the shape of the hyperbola seen when the antenna is scanned above a small object depends on the wave speed in the embedding medium. In particular, the slope of the asymptote to the hyperbola is twice the reciprocal of the wave speed. Therefore, by fitting a mathematical hyperbola to a reinforcing steel response-versus-distance curve, we can estimate the wave speed (v) in concrete and, hence, the dielectric constant of concrete (ε). The process is illustrated in Figure 61.

Scan Position, X

0 nsec

Time

5 nsec

Time to Positive Crest (nanoseconds)

Scan Position, X (feet)

The B-scan image above shows the response obtained by scanning the antenna over a concrete test block containing one rebar target. Note the white crest (positive voltage crest) of the rebar response. At right we plot the pixel coordinates closest to that crest at each discrete scan position.

The red curve above is a best-fit hyperbola to the pixel coordinates along the crest (blue points). From the slope of the asymptote to the hyperbola we estimate the wave speed in concrete to be about 12.7 cm/nsec, corresponding to a dielectric constant for concrete of $\varepsilon = 5.6$

Figure 61. Estimation of the dielectric constant of concrete from a B-scan image of embedded reinforcing steel

Another option added recently to the analysis software under separate funding allows the use of synthetic-aperture focusing techniques (SAFT) to enhance the responses of weak reflectors. Our GPR antenna does not provide a focused electromagnetic beam, but rather a beam that spreads out as it propagates. If the beam were focused at a particular depth, reflected signals from objects at that depth would be enhanced.

SAFT provides a way to improve image quality to that comparable for a focused antenna. This is done by combining measurements obtained sequentially at an array of spatial positions using our single non-focused antenna. Such techniques are used extensively in related RADAR applications of aerial reconnaissance and planetary exploration. The basic idea is illustrated in Figure 62a.

The A-scans gathered at different antenna positions (A, B, C) are shifted in time to account for their different travel times to a target point. The shifted A-scan responses are then summed to obtain a new response value that is then assigned to the target point. This process is repeated for every possible target point in the image.

Figure 62b illustrates the application of SAFT in one case. The original pre-SAFT image was obtained by scanning the antenna across the back sides of two abutting concrete test blocks, each containing one reinforcing steel target. After SAFT processing, response hyperbolas of the two reinforcing bars have been greatly compressed in the horizontal direction, resulting in higher-amplitude peak responses and more readily identified reinforcing steel locations. Our addition of SAFT to image processing is a very recent development still undergoing testing and refinement.

It has not yet been applied systematically to reinforcing steel responses from laboratory test specimens or bridge inspection/field testing.
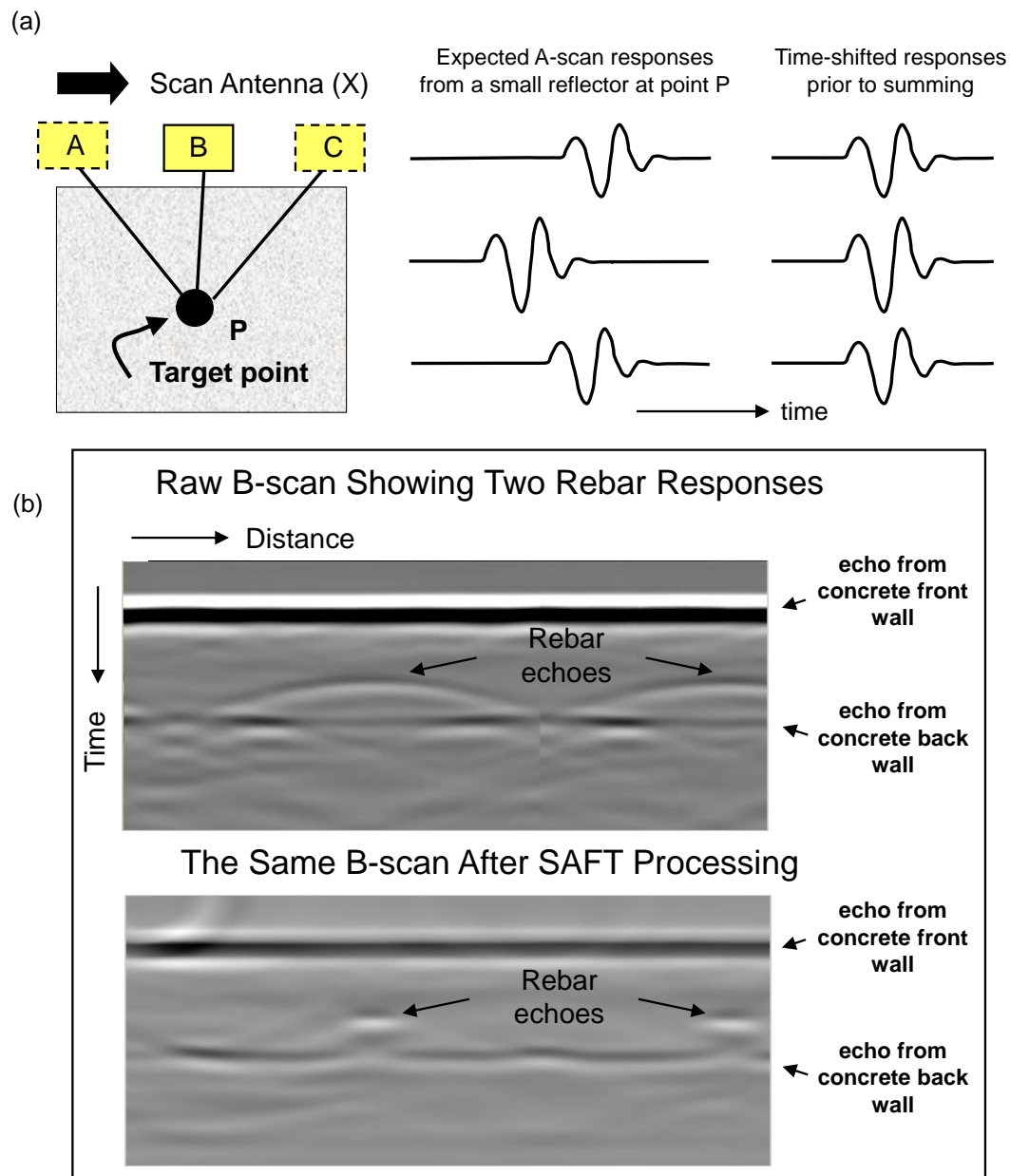
Figure 62. (a) Principle underlying SAFT processing and (b) application of SAFT to a scan over abutting concrete test specimens containing two reinforcing steel targets

During the research period, work also commenced to develop simulation models for the reinforcing steel inspection process, under separate funding. This is envisioned as a four-step process:

1. Map the radiation pattern of the GSSI 1.6-GHz antenna.

2. Fit the measured radiation pattern to that of a simple model antenna.

3. For the model antenna radiating toward a reinforcing steel in air, develop expressions to predict the reflected response from the reinforcing steel as functions of reinforcing steel size, location, and orientation.

4. Repeat step 3 for a reinforcing bar embedded in concrete, taking into account pertinent properties of concrete (wave speed, attenuation).

To date, substantial progress has been made on steps 1 and 3. Step 3 is actually required to carry out and test the fitting process indicated in step 2 given that a portion of the antenna-mapping measurements use reinforcing steel-like targets (bars).

Preliminary mapping of the antenna radiation pattern was performed as illustrated in Figure 63. A wooden frame was constructed containing two rails on which the antenna carriage could roll, with the antenna itself radiating through the air gap between the rails. A steel rod or bar was placed below the antenna serving as a reflecting target. The target was placed on a foam-backing pad that reflected little or no EM radiation and the antenna was scanned from above. The process was repeated for various choices of antenna-to-target distance or, in the case of the ball target, the lateral offset distance.

Figure 63a depicts mapping the antenna radiation pattern using rod and ball targets. Figure 63b shows, for the rod target, B-scans for three choices of the air gap between the antenna and the rod, and corresponding A-scans for the peak response points (vertical white lines on B-scans).

For the steel rod target and three choices of the air gap, Figure 63b shows B-scans and A-scans recorded during the measurements. Note as the distance (air gap) between the antenna scan line and the steel bar increases, the echo from the bar arrives later in time and weakens in amplitude.
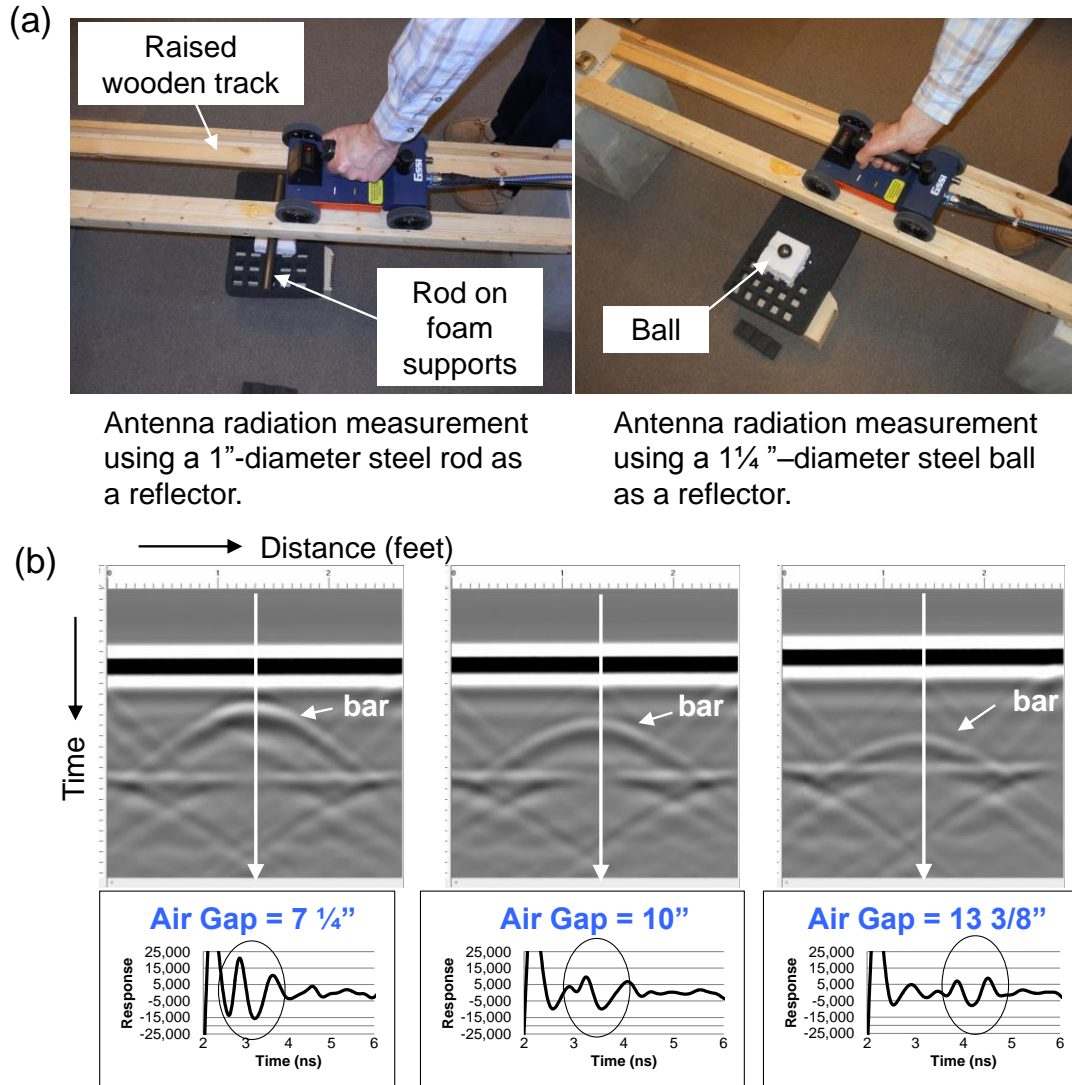
Figure 63. (a) Mapping the antenna radiation pattern using rod and ball targets and (b) B-scans for three choices of the air gap between the antenna and the rod target and corresponding A-scans for the peak response points

To approximate the dipole antenna radiation pattern, simple beam models are currently being explored. If these prove unsatisfactory, models that are more complex will be considered. The antenna is presently being modeled as an effective radiator having two independent size parameters, analogous to a rectangular transducer in ultrasonics. The values of the size parameters will eventually be determined by fitting to the combined rod and ball data.

Analogous to the ultrasonic Thompson-Gray measurement model, we can construct a GPR model to predict how the reflected response from reinforcing steel depends on the reinforcing steel location and diameter. A preliminary version of such a model has been formulated and Figures 64b and 64c show its predictions for cylindrical reinforcing steel in air, assuming antenna-size parameters based on the antenna housing dimensions.

78
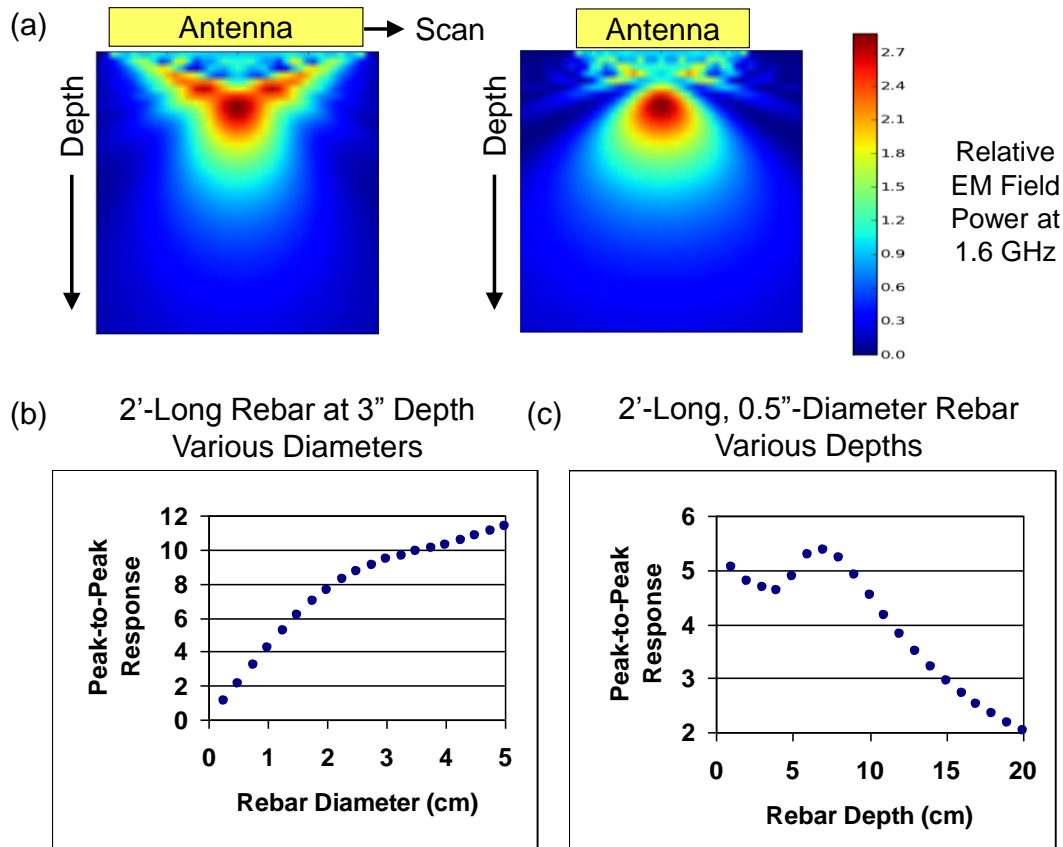
Figure 64. (a) Predicted antenna radiation pattern at 1.6 MHz assuming antenna size parameters based on the physical dimensions of the antenna housing (b-c)

Two cases are illustrated: dependence of reinforcing steel response on reinforcing steel diameter when there is a fixed distance of 3 in. between the antenna and the reinforcing steel and dependence of reinforcing steel response on antenna-to-reinforcing steel distance for a fixed reinforcing steel diameter (0.5 in.).

For the moment, the size parameters have been estimated from the physical dimensions of the antenna housing. Given the two size parameters, the radiation pattern in air can be predicted, as illustrated in Figure 64a. There, each colored image is 20 by 20 cm, with the leftmost image showing the plane containing the antenna scan direction and the rightmost image showing the plane normal to the scan direction.

For the 1.6 GHz component displayed in Figure 64a, the EM field intensity peaks in the near field about 6 cm from the antenna before diverging at larger distances. Figure 64a depicts the predicted antenna radiation pattern at 1.6 MHz assuming antenna size parameters based on the physical dimensions of the antenna housing. For reinforcing steel in air, predicted dependence of the measured response is shown on reinforcing steel diameter (Figure 64b) or depth below the antenna plane (Figure 64c).

Our broadband antenna radiates over a range of frequencies from about 0.8 to 2.4 GHz in practice. The radiated intensity pattern depends on frequency, tending to diverge faster at lower frequencies.

We hope to extend the model soon to treat reinforcing steel embedded in concrete, including reinforcing steel that is thinned in local regions. In addition, work is planned to refine the antenna size parameters by fitting them to the measured bar and ball data.

5 CONCLUSIONS AND RECOMMENDATIONS

Three technologies were evaluated for their abilities to detect and quantify corrosion damage in reinforcing steel used in bridge barrier rails. A two-phase approach that included laboratory evaluation on typical sample geometries was followed by a limited, field feasibility study on the Iowa Highway 210 Bridge over I-35 south of Ames, Iowa. Application of radiography to this problem was limited to the laboratory evaluation. Summaries for each of the methods follows:

- X-ray radiography provides clear images of the condition of reinforcing steel in concrete. This has been demonstrated previously using film. To date, there has been a reluctance to use this technique due to the cost of equipment and the slow feedback for film radiography. In our laboratory studies, we were able to demonstrate that locating corroded reinforcing steel in concrete bridge barrier rails is achieved easily using digital radiography. This approach provides feedback time of less than one minute per location. Furthermore, the image gives a direct visual measure of the extent of corrosion.

  However, the equipment that was available for this study is not optimal for inspection of this type of object. In particular, the x-ray sources available currently in our laboratory are of relatively low power (320 kV). Although adjustment of the exposure parameters to obtain good images is feasible, a higher potential tube would be more efficient. The detector used was also quite bulky and inefficient for field application. Several digital x-ray imagers are available that would be more efficient for this application.

- The simulation model, XRSIM, was useful in guiding selection of the optimum setup parameters. The early experimental success meant that we did not need to rely on XRSIM to extrapolate to higher energy sources. The comparisons that we made between experimental and simulated results indicated that our understanding of the scattering processes in such thick materials is incomplete. This will guide us toward further fundamental work in developing simulations of the scattering process.

- An x-ray backscatter configuration was also evaluated and showed some promise. However, we were not able to identify the location of the embedded reinforcing steel consistently. Earlier work indicated good results using a cesium (Cs) radioactive source (662 keV). This is much higher energy than our x-ray tube is capable of producing. However, a radioactive source requires much longer time for imaging and has safety concerns. Linear accelerators (linac) can produce the required high energies without these concerns. It is recommended that backscatter studies should be completed using a higher energy x-ray source.

- It was not possible to evaluate either of these x-ray techniques on actual bridge barrier rails. This was due to the necessity to follow state regulations for x-ray system licensing and safety, which was beyond the scope of this short demonstration. There are companies that are already licensed in Iowa to operate x-ray systems in an open outdoor environment. As a follow on to our studies, it would be useful to contract with such a company to do field tests.

- The use of GPR was investigated to detect corrosion-induced reinforcing steel thinning in concrete bridge supports. The approach was based on observing the peak amplitude of the reflected GPR signal from embedded reinforcing steel. Other things being equal, localized thinning is expected to lower the GPR response, given thinned reinforcing steel presents a smaller reflecting target to the incoming electromagnetic pulse. In measurements on reinforcing steel in concrete laboratory specimens, amplitude change was able to detect 50 percent thinning reproducibly but not 25 percent thinning.

  Field measurements were conducted on the Highway 210 Bridge over I-35. There, the approach was to look for a change in reinforcing steel response as the GPR antenna was elevated above the bridge deck (i.e., moved away from the likely location of any corrosion-induced thinning). Several instances were seen in which antenna elevation resulted in a marked increase in reflected amplitude, consistent with expectations for reinforcing steel thinning at the deck. However, reflected amplitude can be changed by many factors in addition to reinforcing steel thinning (e.g., reinforcing steel location and orientation, concrete property variations). Simulation models can be used investigate the relative importance of such factors and work was begun on developing such models for simulating the reinforcing steel inspection process. Use of radiography in the suspect locations would validate the GPR results. Destructive removal of concrete could also be used to verify condition.

- A three-stage study was carried out to evaluate the feasibility of detecting damage of reinforcing steel near the cold joint of bridge structures by the EC and MFL techniques. A commercial EC-based reinforcing steel locator was acquired and an MFL sensor probe was developed using GMR sensors for the study. In Stage 1, EC and MFL measurements were carried out on a set of bare, standalone #4 reinforcing bars with and without artificial defects. Both EC and MFL can detect 25 and 50 percent material loss readily in the standalone reinforcing steel at the minimum required distance of 2.5 in. (63.5 mm). The EC and MFL signals were both found to decrease monotonically as the amount of material loss increases, indicating the potential of using the techniques to quantify material loss of standalone reinforcing steel.

- EC and MFL measurements were conducted on test specimens containing multiple #4 or #6 reinforcing steel, with or without artificial defects, embedded in concrete according to the design provided by Iowa DOT. Both EC and MFL signals were found to be affected by other reinforcing steel near the cold joint, but the signals detected away from the interfering reinforcing steel are dependent on the amount of local material loss of the vertical (anchoring) reinforcing steel. The results indicate the possibility of using the techniques to detect reinforcing steel damage in realistic bridge structures, provided that other methods are available to provide independent survey of the distribution and orientation of reinforcing steel over the region of interest, so that the potential interference of other reinforcing steel on EC and MFL inspections can be minimized and quantified.

- In the field test carried out on the Highway 210 Bridge over I-35, MFL line scans were performed on and off the bridge deck across 18 reinforcing steel locations selected from four different sections of the bridge. Thirteen inspected locations showed stronger off-deck MFL

signals, suggesting possible damage in the reinforcing steel near the cold joint based on the results obtained from the test specimens. By comparing the MFL and GPR scan results, the researchers found that MFL gave the same predictions as GPR for 16 of the 18 embedded reinforcing steel locations tested.

- Given that no destructive examination of reinforcing steel on the Highway 210 Bridge will be performed to validate the field tests, the GPR and MFL results were compared to determine whether the two techniques give consistent indications of the reinforcing steel condition suspected. Similar to the GPR tests, MFL scans were performed on the same sections by scanning the antenna on the bridge deck and after it was raised 1.5 in. off the deck, to examine any change in signal that would indicate reinforcing steel damage.

- When comparing the on-deck and off-deck GPR signals, most of the hyperbolae, each of which indicates the presence of reinforcing steel, show the same on-deck and off-deck signal level, indicating that those reinforcing bars are possibly undamaged. The exceptions are those locations where hyperbolae show a significant increase in the off-deck signal compared to the on-deck signal, suggesting possible reinforcing steel damage.

In comparison, the MFL scan results were found to be consistent with the GPR data. Similar qualitative comparison between the MFL and GPR field test data was made. The results are summarized in Table 5, which lists the predicted reinforcing steel conditions based on the MFL and GPR data. It is evident that in most cases (16 of 18) MFL gives the same predictions as GPR, except for reinforcing steel E-4 in the east-end section and reinforcing steel W-1 in the west-end section, where MFL indicated possible damage while GPR did not.

Table 5. Comparison of MFL and GPR prediction of damage

	Crown				East end								West end			Section 4		
Rebar	C-1	C-2	C-3	C-4	E-1	E-2	E-3	E-4	E-5	E-6	E-7	E-8	W-1	W-2	W-3	CW-1	CW-2	CW-3
MFL	N	N	N	Y	N	Y	N	Y	Y	Y	Y	Y	Y	Y	Y	Y	Y	Y
GPR	N	N	N	Y	N	Y	N	N	Y	Y	Y	Y	N	na*	Y	na	na	na

Y: Positive indication of possible damage
N: No indication of possible damage

* na: GPR data not available for comparison

6   FUTURE RESEARCH

- Given the rapid improvements in digital radiography, reevaluation is recommended for the use of x-ray imaging of reinforcing steel in concrete, as well as for other issues with concrete structures. Digital x-ray imaging can provide feedback times comparable to other techniques, and produce images that are relatively easy to interpret. The shorter feedback time and more-efficient detectors also result in reduced radiation exposure, thereby greatly reducing risks to workers and the public. A logical next step would be to contract with a company that has proper licensing and the appropriate digital radiography equipment to perform field tests. The XRSIM model will be useful in predicting the geometric setup for field tests. Further work on the scattering portion of the model will be required before it can be used to predict exposure settings.

- Backscatter imaging is seeing increased use in inspection of relatively low-density objects. It is especially useful when it is not possible to access both sides of an object. Extension to use on high-density materials, such as concrete, requires more research, particularly extending work to higher energies.

- Results of the three-stage study show the potential for EC and MFL in detecting reinforcing steel damage not only in laboratory specimens but also in realistic bridge structures. Nevertheless, the researchers point out that both techniques, in the current state of development, have limitations and require further research before they can be considered as viable techniques for field inspections. Specifically, the current probe designs for EC and MFL tests lack the capability to separate the contributions of multiple signal sources and therefore the detected signals are susceptible to interference by other reinforcing steel nearby. The measurement ranges of the commercial EC instruments and the MFL system developed in this work are limited to within a few inches, although these can extended by improving the probe design and signal processing for higher sensitivity. Based on the results of the feasibility study, further research and development is recommended as described below to improve the technical readiness of EC and MFL for reinforcing steel inspection.

- The EC and MFL signals detected using the present sensor probes are susceptible to interference by other reinforcing steel near the cold joint. This problem can be addressed by using a linear array of multi-axial magnetic field sensors for both EC and MFL measurements. Each of the sensors will detect the EC field or leakage flux from defect in multiple directions. This aims to map the magnetic field pattern and use it to separate the influence of nearby reinforcing steel from defect signals, based on the fact a defect produces a distinctively different leakage field pattern from that of intact reinforcing steel. Under AC field excitation, both the amplitude and the phase of the detected field signals can be used to correlate with the reinforcing steel size (diameter) and distance from the sensor probe. This will help alleviate the need for other techniques to survey the distribution of reinforcing steel in concrete structures under inspection.

- Hardware development is needed to improve the speed of EC and MFL for inspecting large-scale civil structures. For field inspection, both EC and MFL measurements rely on manual

scanning of the sensor probe over the region of interest and require manual registration of probe locations for data analysis, which is time consuming. The inspection time can be reduced by using a portable, linear scanner stage under computer control that will scan the sensor probe across the region under inspection. A linear position sensor can be used to register the positions of an EC or MFL probe for producing line scan results automatically. Another factor limiting the inspection speed of MFL is excitation field frequency, which was fixed at 20 Hz for this project to optimize the signal-to-noise ratio and the measurement range. The inspection time can be reduced significantly by using a higher field frequency, which will require an upgrade of the power amplifier to drive the electromagnet.

- Although consistent indications of possible reinforcing steel damage were obtained from the MFL and GPR field test data, neither technique has been validated through direct examination of the inspected reinforcing steel. Further MFL and GPR studies on sacrificial structures are recommended to validate both techniques. Once the techniques have been validated, further work is recommended to study the dependence of MFL signals on the cross-sectional area of reinforcing steel and their distance from the sensor probe so that they can be determined by MFL measurements. Development of a dual antennae approach for GPR would speed the inspection and data analysis processes, leading to an improved field decision regarding extent of damage.

- To field a practical amplitude-based system for detecting thinned reinforcing steel, researchers must be able to quantify and assess the many factors that contribute to GPR signal amplitude changes. Commercial software is geared primarily toward providing and manipulating B-scan images for visual interpretation by the user. A-scan data could be viewed graphically, but there is no practical way to process individual A-scans and extract numerical values for peak responses and other characteristics. Such numerical values are required to quantify reinforcing steel responses accurately and to construct comparative graphs for analysis. In the initial phase of the reinforcing steel research project, it was necessary to develop special-purpose software to read the raw data files and to analyze those data in various ways. Continued software development using the C+ language is required to develop new analysis tools needed for the determination of thinned reinforcing steel. Some software tools will be relatively simple in intent, such as the ability to locate the peak response and its corresponding arrival time within a user-selected box on a B-scan. Others tools will be more sophisticated, such as the ability to fit a hyperbola to a reinforcing steel response crest and then determine an effective EM wave speed from the shape of that hyperbola.

- A second phase in the development of analysis software is the use of synthetic aperture focusing techniques (SAFT) to enhance the responses of weak reflectors. The GPR antenna is not a focused antenna. If it were focused at a particular depth, reflected signals from objects at that depth would be enhanced. SAFT provides a way to improve image quality to that comparable for a focused antenna by combining measurements made at a sequence of lateral positions. The A-scans gathered at different antenna positions (A, B, C) are shifted in time to account for their different travel times to a target point. The shifted A-scan responses are then summed to obtain a new response value that is then assigned to the target point. This process

is repeated for every possible target point in the image. After SAFT processing, the response hyperbolas of the reinforcing steel is greatly compressed in the horizontal direction, resulting in higher-contrast peak responses and more readily identified reinforcing steel locations.

- As with past ultrasonic modeling efforts, efforts could begin to develop a measurement model that can be used to simulate GPR inspections. The eventual goal would be a simulation tool to predict how the pulse/echo response from a given reinforcing bar depends on the degree of thinning and on the position and orientation of the reinforcing steel relative to the antenna. We have performed initial measurements to map the radiation pattern broadcast by the antenna, fit that pattern to a two-parameter antenna model, and used the antenna model as one ingredient in GPR simulation software.

- The ability to increase the speed of the inspection during data acquisition and reduce the amount of road closure time will require the development of a new type of GPR hardware system. The use of multiple antennas would allow for the simultaneous comparison of a single reinforcing bar at several locations. Once the data were collected, an algorithm could then be employed to quantify the amplitude of the separate locations, thereby allowing for a quick determination of potential thinning of the reinforcing steel.

REFERENCES

Al-Qadi, I. L., Lahouar, S., and Loulizi, A. 2005. *Ground-Penetrating Radar Calibration at Virginia Smart Road and Signal Analysis to Improve Prediction of Flexible Pavement Layer Thicknesses*. Virginia DOT. FHWA/VTRC 05-CR7.

American Society of Civil Engineers (ASCE). 2009. http://www.infrastructurereportcard.org/

Bligh, Roger P., Nakirekanti, S., Bray, D., and James, R. 1994. Evaluation of NDE Techniques for Detecting Grout Defects in Cable Stays. *Materials Evaluation*.

Blitz, J. 1997. *Electrical and Magnetic Methods of Nondestructive Testing*. Second edition, Chapman & Hall, Chapter 3.

Brown, K., and St Leger, J. 2003. Use of the Megascan Imaging Process in Inspection Systems for Post-Tensioned Bridges and Other Major Structures. Non-Destructive Testing in Civil Engineering. International Symposium (NDT-CE 2003).

Callerame, Joseph. 2006. X-Ray Backscatter Imaging: Photography Through Barriers. *Powder Diffraction*. Vol. 21, 132.

Chase, S., and Washer, G. 1997. "Nondestructive Evaluation for Bridge Management in the Next Century." *Public Roads*, Vol. 61, No. 1.

Ciolko, A., and Mehrabi, A. 2002. "Toledo's New Signature Structure." *Public Roads*, Vol. 66, No. 2.

Ciolko, A., and Yen, W. 1999. "An Immediate Payoff from FHWA's NDE Initiative." *Public Roads*. Vol. 62, No. 6.

Ciolko, A. T., and Tabatabai, H. 1999. *Nondestructive Methods for Condition Evaluation of Prestressing Steel Strands in Concrete Bridges*. Final Report: Phase I–Technology Review. NCHRP Web Document 23 (Project 10–53). Transportation Research Board.

Clemena, G., Lane, S., Freeman, T., and Lozev, M. 2000. *Evaluation of Nondestructive Evaluation Methods for Application in Early Detection of Deterioration in Concrete Pavements*. Virginia Transportation Research Council, VTRC –R13.

DaSilva, M., Javidi, S., Yakel, A., and Azizinamini, A. 2009. *Nondestructive Method to Detect Corrosion of Steel Elements in Concrete*. Final Report NDOR Research Project No. P597. National Bridge Research Organization (NBRO).

Derobert, X., Aubagnac, C., and Abraham, O. 2002. Comparison of NDT Techniques on a Post-Tensioned Beam before its Autopsy. *NDT&E International* 35: 541-548.

DMJM Harris. 2003, *Test and Assessment of NDT Methods for Post-Tensioning Systems in Segmental Balanced Cantilever Concrete Bridges*. Florida Department of Transportation. Central Structures Office.

Dugan, E., Jacobs, A., Shedlock, D., and Ekdahl, D. Detection of Defects in Foam Thermal Insulation Using Lateral Migration Backscatter X-ray Radiography. Proceedings of SPIE 49th Annual Meeting, Symposium on Optical Science and Technology, Penetrating Radiation Systems and Applications VI, Vol. 5541.

Fernandes, B., Wade, J. D., Nims, D. K., and Devabhaktuni, V. K. 2012. "New Magnetic Sensor Concept for Nondestructive Evaluation of Deteriorated Prestressing Strand." *Research in Nondestructive Evaluation*. 23: 46–68. DOI: 10.1080/09349847.2011.626143.

Florida Department of Transportation (FDOT). 2003. *Test and Assessment of NDT Methods for Post-tension Systems in Segmental Balanced Cantilever Concrete Bridges*. Central Structures Office.

Ghorbanpoor, A., Borchelt, R., Edwards, M., and Abdel Salam, E. 2000. *Magnetic-Based NDE of Prestressed and Post-Tensioned Concrete Members – The MFL System*. Final Report FHWA-RD-00-026, Federal Highway Administration, US Department of Transportation, McLean, VA.

Gray, J. N., Inanc, F., Jensen, T., and Xu, J. 1998. Human Body Radiography Simulations: Development of a Virtual Radiography Environment. SPIE International Symposium on Medical Imaging.

Grosse, C. U. (Ed.). 2007. *Advances in Construction Materials*. 2007, 639–649. Springer, Berlin, Germany.

Hillemeir, B., and Scheel, H. 1998. "Magnetic Detection of Prestressing Steel Fractures in Prestressed Concrete." *Materials and Corrosion*, Vol. 49: 799-804.

Hussein, E. M. A., and Whynot, T. J. 1989. *A Compton Scattering Method for Inspecting Concrete Structures. Nuclear Instruments and Methods in Physics Research A283*. North-Holland, Amsterdam.

Jones, L., Pessiki, S., Naito, C., and Hodgson, I. 2010. *Inspection Methods & Techniques to Determine Non Visible Corrosion of Prestressing Strands in Concrete Bridge Components, Task 2 – Assessment of Candidate NDT Methods*. Lehigh University, ATLSS Report No. 09-09.

Kear, P., and Leeming, M. 1994. "Radiographic Inspection of Post-tensioned Concrete Bridges." *INSIGHT*. Vol. 36 No. 7.

Kusenberger, F. N., and Barton, J. R. 1981. *Detection of Flaws in Reinforcement Steel in Prestressed Concrete Bridges*. Final Report FH-WA/RD-81/087, Federal Highway Administration (FHWA), Washington, DC.

Mariscotti, M. A. J., Jalinoos, F., Frigerio, T., Ruffolo, M., and Thieberger, P. 2009. Gamma-Ray Imaging for Void and Corrosion Assessment. *Concrete International.* 48-53.

Mariscotti, M. A. J., Thieberger, P., Frigerio, T., and Ruffolo, M. 2007. Method and Device for Improving Tomographic Determinations, Particularly Suitable for Inspection of Steel Reinforcement Bars in Concrete Structures. Tomografia De Hormigon Armado S.A., US patent office, application number PCT-US2007/2286.

Martz, H., Schneberk, D., Roberson, P., and Monteiro, P. 1993. Computerized Tomography Analysis of Reinforced Concrete. *ACI Materials Journal*. Vol. 90, No. 3.

Moore, M., Rolander, D., Graybeal, B., Phares, B., and G. Washer. 2001. *Highway Bridge Inspection: State-of-the-Practice Study*. FHWA-RD-01-033.

Naito, C., and Jones, L. 2010. Nondestructive Inspection of Strand Corrosion in Prestressed Concrete Box Beam Members. NDE/NDT for Highways and Bridges: Structural Materials Technology Conference, New York City.

National Transportation Safety Board (NTSB). 2010. Safety Recommendations H-10-17 and -18. Washington, DC.

Nims, D. K., and Devabhaktuni, V. 2011. *Magnetic Sensor for Nondestructive Evaluation of Deteriorated Prestressing Strand – Phase II*. Final report to The University of Toledo University Transportation Center.

Owen, R.D. 1998. "Portable Linear Accelerators for X-ray and Electron-beam Application in Civil Engineering." *NDT&E International*. Vol. 31, No. 6, 401-409.

Pimentel, M., Figueiras, J., Mariscotti, M., Thieberger, P. Ruffolo, M., and Frigerio, T. 2010. Gamma-Ray Inspection of Post Tensioning Cables in a Concrete Bridge. Proceedings of Structural Faults and Repair-2010 Conference, Edinburgh, UK.

Pinna, M. 2002. Inspection of Post Tension Cables in concrete using High Energy X-rays. Ramp D at the Ft Lauderdale Airport.

Podolny, W. Cox, W., Hooks, J., Miller, M., Moreton, A., Shahawy, M., Edwards, D., Madani, M., Montgomery, R., Pelstick, B., and Tang, M-Chung. 2001. *Performance of Concrete Segmental and Cable-Stayed Bridges in Europe*. Report No. FHWA-PL-01-019.

Rens, K., Wipf, T., and Klaiber, W. 1997. "Review of Nondestructive Evaluation Techniques of Civil Infrastructure." *Journal of Performance of Constructed Facilities.* Vol. 11, No. 4, 152.

Sawade, G., and Krause, H-J. 2007. "Inspection of Prestressed Concrete Members Using the Magnetic Leakage Flux Measurement Method – Estimation of Detection Limit." *Advances in Construction Materials*. 639-649.

Scheel, H., and Hillemeier, B. 1997. "Capacity of the Remnant Magnetism Method to Detect Fractures of Steel in Tendons Embedded in Prestressed Concrete." *NDT & E International*. Vol. 30, No. 4. 211-216.

Sirles, P. 2006. *Use of Geophysics for Transportation Projects – NCHRP Synthesis 357*. Transportation Research Board. Washington, DC.

Wimsatt, A., Scullion, T., Fernando, E., Hurlerbaus, S., Lytton, R., Zollinger, D., and Walker, R. 2009. *A Plan for Developing High Speed Nondestructive Testing Procedures for Both Design Evaluation and Construction Inspection*. SHRP 2 Report S2=R06-RW. Washington, DC.

Xu, J., Wallingford, R., Jensen, T. and Gray, J. 1994. "Recent Developments in the X-Ray Radiography Simulation Code: XRSIM." *Review of Progress in Quantitative Nondestructive Evaluation*. D. O Thompson and D. E. Chimenti (Eds.) Vol. 13: 557.

Yu, Thomas, and Khazanovich, L. 2005. *Use of Magnetic Tomography Technology to Evaluate Dowel Placement*. Final report: FHWA-IF-06-006. US Department of Transportation, Federal Highway Administration.